Luminescent Probes of Emergent Physics from Organic Semiconductor Interfaces

A Thesis

SUBMITTED TO THE FACULTY OF

UNIVERSITY OF MINNESOTA

BY

Nolan Concannon

IN PARTIAL FULFILLMENT OF THE REQUIREMENTS

FOR THE DEGREE OF

DOCTOR OF PHILOSOPHY

Russell J. Holmes, Advisor

December 2022

Acknowledgements

Thank you to my advisor Russ Holmes for his training and help defining a thesis topic, designing and analyzing measurements, editing manuscripts and his earnest career advice. Additionally, I want to acknowledge the training and direction I received from Dr. Tao Zhang in my first few years. Special thanks to Dr. John Bangsund for his support and for helping set up the automated biased-PL setup which likely would have taken months longer to develop or manually collect data without his help. I also recognize the other members of the Holmes group whom I had pleasure to train with including Ian, Kyle, Deepesh, Catherine, Kaicheng, Rajiv, Robert, Wan-Ju, Evgeny, Betty, Brian, Emma, and Colton.

Additional thanks to my classmates and friends who enriched my time outside of research, including Kevin, Eeshani, Justin, and Supriya. I appreciate the many classmates I worked with through Science for All and UMN Materials Research Society, which contributed to my personal and professional development. Thank you to the ~200+ CEMS graduate and undergraduate students who excited my love of teaching. Also, I want to recognize the incredible staff in the CEMS main office, namely Julie, Theresa, Jenny and Gayle.

I want to thank my parents, Pat and Mary, and family who steadfastly supported my pursuit to become the first doctor of the family. Finally, I thank my wife Hannah, to whom this thesis is dedicated for her patience and partnership over many years.

This work was supported by National Science Foundation (NSF) Electronics, Photonics and Magnetic Devices under ECCS-1509121 and Solid-State and Materials Chemistry under DMR-1708177. I was individually supported in my first year by fellowships from Curtis and Joyce Stendahl, Chris and Kathleen Macosko, and the First-Year Graduate Student Fellowship Fund established by Bob and Jane Gore. Subsequent years were supported by the NSF Graduate Research Fellowship under Grant 00074041. Parts of this work were performed in the Characterization Facility, University of Minnesota, which receives partial support from NSF through the MRSEC program.

Dedicated to Hannah, who has the clarity of mind to know that a 30th rant about the paper with a deeply unphysical model of coulombic interactions does not a thesis make.

Abstract

To prevent the most harmful effects of the present climate crisis, development of higher performance energy conversion devices is needed to accelerate the adoption of renewable energy and energy efficiency technologies. Organic semiconductor materials have demonstrated exciting efficiency gains in a variety of emerging and in-production devices. These materials exhibit a variety of emergent material and device physics, requiring additional research to understand and design next-generation energy conversion technologies. Thin films of organic semiconductors, common in large-area optoelectronics such as consumer displays, present rich photophysics due to forming room-temperature stable excitons, unlike silicon or III-V semiconductors. A plethora of emergent phenomena of excitons at organic semiconductor interfaces requires a detailed understanding of such processes to optimally design devices such as energy-efficient lighting, flexible or transparent solar cells, photodetectors and displays.

This dissertation focuses on investigating the novel optical physics of excited states at organic donor-acceptor interfaces through emission spectroscopy of organic mixtures and bilayer devices. In one study, exciplex diffusion is investigated in several donor-acceptor pairings toward an improved understanding of the mechanism of nanoscale energy transport in organic semiconductor mixtures. Additionally, the effect of electric field on exciplex emission spectra is studied to detail the effect of field on exciplex energy and electron-hole separation. Finally, preliminary data displaying the effect of binary dilution on exciplex energy in a two-component mixture is presented. All together, these findings present new insights into the behavior of key device properties such as exciton diffusion length and excited state energies to aid further study of device performance.

Table of contents

List of figures

List of tables

1. Organic optoelectronics for sustainable energy

To limit the effects of the ongoing climate crisis, global carbon dioxide emissions must be dramatically cut in the near term. One major source of such emissions arises from electricity generation from carbon-rich natural gas, coal, and oil. These energy sources will need to be replaced with low-carbon technologies such as nuclear, wind, hydropower, solar, biomass and geothermal energy sources. Of these, wind and solar energy possess the simultaneous potential for fast implementation at scale and abundant energy availability [1]. Additionally, energy efficiency improvements at point-of-use can reduce demand for electricity and supplement this energy transition. Gielen et al. laid out a possible mix of energy sources that would limit average global temperature increases to below 2 °C, a key goal in the Paris Climate Accords, which included raising photovoltaic solar generation to 15% of energy use from the current share of 2.8% [2,3]. Additionally, energy efficiency factored in as a means for 40% of the reduction in carbon emissions, comparable to the impact of expanded use of *all* renewable energy sources. Specifically, lighting consumes 5% of total US electricity, providing an important sector for efficiency gains [4]. Improving photovoltaic generation and reducing lighting consumption are important facets of any clean energy transition.

One class of materials that can significantly impact both applications are organic semiconductors, which are small molecules and polymers based on carbon that can efficiently transport charge, absorb, and emit light. Semiconductors with a wide range of absorption, charge transport, and mechanical properties have been identified and

incorporated in optoelectronic devices. These materials are currently used in several applications such as organic photovoltaics (OPVs) such as solar cells and photodetectors, and organic light-emitting devices (OLEDs). Organic semiconductors are soft materials permitting fabrication of flexible thin films enabling roll-to-roll processing on flexible substrates [5,6]. This chapter briefly introduces these devices and provides an overview of the remaining thesis.

1.1. Organic photovoltaic devices (OPVs)

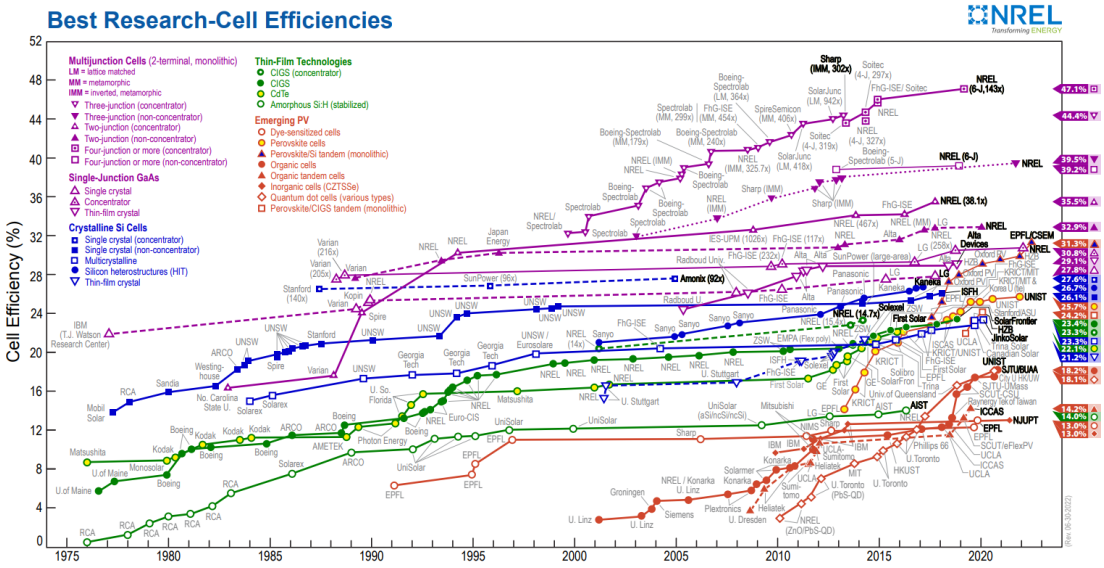

Figure 1.1 Chart of the best research-cell efficiencies of solar cells reported by the National Renewable Energy Laboratory (NREL) [7].

Organic photovoltaic devices are thin-film multi-layer stacks of organic semiconductors and metals, first demonstrated in 1958 by Kearns and Calvin [8], with incremental progress over the next ~30 years [9,10] before C.W. Tang demonstrated a device in 1986 exceeding 1% power conversion efficiency [11]. These devices convert incident light energy into electricity, by generating photocurrent. Organic solar cell power conversion efficiency has reached 18.2% [12] compared to incumbent single-crystal

silicon efficiency of 26.1% [7]. However, OPVs possess several advantages that enable their use as building integrated photovoltaics and other applications [13,14]. One advantage is that the mechanical softness of organic semiconductors leads to fabrication of flexible organic thin films on plastic substrates or metal foil [5]. This provides light-weight solar cells with the ability to conformally cover curved structures or surfaces that cannot bear the load of silicon solar cells. Example applications of flexible organic solar cells are shown in Figure 1.2 (a-b) [15]. The low weight of these cells also reduces installation difficulty and improves handling safety, reducing the non-panel costs of an OPV system [16]. Additionally, discussions are ongoing to attain >20% power conversion efficiency for OPVs, further closing the efficiency gap with incumbent technologies [17].

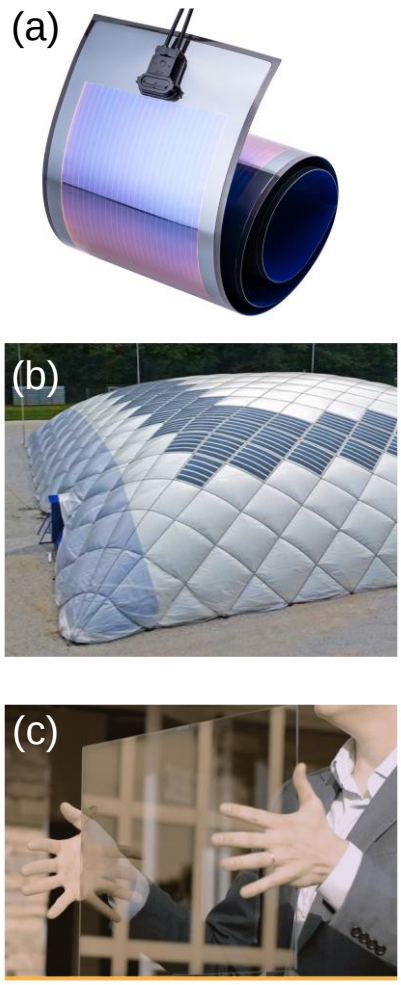

Figure 1.2 (a) Flexible solar panel (b) Flexible solar panels installed on an inflatable tent (Heliatek GmbH). (c) Transparent solar cell. (Ubiquitous Energy, Inc.).

Additionally, the ability to tune material optical absorption by selecting or designing different molecular structures enables devices that only absorb light in the UV or IR regions of the electromagnetic spectrum. This has been applied in transparent photovoltaics that are used as windows with integrated solar cells, such as one shown in Figure 1.2 (c) [18,19]. Such devices can be integrated into buildings in ways that access surfaces not available to

traditional solar panels and in a manner that may not noticeably change the appearance of an existing building. Finally, transparent photovoltaics have been explored for use with greenhouses to generate electricity from light that would otherwise go unused in plant growth to provide power for accessory equipment such as ventilation or lighting [20,21].

1.2. Organic light-emitting devices (OLEDs)

Organic light-emitting devices use layers of organic semiconductors to transport injected charges to an electroluminescent material. Initially demonstrated in 1987 by C.W. Tang and S.A. Van Slyke [22], these devices have been manufactured for use in smartphone and television displays, with example products shown in Figure 1.3 [23,24]. They have superseded liquid-crystal (LCD) displays in smartphones because they do not require a backlight, allowing for true black providing excellent contrast. LCDs require a white backlight that is filtered to provide the desired pixel color, which wastes light and thus energy efficiency [6,25]. Additionally, the mechanical flexibility of organic thin films has allowed for flexible and foldable displays, while additional interest focuses on their use for automotive and solid-state lighting. Considerable work has been devoted to improving efficiency and stability of OLEDs [26–31], with recent work including development of high-brightness white OLEDs for lighting [32–35].

Figure 1.3 (a) Motorola Razr foldable smartphone (Motorola, Inc.). (b) LG OLED evo television display (LG Group).

1.3. Thesis Overview

This thesis will explore the properties of molecular excited states known as "excitons" in organic semiconductor thin films, with emphasis on the energetics and transport of interfacial excited states formed at electron donor-acceptor interfaces. An excited electron-hole pair bound across an interface of different organic semiconductors is called a charge-transfer (CT) state or exciplex. These states are critical intermediates in the operation of OPVs and are emerging as a means of improving efficiency and stability in OLEDs [36–38]. Deeper insight into the excited state properties of CT states and exciplexes can be used to better design and optimize these devices. In Chapter 4, the diffusive energy transfer of exciplexes is investigated understand the mechanism of transport and provide tools to tune the length scale of this diffusion, which will enable deeper study of the role of CT state transfer in OPV device performance. Additionally, methods to tune the energy of exciplexes are explored in Chapters 5 and 6. In the first of this pair of study, electric fields are applied to exciplex-forming bilayer devices to understand the effect of field on exciplex energy. This led to the identification of the giant Stark effect in organic semiconductors, which provides a means of tuning exciplex energy and probing excited state structure in exciplex systems. In the other study, preliminary findings are provided showing a sensitivity of exciplex energy to the relative abundance of donor versus acceptor in binary mixtures, with an initial explanatory model described. Finally, Chapter 7 will summarize the findings of this thesis and the impact of this work.

2. Material and device physics of organic semiconductors

Organic semiconductors are conjugated small molecules or polymers that contain primarily carbon and possess an energy gap between ~1-4 eV [39]. They are notable for their ability to stably host and efficiently transport charges and their capability to absorb or emit light in the visible and near infrared portions of the electromagnetic spectrum (~380-1000 nm). These materials are applied in a range of settings such as passive dyes, channel materials in thin-film transistors, and as the active components of organic photovoltaic and light-emitting devices [6,19,25]. These later applications in electroluminescence and photoconversion must carefully consider the excitonic nature of these materials to properly design and optimize device performance.

This chapter will introduce the structure and bonding of organic semiconductors, describe the excitonic nature of excited molecules and outline the important processes and properties of excited organic semiconductors in OPVs and OLEDs. Special attention will be given to the role of energy transfer processes and material interfaces on device operation. As this section provides a brief overview of a broad range of topics, readers are referred to *Electronic Processes in Organic Semiconductors: An Introduction* by Köhler and Bässler and *Modern Molecular Photochemistry* by Turro for further details [39,40]. Köhler and Bässler provide an excellent introduction to organic semiconductors, exciton physics, and organic device principles, while Turro provides essential depth of study to molecular photophysics.

2.1. Structure and bonding of organic semiconductors

In contrast to the covalent bonds formed between atoms within a molecule, the interactions between molecules in a solid are much weaker, typically characterized by van der Waals bonding. Solid films can be found in crystalline or amorphous form, but typically electronic states remain localized to one or a few molecules, rather than extended throughout a solid, as in inorganic semiconductor crystals. Additionally, these molecular solids exhibit low relative dielectric constants of ~2-4, vs. ~11 for silicon [39].

Conjugation in molecules and polymers arises from alternating single and double carbon-carbon bonds formed by stronger σ-bonds between sp^2-hybridized electrons and weaker π-bonds of unhybridized p_z-orbital electrons. The weaker π bonds exhibit smaller energy splitting between resulting π bonding and π* antibonding orbitals than for σ bonds with σ and σ* orbitals, leading to smaller energy gaps than for unconjugated structures [39]. The highest energy orbital filled with electrons in the ground state, typically a π bonding orbital, is called the highest occupied molecular orbital (HOMO), while next lowest energy orbital, unfilled in the ground state and typically a π* antibonding orbital, is called the lowest unoccupied molecular orbital (LUMO). The difference in energy between the HOMO and LUMO is referred to as the transport energy gap [41].

Organic semiconductors can be excited by absorbing a photon, whereby an electron is excited from the HOMO to the LUMO leaving behind a hole in the HOMO, although the energy required to excite an electron is lower than the HOMO-LUMO gap due to the coulombic attraction between the resulting electron and hole, and is commonly referred to as the optical energy gap [41]. Due to the low dielectric constants of organic semiconductors, the weak screening of the electric field within the electron-hole pair leads

to significant energy being stored in the attraction of the charge pair. These bound pairs are called excitons, while the Coulombic interaction energy between the carriers is called the binding energy (E_b). The binding energy reduces the energy stored in the exciton from that of carriers residing in the HOMO and LUMO energy levels, and is often expressed as follows:

$$E_b = \frac{q^2}{4\pi\epsilon_0\epsilon_r r} \quad (2.1)$$

where q is the elementary charge, ϵ_0 is the vacuum permittivity, ϵ_r is the relative dielectric constant of the excitonic material, and r is the electron-hole separation in the exciton. Typical exciton binding energies of 100 meV up to few eV are observed, varying between different materials and film morphologies [42]. Excitons of organic semiconductors can further be classified as Frenkel or local type, in which the electron and hole reside on a single molecular subunit, or charge-transfer (CT) type, which span heterojunctions formed between dissimilar semiconductors with electron-hole separations of ~0.5-5 nm [43–45]. Notably, application of Equation 2.1 is further complicated for Frenkel excitons as there is significant electron-hole overlap and the relevant dielectric is the space occupied by a single molecule [46], however it is frequently applied with improved accuracy for CT states [47]. Additionally, CT states are still more localized than Wannier-Mott excitons typically observed in traditional, crystalline semiconductors like Si and GaAs at low temperature [48,49], which are delocalized over ~5-10 nm [39,50]. Importantly, the delocalization of CT states versus local excitons leads to significantly reduced binding energy, reducing the required fields to dissociate excitons from $>10^6$ V/cm to 10^5 V/cm [42,51,52], aiding efficient carrier generation in organic photovoltaic devices.

2.2. Exciton kinetics and energy transfer

2.2.1. Types of excitons

In addition to the classifying excitons by their degree of delocalization mentioned above, excitons can be described by their electronic excitation level, vibrational excitation level, and quantum mechanical spin. In absorption measurements, transitions to higher electronic excited states are commonly observed, however the ability for excitons to relax before recombination leads to less frequent, although not uncommon, observation of higher excited states in emission spectra [39,53,54]. Exciton vibrational levels can be important to understand the structure of absorption and emission spectra of molecular thin films. An energy diagram depicting transitions between the electronic potential energy manifold for the ground (S_0) and excited state (S_1) of a material are shown in Figure 2.1.

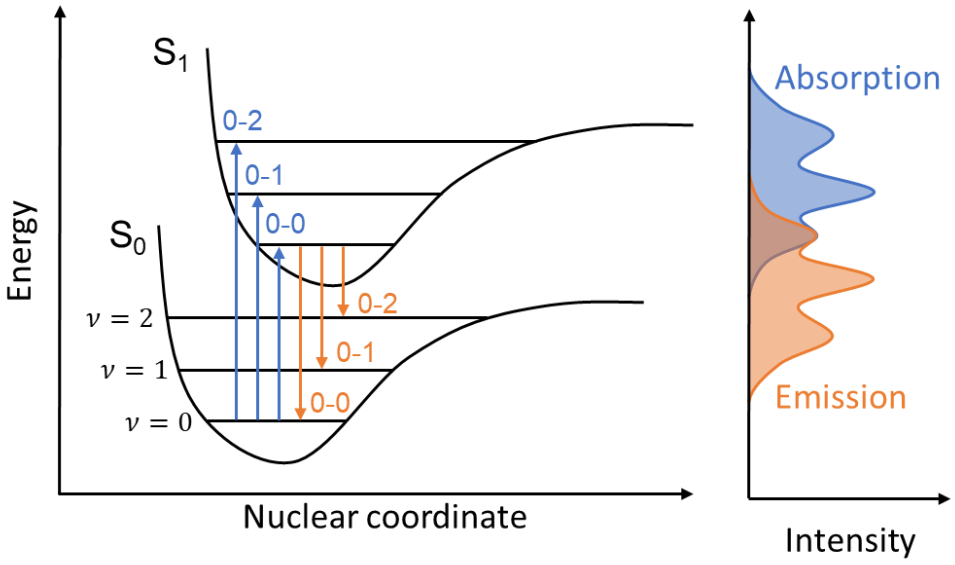

Figure 2.1 Electric potential energy diagram for ground state-excited state electronic transitions. Resulting absorption and emission spectra from superposition of vibronic series.

Absorption transitions may occur between the ground vibrational state ($\nu = 0$) of S_0 to equal or higher vibrational states of S_1 ($\nu \geq 0$). Depending on the specific coupling and

resulting rates between these states, the absorption spectrum may possess several vibronic features, as shown in the right-hand plot of Figure 2.1. After absorption, the vibrationally excited molecules will lose energy and relax via internal conversion to the lowest vibrational state ($\nu = 0$) of S_1, typically on timescales of ~$10{-}10^4$ ps. If emission occurs, a superposition of transitions can also result leading to vibrationally structured PL spectra [40].

Since excitons are composed of Fermionic electrons and holes of spin-1/2, the resulting boson may have integer spin of 0 or 1. However, the spin-1 exciton is triply degenerate and are thus called triplet excitons, while the spin-0 excitons are called singlet excitons [55]. Since the ground state typically has a HOMO filled with two electrons of opposite spin, it also possesses spin of 0 and is a singlet. As photons possess zero spin, singlets are uniquely generated by direct optical absorption. Electrical excitation occurs from two uncorrelated carriers and typically leads to about 75% triplets and 25% singlets [56,57]. Additionally, singlet excitons may be converted to triplet excitons by undergoing intersystem crossing, with characteristic timescales longer than 10 ns and is more commonly observed for molecules containing heavy-atoms such as Cu, Zn, or Ir which allow for significant spin-orbit coupling leading to excited states with mixed singlet and triplet character [55].

2.2.2. Exciton recombination

The excitonic nature of organic semiconductors substantially affects the kinetics of recombination and energy transfer in organic semiconductors. Recombination can occur radiatively, emitting light, or non-radiatively, generating heat. Further, radiative recombination can be divided broadly into fluorescence and phosphorescence. Fluorescence arises from radiative recombination of singlet excitons, while

phosphorescence arises from triplets. Fluorescence typically occurs on the timescale of 1-50 ns [58]. Meanwhile phosphorescence is quantum mechanically forbidden due to the change from spin-1 of triplet excited states to a spin-0 ground state of the excited molecule, leading to long lifetimes well beyond 1 s, however the spin-mixing mentioned above can enable recombination on microsecond timescales [39,40]. Additionally, high excitation densities, higher-order recombination via exciton-exciton or exciton-charge mechanisms, such as triplet-triplet and triplet-polaron quenching can also dominate [59]. Such quenching mechanism have been identified to be key determinants in OLED degradation, limiting device operational lifetime [28,60,61]. As summary of these processes can be found in Figure 2.2.

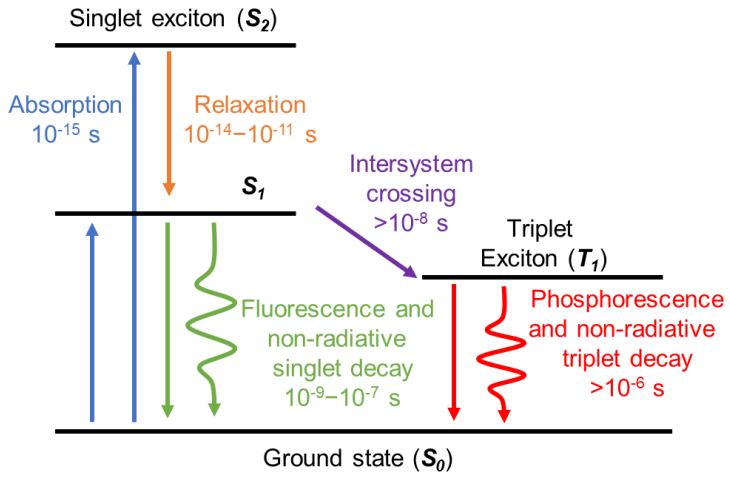

Figure 2.2 Jablonski diagram of common excitonic state transitions. Vibrational energy levels are not depicted for simplicity.

The energy of singlet and triplets differ by the exchange energy which depends on the spatial overlap between the electronic orbital wavefunctions of the two states, leading to reduced strength of interaction at larger separations. As such, Frenkel excitons often exhibit large exchange energy splitting, 0.7-1.0 eV [55], due to significant HOMO-LUMO overlap, although molecules have been observed and specifically designed for small

splitting [36]. Meanwhile, CT states and exciplexes have smaller splitting between singlet and triplet states due to the separation between the donor HOMO and acceptor LUMO, providing only a small energy barrier between singlet and triplet states comparable to thermal energy (k_bT) at room temperature of order 25 meV. This small exchange energy splitting enables efficient interconversion between singlet and triplet states through intersystem and reverse intersystem crossing, which will be more thoroughly discussed in Section 0.

2.2.3. Förster energy transfer

The most commonly observed mechanisms of exciton energy transfer are Förster and Dexter type energy transfer, summarized schematically in Figure 2.3 [39]. Förster-type energy transfer occurs by radiative coupling of dipoles between an excited exciton donor unit and an exciton acceptor unit. The rate of energy transfer is determined by several factors, with a characteristic dependance on dipole-dipole separation determined by the arrangement of the donor and acceptor molecules. One such relationship for point dipoles separated by a distance d, the Förster energy transfer rate (k_F) is seen in Equation 2.2:

$$k_F = \frac{1}{\tau}\frac{{R_0}^6}{d^6} \qquad (2.2)$$

Where τ is the exciton lifetime, and ${R_0}^6$ is the Förster transfer radius raised to the sixth power, which can be expressed as in Equation 2.3 [58], although other expressions for the transfer rate have been described for other transfer geometries [62–64]:

$${R_0}^6 = \frac{9\eta_{PL}\kappa^2}{128\pi^5 n^4}\int \lambda^4 F_D(\lambda)\sigma_A(\lambda)d\lambda \qquad (2.3)$$

where η_{PL} is the photoluminescence efficiency of the exciton, κ is the dipole orientation factor, n is the refractive index of the medium, λ is the wavelength, F_D is the area-

normalized fluorescence spectrum of the exciton and σ_A is the absorption cross-section of the acceptor molecule. This mechanism is typically dominant for excitons that are luminescent, with high η_{PL}, even though photon emission is not required, with strong spectral overlap between donor emission and acceptor absorption. The relative molecular orientation between exciton donor and acceptor molecules will have a significant impact on energy transfer through the dipole orientation factor, κ.

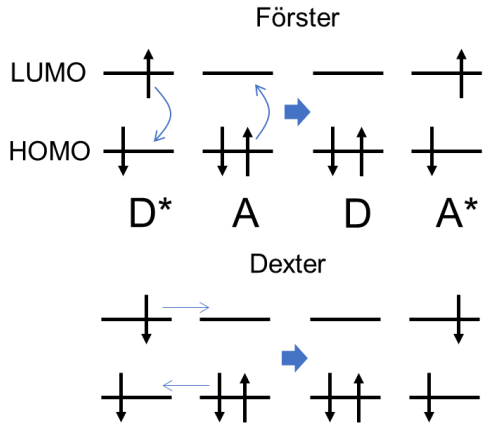

Figure 2.3 Schematics of exciton energy transfer mechanisms. Transfer occurs between an excited donor (D*) and ground state acceptor (A) to form a ground state donor (D) and an excited acceptor (A*). Top: Förster transfer via dipole coupling. Bottom: Dexter transfer via electron exchange

2.2.4. Dexter energy transfer

Dexter-type energy transfer, on the other hand, is always active, but is the dominant mechanism of energy transfer for dark excitons, such as weakly- or non-emissive triplet excitons. Dexter type transfer occurs via an electron exchange interaction between the excited donor and the acceptor units, whereby the excited electron and hole transfer from one unit to the other, as shown in Figure 2.3. The rate of Dexter transfer (k_D) is typically described as in Equation 2.4 [58]:

$$k_D = KJe^{-\frac{2d}{L}} \qquad (2.4)$$

where K is a pre-factor related to the specific orbital interaction, J is the spectral overlap integral normalized to the extinction coefficient of the acceptor, d is again molecular spacing, and L is the van der Waals radius of the molecules. Due to the steep dependance of Dexter transfer on molecular spacing, most transfer events occur between nearest-neighbor molecules, such that acceptors separated by $d \approx L$ dominate the transfer rate. This mechanism is typically dominant for non-luminescent excitons, such as triplet excitons, as the quantum mechanical prohibition of radiative recombination can be circumvented by this nonradiative transfer mechanism, with only electronic orbital overlap being required.

2.2.5. Exciton diffusion

Regardless of energy transfer mechanism, excitons have the possibility to migrate throughout a solid before recombining, often within nanoseconds for Frenkel excitons or microseconds for CT states [47], leading to exciton diffusion which can be described with a diffusivity, D, which can be related to the exciton energy transfer rate summed between all N neighbors, which can be expressed for an cubic lattice as [58]:

$$D = \frac{A}{6}\sum_N d^2 k_{ET}(d) \quad (2.5)$$

where A is a dimensionless parameter of order unity related to the disorder of the solid. In a cubic lattic with isotropic diffusion, this reduces to $D = Ad^2k_{ET}$ [58]. Considering generation, recombination, and exciton energy transfer together, we may model steady-state exciton kinetics in one dimension using Equation 2.6 [65]:

$$0 = D\frac{d^2n}{dx^2} - \frac{n}{\tau} + \theta_1\frac{Q(x)}{h\nu} \qquad (2.6)$$

where n is the volumetric exciton density, τ is the exciton lifetime, θ_1 is the quantum efficiency of exciton generation, and $h\nu$ is the energy of the exciting photon. The exciton diffusion length L_D, which is the square-root of the product of diffusivity and lifetime as $L_D = \sqrt{D\tau}$ [58]. Steady-state exciton density distributions can be calculated in active layers of organic semiconductors using appropriate boundary conditions provided an accurate model for the volumetric energy dissipation density Q, (see Section 3.4). Direct or indirect methods of measuring the exciton density or total number of excitons formed in a sample can be used along with the combined optical and transport models to experimentally extract exciton diffusion lengths.

Exciton diffusion lengths of amorphous small molecule semiconductors are on the order of ~1-10 nm for singlet excitons [58,66]. Two common methods for extracting exciton diffusion lengths, which are used in this thesis, are wavelength and thickness dependent photoluminescence quenching spectroscopy. Additional strategies use photoluminescence or transient absorption microscopy, as well as time-dependent photoluminescence quenching [58,66–68]. Finally, device-based measurements have been developed to extract the exciton diffusion length of several emerging semiconductors in thin-film photovoltaic devices [69]. Further details and a demonstration of the thin-film optical model employed for extracting diffusion length from measurements of thickness-dependent photoluminescence quenching are discussed in Sections 3.4 and 3.5.

2.3. Exciplexes at donor-acceptor heterojunctions

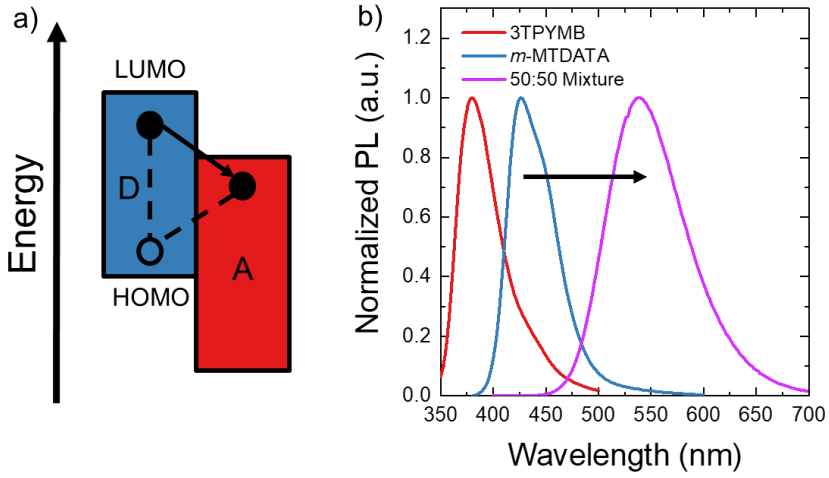

Figure 2.4 Exciplex formation schematic. (a) HOMO-LUMO energy diagram for a donor (D)-acceptor (A) system with a local donor exciton undergoing charge-transfer to form an exciplex. (b) Photoluminescence (PL) spectra of donor m-MTDATA, acceptor 3TPYMB, and a 50:50 mixture of m-MTDATA:3TPYMB exhibiting the characteristic red-shifted exciplex PL.

In addition to excitons present in single-component thin films excitons can form at interfaces between organic semiconductors. Such interfacial excitons can form at electron donor-acceptor interfaces where the hole resides in a donor HOMO and the electron resides in an acceptor LUMO, as is Figure 2.4 (a). The terms “CT state” and “exciplex” are often used interchangeably, with the later distinguished by its propensity for efficient photoluminescence [36,47]. As all interfacial states studied in this thesis are emissive, these terms will be used interchangeably. Exciplex formation can be observed in emission by the emergence of a significantly broadened and red-shifted spectrum, lacking any distinguishable vibronic structure, versus either pure component material, as in Figure 2.4 (b) for the 50:50 donor-acceptor pairing of m-MTDATA:3TPYMB. Often, wide-gap electron or hole transport materials are used as the donor or acceptor materials in exciplex-forming systems, such as the hole transport materials m-MTDATA, TAPC,TPD, TCTA or mCP and the electron transport materials such as Alq3, 3TPYMB, BPhen, BCP, and PO-

T2T, for which molecular structures can be found in Figure 2.5 [70]. Having been originally designed as transport materials for OLEDs, these materials typically form glassy, amorphous thin films in the solid state.

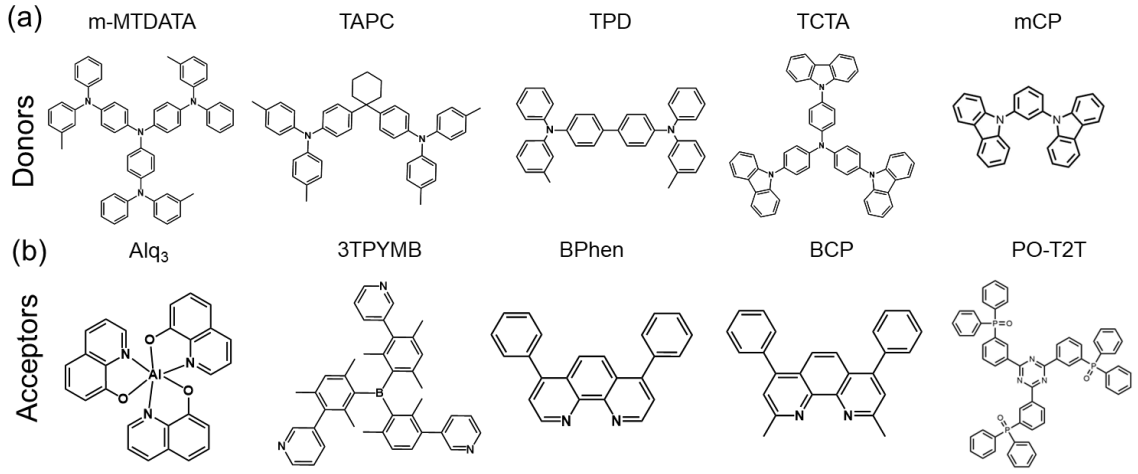

Figure 2.5 Molecular structures for materials in common exciplex-forming mixtures. (a) Donor materials (b) Acceptor materials

Most exciplexes have been studied in mixtures of donor and acceptor materials, as this provides high contact area for charge-transfer [47]. However, due to the random arrangement of molecules in the mixture, exciplexes can form with any orientation, leading to the lack of structured emission. Compared to mixtures, bilayers possess less contact area, which leads to mixed local and exciplex emission in PL, as charge-transfer is limited. However, the exciplexes formed in a bilayer are oriented, with the dipole moment from electron to hole aligned in the out-of-plane direction from acceptor to donor layers. Both mixtures and bilayers of donor and acceptor materials will be used in this thesis to study the properties of organic exciplexes, as both have been applied in organic semiconductor devices such as OPVs and OLEDs [42,71,72].

2.4. Organic photovoltaic devices (OPVs)

2.4.1. Device principles

Organic photovoltaic devices typically consist of multi-layer stacks of single or multi-component organic thin films sandwiched between metallic contacts. One such architecture for a planar heterojunction OPV is shown in Figure 2.6 (a). The structure can be fabricated on glass with a transparent, conductive anode, such as Indium-Tin-Oxide (ITO), which allows light to enter the device, while enabling charge collection. Sequential layers of donor and acceptor organic semiconductors are included to form the optically active region of the device, while a metallic top-contact of Al is included as the cathode.

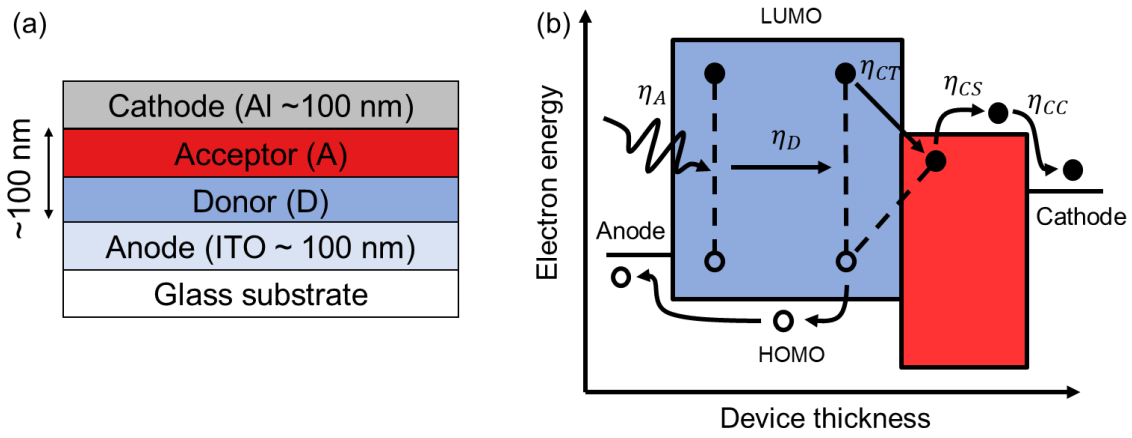

Figure 2.6 (a) Schematic of layer architecture of planar heterojunction OPV (b) Energy level diagram of planar heterojunction OPV. A photon is absorbed in the donor to form an exciton. The exciton diffuses to the donor-acceptor interface and undergoes charge transfer to form a CT state. The CT state is dissociated into free charges which are collected at the anode and cathode.

When an OPV is illuminated with light with photons of energy above the energy gap(s) of the acceptor and/or donor materials, light will be absorbed forming excitons with an absorption quantum efficiency of η_A [65,73], as depicted in Figure 2.6 (b). Excitons can then migrate throughout the active layers until they reach the donor-acceptor interface and undergo charge transfer to form CT states with efficiencies for diffusion of η_D and charge-

transfer of η_{CT}, respectively [47,58,66]. Then, CT states can dissociate to form mobile charges with charge separation efficiency η_{CS} [42]. At steady state, the chare carriers will either be extracted at the contacts generating photocurrent or recombine with one another, with charge collection efficiency η_{CC} [74]. Each recombination event leads to loss of achievable current density and limits device performance. Efficient device operation requires simultaneous optimization of light absorption, exciton diffusion, carrier dissociation, and carrier extraction to maximize external quantum efficiency (η_{EQE}) [42], the ratio of extracted charges to incident photons, as:

$$\eta_{EQE} = \eta_A(\lambda)\eta_D(L_D)\eta_{CT}\eta_{CS}\eta_{CC} \qquad (2.7)$$

Key factors that affect the absorption efficiency include the exciting wavelength (λ), the optical extinction coefficients of the donor and acceptor, and layer thicknesses. The exciton diffusion efficiency is primarily determined by the exciton diffusion length (L_D) and the heterojunction geometry and morphology, with smaller donor and acceptor domains providing easier access to the D-A interface [58,66]. This interface may be between two clearly defined layers, in a planar heterojunction, or at domain boundaries between mixed phases of donor and acceptor materials in a single layer, in a bulk heterojunction. Each of these heterojunction geometries are depicted in Figure 2.7. Charge transfer efficiency is sensitive to the LUMO and HOMO energy offsets at the D-A interface as well as precise molecular arrangements leading to stronger or weaker orbital overlap, impacting carrier transfer [47]. Charge separation efficiency is sensitive to the interfacial field experienced by the CT state. Charge collection efficiency is impacted by the carrier mobilities, electric field distribution within the device, and degree of segregation of donor and acceptor domains [74].

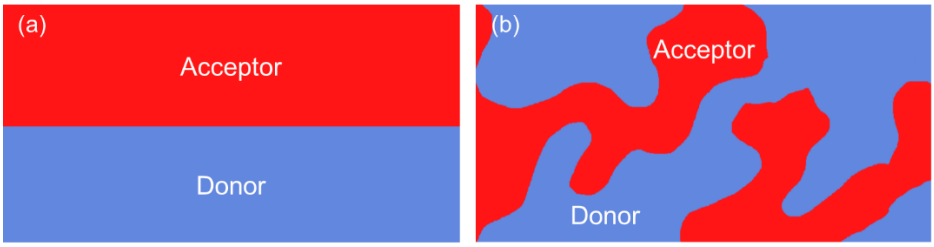

Figure 2.7 Organic donor-acceptor heterojunction geometries (a) A bilayer or planar heterojunction with a defined layer of an acceptor materials on a donor material. (b) A mixed or bulk heterojunction with domains of acceptor mixed into a donor. Domain sizes may be on the scale of several nanometers or individual molecules randomly mixed throughout.

Tradeoffs between absorption, diffusion, and charge recombination determine the optimal donor and acceptor thicknesses and degree of mixing in bulk heterojunctions. While long absorption lengths (~100 nm) favor thick layers [42], small diffusion lengths (~5-30 nm) require small donor and acceptor domains [66]. Thick mixed films, as in a bulk heterojunction architecture can break the tradeoff between absorption and diffusion, however intimate contact between hole-carrying donors and electron-carrying acceptors will lead to charge recombination, requiring some degree of phase segregation. Improved diffusion lengths and deeper insight into energy transfer in organic heterojunctions is key to optimizing and improving upon these limitations.

2.4.2. Exciton diffusion and charge-transfer states

As noted above, the optically generated excitons must reach dissociating heterojunctions before they recombine to be efficiently harvested as photocurrent [11,58,69]. Thus, the exciton diffusion length (L_D) sets the fundamental length scale for photoconversion in organic thin film devices. Deeper understanding of the factors that determine exciton energy transfer are critical to improving and optimizing OPVs and has attracted significant investigation. Additionally, the formation, dissociation, and recombination of charge-transfer states at the D-A interface serves as another critical

area of study as facile dissociation to carriers facilitates current generation [47]. Substantial work has been devoted to understanding both the dynamics and energetics of CT states, but recent work has added another potential kinetic process to be considered [75–79].

One process not captured in the standard charge generation pathway discussed in the section above is CT state diffusion, which was observed in 2016 by Deotare et al. for the exciplex-forming pair of m-MTDATA:3TPYMB which provides new questions about what impact this has on photoconversion [80]. While a pair of studies have followed considering the phenomenon of exciplex energy transfer, details determining the role of CT state diffusion on OPV device performance have not been reported [81,82]. Unlike local exciton diffusion which is essential for efficient charge generation, CT state motion may help or hinder device performance when excitons reach quenching, trapping, or dissociating sites. Understandably, it is difficult to study the motion of CT states as they exhibit minimal direct absorption and typically weak photoluminescence, such that great care must be taken in generating and detecting the emission or photocurrent response of these states [83,84]. However, exciplexes, which are also electron-hole pairs delocalized across a donor-acceptor interface, possess stronger photoluminescence due to exhibiting TADF [85]. In fact, Deotare et al. used these strongly emissive states as an analog for studying CT state motion. However, these observations were limited to studying diffusion a single composition mixture of a single donor-acceptor system. To demonstrate the generality of exciplex and CT state diffusion more broadly, this thesis will employ several donor-acceptor systems with different mixture composition to provide methods of tuning and investigating the length scale of exciplex diffusion in Chapter 4.

2.5. Organic light-emitting devices (OLEDs)

2.5.1. Device principles

Organic light-emitting devices generate electroluminescence from injected charge carriers that bind to form excitons which radiatively recombine to emit light. These devices also employ multilayer stacks of organic semiconductors, with a simplified architecture shown in Figure 2.8 (a) [22,86]. In such a device, electrons are injected from the top metal contact into a layer of electron transport material (ETM), before reaching the emissive layer (EML), which is a composite of a host and guest material, often a wide-energy gap host doped with guest emitter molecule(s) [87]. Similarly, holes are injected into a layer of hole transport material (HTM) and then the EML. Energy transfer can lead to formation of different types of excitons which may lead to advantageous emission properties or may quench leading to enhanced nonradiative recombination. Radiative recombination gives rise to electroluminescence (EL), while non-radiative recombination leading to loss of energy as heat [28].

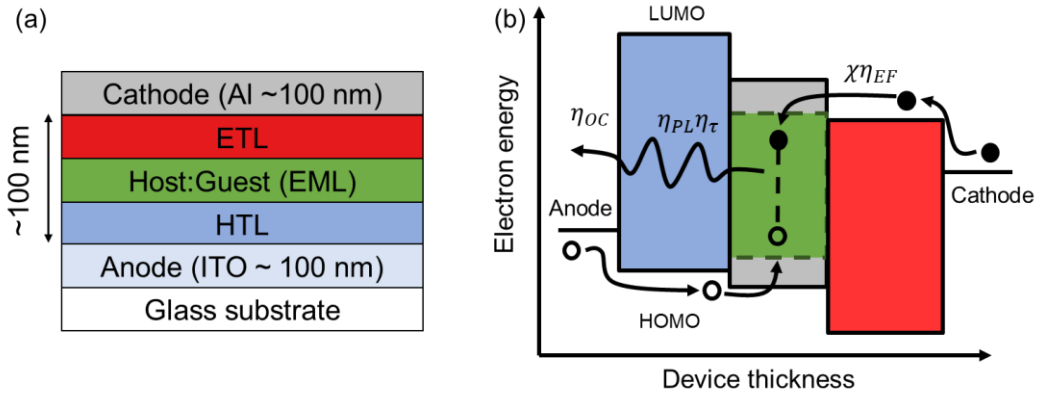

Figure 2.8 (a) Schematic of layer architecture of a simplified OLED (b) Energy level diagram of a simplified OLED. Electrons and holes are injected into hole and electron transport layers (HTL, ETL) and then reach the emissive layer (EML) where they bind to form an exciton. The exciton recombines emitting a photon which is outcoupled through the anode.

Additionally, unbalanced carrier transport can lead to carrier leakage across the device and recombination on non-radiative recombination centers reduced the by the exciton formation efficiency η_{EF}, also known as the charge balance factor [28,88]. Injected carriers form a mixture of singlet and triplet excitons, which may not all be emissive for a given emitter. This is called the radiative spin fraction χ, which is typically unity for phosphorescent and TADF emitters, but only ¼ for fluorescent emitters. The formed excitons will emit photons with a photoluminescence efficiency η_{PL} depending on intrinsic radiative and non-radiative recombination rates. Alternately, quenching via triplet-triplet, triplet-polaron, or other mechanisms can reduce the fraction of excitons that recombine on the intrinsic lifetime (τ) of the molecule, described by the natural decay efficiency η_{τ} [60]. Finally, emitted photons may be trapped in the devices by internal reflection into optical waveguide or substrate modes, or by coupling to surface-plasmon modes of the cathode, leading to only a fraction of photons being outcoupled η_{OC}. Outcoupling efficiencies are often ~20% for isotropic emitters, but can be improved to ~30% by careful alignment of emitter transition dipole moments [89,90]. A schematic of these processes are depicted in Figure 2.8 (b), and a summary of contributions to OLED external quantum efficiency is summarized as follows [60]:

$$\eta_{EQE} = \eta_{OC}\eta_{PL}\eta_{\tau}\chi\eta_{EF} \qquad (2.8)$$

In the emissive layer of an OLED, the selection of an emissive dopant must carefully balance the tradeoff between the radiative fraction of excitons (χ) and device stability, especially for high-energy excitons required for blue OLEDs [91]. Depending on the mechanism of emission for the guest emitter, less than 100% of formed excitons may luminesce, as touched upon in Section 2.2. The next section, 2.5.2, will discuss important

challenges and strategies to improve the radiative fraction of excitons formed in blue OLEDs.

2.5.2. Thermally activated delayed fluorescence and exciplexes

Although phosphorescent emitters have been developed to stably harvest 100% of excitons in green and red OLEDs [92–94], the realization of stable, efficient blue phosphorescent materials and devices has been challenging, due to the generation of long-lived high-energy excitons required for blue emission [91,95]. The incumbent technology for harvesting triplets for blue OLEDs is by using triplet-triplet annihilation, whereby two triplet excitons combine leading to the formation of one singlet exciton [91]. This two-to-one conversion however leads to only 62.5% of generated excitons being emitted as photons, as depicted in Figure 2.9 (a) [37].

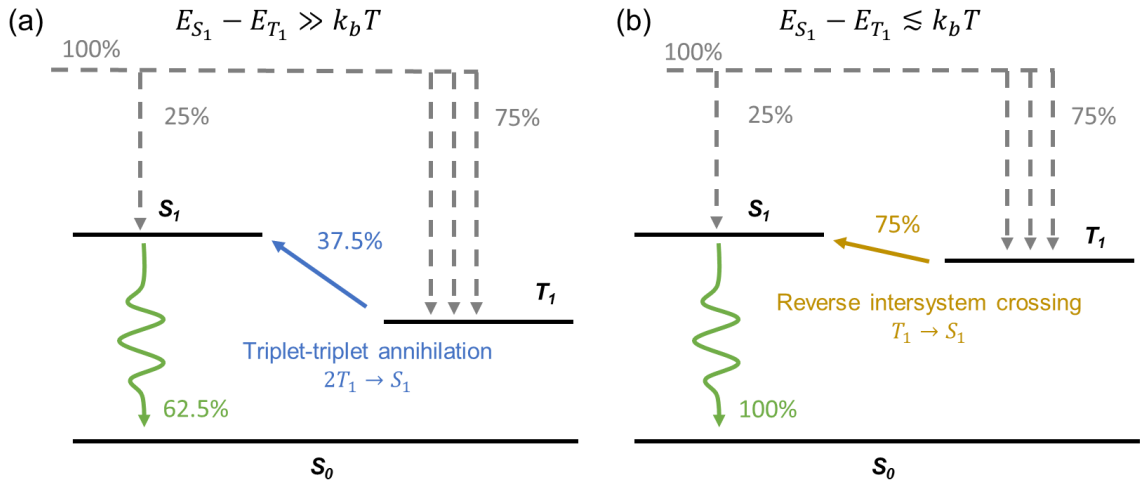

Figure 2.9 Triplet-to-singlet conversion mechanisms. Percentages reflect the amount of generated excitons, via electrical excitation, are involved in each process. (a) Triplet-triplet annihilation (TTA) converts two triplets into one singlet, which recombines radiatively. Note: Intermediate steps are excluded for simplicity. (b) Thermally activated delayed fluorescence (TADF) converts one triplet to one singlet via reverse intersystem crossing.

More recent work has sought to increase blue OLED efficiency through realization of one-to-one triplet-to-singlet conversion via a process called reverse intersystem crossing (RISC), as depicted in Figure 2.9 (b) [36,37,70,85,96,97]. Singlets generated by RISC can then fluoresce in a process called thermally activated delayed fluorescence (TADF) [70,98,99]. This process relies on thermal fluctuations to permit the endothermic RISC process, which can only occur in systems with exchange energy splitting comparable to k_bT, as can be found in CT state and exciplex systems (see Section 2.2.2) [70].

Additionally, TADF systems have been paired with fluorescent dopants to further increase the rate at which excitons recombine radiatively. This method is called hyperfluorescence, which takes advantage of the high radiative fraction of the host and the narrow-line width of guest to improve device efficiency, stability, and color purity [100–102]. A schematic of the exciton kinetics in a hyperfluorescent system are shown in Figure 2.10 (a) [100–102]. With several excited states available to a formed exciton, higher energy species will energy transfer to lower energy states either exciting a highly emissive guest or finding sites that quench luminescence. In the latter case, D-A interface states with energy lower than the desired emitter exciton can act as a sink for excitons leading to diminished efficiency or reduced color purity as in Figure 2.10 (b). In addition to the simplified three-state diagrams of Figure 2.10, several other local singlet and triplet energy levels of component materials are present and could contribute to emission quenching, where energetic alignment of excited states is a critical factor determining emission properties.

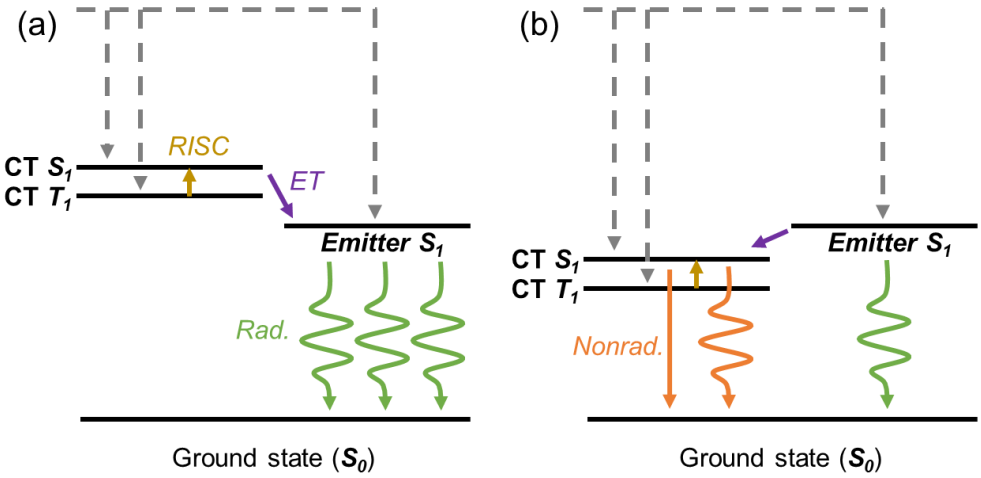

Figure 2.10 Simplified exciton energy diagrams for properly and improperly designed emitter-doped exciplex cohost systems (a) A hyperfluorescent system with an exciplex or CT state-forming cohost exhibiting reverse intersystem crossing that efficiently radiates photons from emitter excitons generated through energy transfer. (b) A system with lower exciplex energy that quenches emitter excitons to yield mixed emission color or lower emission through nonradiative recombination.

With the proliferation of OLEDs employing materials exhibiting TADF, detailed understanding of the energy and energy transfer of excitons in these materials is required to design efficient devices. A pair of reports explored the rate of exciplex TADF for several D-A systems, but questions remain regarding factors determining the exciplex energy for a given material pairing [70,103]. Additionally, Al Attar et al. noted unusual bias-induced shifts in emission energy from exciplex electroluminescence spectra of bilayer devices including m-MTDATA:3TPYMB [104]. However, a detailed investigation that decouples the role of injected polarons and applied field is lacking, leaving uncertainty regarding the origin of the emissive shifts. This thesis provides further studies of exciplex systems exhibiting TADF examining the exciplex energy, in Chapters 5 and 6, and energy transfer in Chapter 4.

2.6. Conclusion

This chapter has discussed important features of organic semiconductors and their optoelectronic devices including exciton energetics and energy transfer, types of excitons in pure of mixed phases, and the basics operating principles of organic photovoltaic and light-emitting devices. Particular focus is given to the phenomena of exciton diffusion and interfacial excitons that exhibit thermally activated delayed fluorescence, which will be studied in more depth in Chapters 4,5, and 6. Preceding this, relevant experimental techniques for sample fabrication and characterization are discussed in Chapter 3.

3. Fabrication and measurement techniques for organic thin films

Organic semiconductor devices rely on carefully designed architectures comprising nanometer scale thin films. Further, the electronic and photophysical properties of organic semiconductors are frequently studied in thin films via optical spectroscopies. This chapter will describe how organic thin films can be prepared, as well as detail a select few techniques that are essential for the investigation of the absorption, emission, and exciton energy transfer of organic semiconductor thin films.

3.1. Fabrication of organic thin films

Thin films of organic semiconductors can be prepared by solution-phase processing such as spin coating or printing of solvent solutions or suspensions, or vapor phase processing such as vacuum thermal evaporation from molecular powders [105]. Additionally, donor-acceptor heterojunctions of different organic semiconductors can be prepared as either mixtures, often referred to as bulk heterojunctions, or as bilayers, often referred to as planar heterojunctions [42,106]. Additionally, these heterojunctions exhibit a variety of emergent properties not observed in single-component films [47,85]. This section will detail how organic thin films and donor-acceptor heterojunctions are fabricated with precise composition and abrupt interfaces as well as introduce several processes and properties that can arise for excitons at donor-acceptor interfaces. Materials in this thesis are processed via vacuum thermal evaporation (VTE) which will be discussed further.

When organic molecular powders, with molecular weights between a few hundred to several thousand g/mol, are heated in high vacuum ($< 10^{-6}$ Torr) melting then evaporation

or direct sublimation can occur [105]. Common molecular classes deposited by this method include polyacenes, fullerenes, carbazoles, and metal complexes of phthalocyanines and various other ligands [35,42]. This evaporation can be carefully controlled by heating powders in a crucible or metal boat in a high-vacuum chamber with samples mounted on a nearby substrate holder, leading to deposition of material on the substrate. Deposition rates can be monitored using a calibrated quartz crystal microbalance (QCM) and feedback can be used to adjust heating to reach a desired deposition rate, typically on order of ~0.1-10 Å/s. A shutter can be used to abruptly begin or end depositions, allowing for depositions thicknesses of few to hundreds of nanometers and precision on the nm-scale. A schematic of a deposition chamber for high-vacuum thermal evaporation is shown in Figure 3.1.

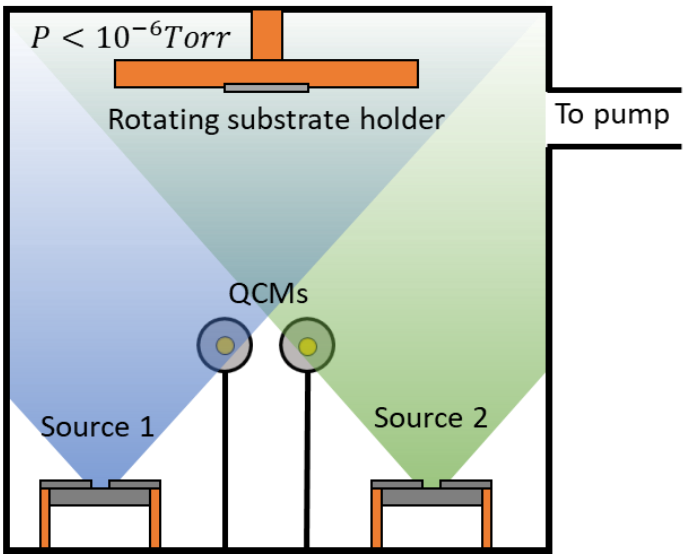

Figure 3.1 Schematic of a vacuum thermal evaporation chamber equipped for co-deposition from two sources of organic powder. Pressure is held below 10^{-6} Torr via a cryogenic pump attached to the chamber. Deposition rates are monitored using quartz crystal monitors (QCMs). Deposition occurs from each heated source on a substrate mounted on a rotating holder.

Further, mixed composition films can be prepared by simultaneous heating and deposition of multiple organic powders, with additional QCMs to monitor component deposition rates. Mixtures with doping levels as low as ~1 vol % can be achieved by co-

deposition of two components at different growth rates. Such low doping concentrations are essential in OLED emissive layers to limit fluorophore self-quenching [93,107]. Sample architectures with layers of different materials, of pure or mixed composition, can be fabricated by sequential deposition of each material or materials of interest. Additionally, various inorganic materials can be deposited similarly, such as metals like Al or Ag, metal oxides like MoO_3 or WO_3, or halides like LiF [108–110]. The ability to fabricate structures with insulating, semiconducting, and conducting properties allows for facile preparation of organic semiconductor devices with abrupt interfaces and carefully controlled thickness, allowing systematic study of material and interfacial properties with control over layer composition, thickness, and deposition rate.

3.2. Emission spectroscopy

Exciton recombination may lead to radiative emission via photoluminescence (PL). The associated emission spectra, which can be recorded by a spectrofluorometer, possess critical information about the electronic energy states that are occupied by excitons in a sample. A schematic of a spectroflurometry setup is shown in Figure 3.2, comprising a light-source, often a Xenon arc lamp, from which a specified excitation band of wavelengths is selected by using a monochromator or optical filter, to illuminate a sample which emits PL that is monochromated or filtered and recorded with a detector. Alternately, a charge-coupled device can be used to record an emission spectrum all at once using a diffraction grating. Analysis of emission spectra can provide information not only of what electronic transitions occur during recombination, but also reflect the influence of the surrounding environment of the emitter, such as solid-state solvation or quenching [111–113]. Finally, the intensity of PL can provide details as to what fraction of generated

excitons undergo nonradiative processes instead of emission. The radiative fraction of excitons can be quantified through measurement of the PL efficiency η_{PL}, the fraction of photons emitted per absorbed photon or generated exciton. It may also be described in terms of the radiative rate k_r of recombination and the nonradiative rate of recombination k_{nr}, or the exciton lifetime $\tau = \frac{1}{k_r+k_{nr}}$ as follows:

$$\eta_{PL} = \frac{Photons\ emitted}{Photon\ absorbed} = \frac{k_r}{k_r+k_{nr}} = k_r\tau \qquad (3.1)$$

PL efficiency may also be assessed in relative terms by comparison of emission intensities of similar samples, namely having the same radiative recombination rate and intrinsic lifetime, under the same illumination conditions. Differences in absorption can be treated with the thin-film optical model described in the next section. In such cases, the emission intensity of a pair of samples are compared to deduce the increased rate of non-radiative recombination via processes such as exciton diffusion to a quenching interface. This later approach forms the basis of photoluminescence quenching measurements of exciton diffusion lengths, which will be discussed in more detail later.

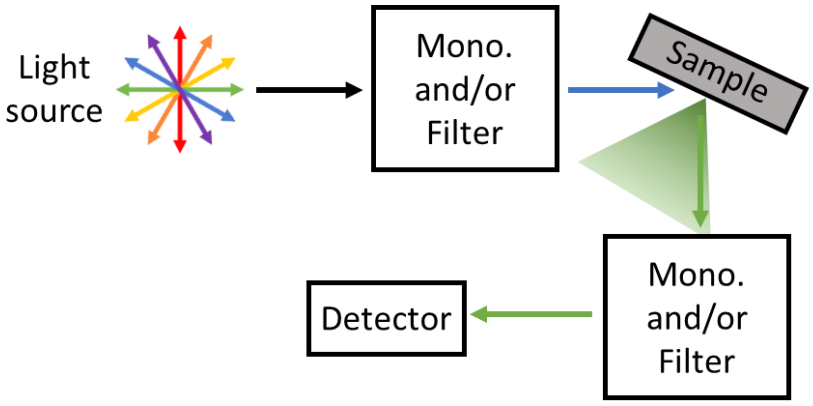

Figure 3.2 Schematic of spectrofluorometry measurement. A light source is monchromated or filtered to select a specific excitation band which illuminates a sample. The sample photoluminescence spectrum is collected as a function of wavelength using a monochromator and detector.

3.3. Ellipsometry

Ellipsometry is an optical measurement technique that can be applied along with a thin-film optical model to extract properties such as thicknesses and optical constants of thin film samples [53,65,114,115]. One ellipsometric set-up is depicted in Figure 3.3, where a beam from an unpolarized light source passes through a polarizer, reflects off a sample, and the reflected beam is analyzed with a rotating polarizer and detector. From this, the elliptical transformation of the reflection can be parameterized by either a complex-valued parameter (ρ) which is the ratio of complex-valued reflection coefficients for electric field components lying in and perpendicular to the plane of incidence (R_p and R_s, respectively). This complex-valued property can be expressed as two real valued quantities, Ψ and Δ, as in Equation 3.2:

$$\frac{R_p}{R_s} = \rho = \tan(\Psi)\, e^{i\Delta} \qquad (3.2)$$

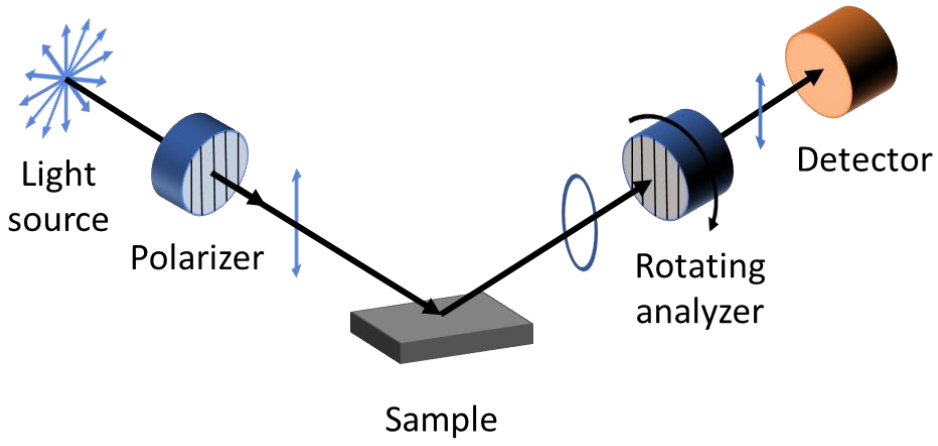

Figure 3.3 Schematic of ellipsometry measurement. A monochromated light source is polarized before reflecting off a sample. The reflected beam is collected by a detector after passing through a rotating analyzer. The time-varying detector signal is used to determine the polarization change due to reflection off the sample.

A monochromator between the light source and polarizer allows for spectral measurements, while a goniometer attached to the sample stage and detector arm allows

for angle-resolved measurements. Measuring Ψ and Δ at various wavelengths and angles can provide spectra that are sensitive to the complex indices of refraction and thicknesses of the thin-film sample layers. These spectra can be modeled using a thin-film optical model similar to the one described in the next section. The model can then be fit to the measured spectra to extract properties of interest. Deposited thicknesses of a given material can be calibrated using ellipsometry at wavelengths the sample does not absorb and fit using a Cauchy dispersion model [116]. Additionally, optical constants can be extracted using more complex dispersion models [69,115]. Relevant measurements in this thesis were collected using a J. A. Woollam VASE ellipsometer.

3.4. Transfer matrix optical model

Since the thickness of organic semiconductor films is often on the order of ~10-100 nm, interference must be considered to accurately predict optical phenomena. A transfer matrix model has previously been described by Pettersson et al. to determine the optical field intensity within a multilayer stack of thin-films with known optical properties [65]. This model has been applied to predict absorption spectra and exciton generation distributions within multilayer organic thin film samples and devices [69,117]. In this thesis, Pettersson's model is applied in conjunction with a one-dimensional exciton transport model to determine exciton diffusion lengths from luminescence quenching measurements.

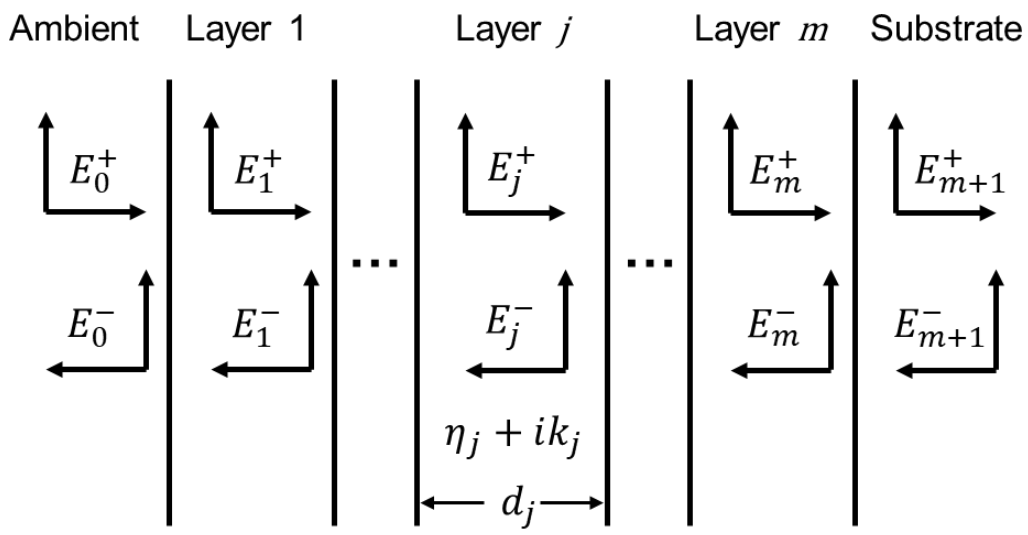

Figure 3.4 Electric field representation in a multilayer structure of thin films. The structure contains m layers of thickness d_j and complex indices of refraction $\eta_j + i\kappa_j$. Electric field vectors are represented by components in the forward propagating and reflected directions.

The model assumes optically isotropic and homogeneous layers that are planar with interfaces parallel to the substrate surface, as in Figure 3.4. The electric field in layer j is described by two complex-valued functions ($E_j^{\pm}(x)$), representing the magnitude and phase of the electric field at a given position (x) in the layer. One function represents the forward propagating electric field E_j^+, while the other describes the reflected field E_j^-. Fields can be normalized to the incident illumination field when comparing measurements under a common illumination condition, as in analysis of photoluminescence quenching experiments. Adjacent field vectors are related by 2 x 2 transfer matrix relations accounting for reflection at interfaces and propagation through bulk layers, dependent on layer thickness (d_j) and complex indices of refraction ($\eta_j + i\kappa_j$). For example, the reflected ambient field (E_0^-) and forward field at the sample-substrate interface (E_{m+1}^+) can be calculated from the forward ambient field vector (E_0^+), knowing that there is no back-side illumination ($E_{m+1}^- = 0$) as in Equation 3.3:

$$\begin{bmatrix} E_0^+ \\ E_0^- \end{bmatrix} = S \begin{bmatrix} E_{m+1}^+ \\ E_{m+1}^- \end{bmatrix} \qquad (3.3)$$

Where S is a 2 x 2 matrix product of interface and bulk propagation matrices and depends on layer indices of refraction and thicknesses. With the electric field functions of each layer, reflection coefficients and spectra can be computed.

For further modeling of exciton generation, the volumetric energy dissipation density Q, which can excite molecules in a given volume, can be calculated from the square of the magnitude of the total electric field at each point within a layer of interest as in Equation 3.4:

$$Q_j(x) = \frac{1}{2} c \epsilon_0 \alpha_j \eta_j \left| E_j^+(x) + E_j^-(x) \right|^2 \qquad (3.4)$$

Where c is the speed of light, $\alpha_j = \frac{4\pi\kappa_j}{\lambda}$ is the absorption coefficient, η_j is the real component of the index of refraction, and $\left| E_j^+(x) + E_j^-(x) \right|^2$ is the square modulus of the total electric field at position x of layer j. This dissipation density can be used with the transport model of Equation 2.6 to predict exciton density distributions for a layer with known optical properties and prescribes diffusion length. In this thesis, we employ measurements of samples with different boundary conditions, one reflecting and one quenching, example simulation results are shown in the next section.

3.5. Photoluminescence quenching

Photoluminescence quenching (PLQ) measures PL of a pair of organic thin films with complimentary exciton reflecting and quenching layers, like the samples I and II shown in Figure 3.5 (a). [58,62,66,117,118] By taking the ratio of total emission, found by dividing integrated spectra, of quenched (II) to unquenched (I) samples with known transport layer

thickness, L, and a prior unknown out-of-sample-plane L_D. A PL ratio (PLR) is defined as in Figure 3.5 (b). A PLR contains contributions from different absorption between I and II, arising from thin film interference, along with exciton dissociation at the quenching interface in II.

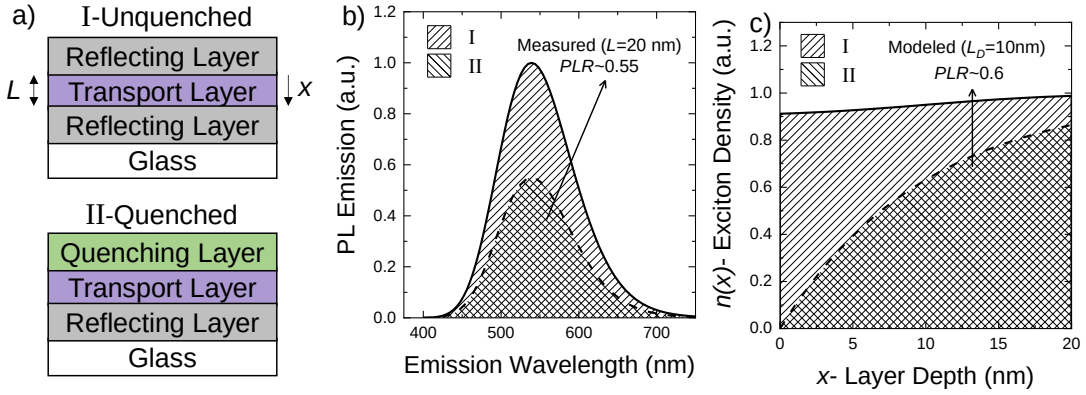

Figure 3.5 (a) Schematic of unquenched (I) and quenched (II) samples for PLQ, differing only by replacement of an exciton reflecting layer with an exciton quenching layer. (b) Typical PL emission spectra for I and II. (c) Modeled *n(x)* for I and II.

PLRs can be modeled by using the optical and transport models applied for organic thin-film structures mentioned in Section 3.4 given optical constants, thicknesses of individual films, and an assumed L_D. The unquenched film, I, is modeled using reflecting (homogeneous Neumann) boundary conditions at both ends, while the quenched film, II, has one boundary replaced by a perfect quenching (homogeneous Dirichlet) boundary condition which gives exciton density profiles, *n(x)*, where x is the distance from the exciton quenching/reflecting interface. Typical simulated profiles are shown in Figure 3.5 (c). Taking the ratio of spatially integrated density profiles of II to I yields a modeled PLR. Iterative nonlinear least-squares minimization of the difference between measured and modeled PLRs across several layer thicknesses is used to extract L_D. This method can be applied for mixtures with varying thickness (thickness-dependent PLQ) or for a range of

excitation wavelengths (spectrally resolved PLQ) and is extensively applied in Chapter 4. Relevant program code is provided in Appendix D. This method can be applied so long as emissive excitons diffuse through the bulk of the transport layer, as either a local exciton in a single-component film or an exciplex through a D:A mixture.

3.6. Conclusion

With the fundamentals of organic semiconductor thin film and device fabrication by vacuum thermal evaporation have been discussed. Additionally, emission spectroscopy for measurement of photoluminescence was discussed in the context of probing molecular and intermolecular excited states. Ellipsometry and transfer matrix modeling was mentioned for careful assignment of thin-film optical properties and optical modeling of thin-film interference. Finally, extraction of exciton diffusion lengths by photoluminescence quenching was discussed, as will be applied briefly in Chapter 4. The remaining chapters of this thesis will now outline recent discoveries of methods to tune excited state energy of exciplexes formed at organic donor-acceptor interfaces, via applied field, Chapter 5, and by varying film composition, Chapter 6.

4. Exciplex diffusion at donor-acceptor interfaces

Charge-transfer (CT) states formed at organic donor-acceptor (D-A) semiconductor heterojunctions play a critical role in optoelectronic devices [47]. While mobile, their migration has not been extensively characterized [80]. Further, the factors impacting the CT state diffusion length (L_D) have not been elucidated. Here, CT state L_D is measured using photoluminescence quenching for several D-A mixtures, with migration occurring along the bulk heterojunction. All D-A pairings considered yield a similar L_D ~5 nm in equal mixtures despite variations in the CT state energy and the constituent molecular structures. The CT state L_D varies strongly with mixture composition and is well-correlated with the slowest charge carrier mobility, suggesting a direct method to tune CT state transport. These findings may be applied to elucidate the role of CT state migration in organic photovoltaic and light-emitting devices, as well as to broadly explain the transport of interfacial excited states along inorganic and hybrid organic-inorganic heterojunctions. This work was completed in collaboration with Dr. Tao Zhang, with specific notes on data collected by Dr. Zhang.

4.1. Background

Bound electron-hole pairs formed at interfaces of dissimilar materials have been studied in heterojunctions of several classes of semiconductors including III-V semiconductors, transition metal dichalcogenide (TMDC) monolayers, organic-inorganic perovskites, and organic semiconductors [45,119–121], as well as hybrid interfaces combining materials types [122]. In inorganic semiconductors, such as III-V coupled

quantum wells and TMDC monolayer heterostructures, these delocalized excited states, termed indirect excitons, have been observed to diffuse over microns and have been exploited for the realization of novel optoelectronic devices [119,120]. The behavior of analogous states at organic semiconductor heterojunctions has been much less widely considered. In organic semiconductor heterojunctions, such interfacial charge-transfer (CT) states, also referred to as exciplexes, CT complexes or excitons [47,123], comprise a bound electron-hole pair delocalized across an electron donor-acceptor (D-A) interface [45]. Heterojunctions are a key component of organic optoelectronic devices, and consequently, CT states are often central to functions like electroluminescence and photoconversion. This work seeks to provide a mechanistic picture and design rules for controlling CT state diffusion in organic D-A heterojunctions.

Charge-transfer states can be important intermediates in both organic photovoltaic cells (OPVs) [47,124] and light-emitting devices (OLEDs) [125–127]. Further, CT state diffusion may play an important role in device functions like photoconversion and electroluminescence. In OPVs, dissociation of optically generated excitons leads to the formation of CT states that themselves must be dissociated to realize photocurrent and photovoltage. Several earlier works have demonstrated the experimental link between the measured maximum open-circuit voltage for a given D-A junction and the CT state energy [76,79,128]. In an OPV, a mobile CT state may more fully sample the D-A interface before recombining, offering an additional opportunity to align the state with the built-in field for dissociation into mobile charge carriers. OLEDs are frequently based on a composite emissive layer that combines a charge transporting host and a luminescent guest. An alternative approach has utilized a co-host design where an electrically generated

CT state (or exciplex) forms between the two host species before transferring energy to the guest. This approach has permitted improvements in turn-on voltage and peak efficiency, as well as efficiency roll-off [125–127]. In these devices, a long-diffusing CT state may more efficiently reach dilute, luminescent emitter molecules, improving exciton harvesting and device performance. Additionally, direct emission from intramolecular CT states exhibiting thermally activated delayed fluorescence (TADF) has been explored as an alternative paradigm for high-efficiency OLEDs [37,85]. Despite the ubiquitous role played by CT states in organic optoelectronic devices, there has been limited investigation of their transport behavior, and the specific materials and device parameters that can influence the CT state diffusion length (L_D).

Though confined to an interface, CT states have recently been shown to be as diffusive as their bulk exciton counterparts [80,129]. Deotare *et al.* used time-resolved photoluminescence (PL)-spreading techniques to observe the spatial diffusion of tightly bound CT states formed in equal D-A mixtures consisting of 4,4',4"-tris[(3-methylphenyl)phenylamino]triphenylamine (m-MTDATA) and tri[3-(3-pyridyl)mesityl]borane (3TPYMB). This system is well-suited for investigation using PL since this tightly bound CT state is characterized by singlet and triplet states that are closely spaced in energy and shows a high rate of radiative recombination relative to non-radiative recombination. This allows the normally non-radiative triplet CT states to undergo reverse intersystem crossing to the singlet CT state and efficiently yield delayed fluorescence [37,130]. Using this methodology, an in-plane CT state L_D ~ 5-10 nm was extracted for equal mixtures of m-MTDATA-3TPYMB. While fluorescent localized excitons typically hop by a dipole-mediated Förster process, the fluorescent CT states

present at D-A interfaces do not have strong absorption, and hence would exhibit exceedingly small rates of Förster transfer [58]. As such, prior work has argued for migration by sequential hoping of the constituent charge carriers, while remaining bound, along the D-A interface [80]. Previous work has treated the CT state as non-dissociative, which is supported by weak π- π stacking between the non-planar electron donor and acceptor molecules leading to weak electronic coupling and limitation of rapid, efficient exciton dissociation [131]. Additionally, subsequent work from Kim et al. has considered energy transfer of exciplexes between states with different donors and a mutual acceptor [81]. In that report they argue that exciplex energy transfer occurs via a Dexter-type energy transfer process, however then use of different donor components for the initial and final exciplex states and possibility that only hole transfer is occurring makes generalization to exciplex diffusion through a binary medium difficult.

The preliminary description of sequential carrier hoping, or asynchronous transfer, has been further supported theoretically in later reports by Lee et al. and Zhang et al., with the former directly expanding upon the model presented in Deotare et al., while the latter separately treats the motion of CT states along a linear D-A interface under a non-uniform electric field [80,82,132]. Although the later treatment focuses on a conjugated polymer donor and imposes a non-uniform electric field to drive transport, thus observing more rapid transfer, the authors separately find that so long as the CT state does not encounter fields strong enough to dissociate it, the CT state motion may proceed by asynchronous carrier transfer.

In the current work, CT state diffusion is examined for a series of D-A mixtures using PL quenching. These methods can be sensitive even to short values of L_D, and are applied

here to examine the role of CT state energy and D-A molecular structure in determining L_D. After first establishing the behavior of CT state diffusion across a range of D-A systems, varying mixture composition is demonstrated as a systematic approach to directly engineer L_D. This dependence is decoupled using measurements of CT state lifetime and the corresponding electron and hole charge carrier mobilities in the mixture. These measurements allow an explicit connection to be made to carrier hopping, a proposal of a mechanism for CT state transfer, and a demonstration of design rules for engineering transport.

4.2. Experimental methods

4,4',4''-tris[(3-methylphenyl)phenylamino]triphenylamine (m-MTDATA >99%), 4,4'-cyclohexylidenebis[N,N-bis(4-methylphenyl)benzenamine] (TAPC >99.5%), bathocuproine (BCP >99%), bathophenanthroline (BPhen >99.5%), tri[3-(3-pyridyl)mesityl]borane (3TPYMB >99%), tris(8-hydroxyquinolinato)aluminum (Alq_3 >99.5%), and 1,4,5,8,9,11-hexaazatriphenylenehexacarbonitrile (HATCN >99%) were purchased from Luminescence Technology Corporation Inc. Molybdenum (VI) Oxide (MoO_3 99.5%) and Al pellets (99.999%) were purchased from Sigma-Aldrich Corporation. N,N'-Bis(3-methylphenyl)-N,N'-diphenylbenzidine (TPD 99%) and lithium fluoride (LiF 99.995%) were purchased from Alfa Aeser. 4,4',4"-tris(carbazol-9-yl)triphenylamine (TCTA 98%) was purchased from TCI Chemicals. All materials were used as received, without further purification.

Samples for optical characterization were fabricated on glass substrates, while devices for electrical characterization were fabricated on glass substrates coated with a layer of indium-tin-oxide (ITO) from Xinyan Technology Ltd. with sheet resistance of ~15 Ω per

square. Substrates were cleaned sequentially in tergitol solution and organic solvents. Devices were exposed to UV-ozone for 15 min. All thin films were deposited by vacuum thermal evaporation at a base pressure below $8x10^{-7}$ Torr. Mixtures were deposited by co-deposition from multiple sources. All materials were deposited at rates of 0.1-2.5 Å/s. For electrical devices, a shadow mask was used to define a 1 mm diameter active area. To realize hole-only devices for space-charge limited current (SCLC) measurements, 5-nm-thick layers of MoO_x were deposited on either side of the organic active layer followed by a 100-nm-thick Al top contact. For electron-only devices, 1-nm-thick layers of LiF were deposited on either side of the organic layer along with a 30-nm-thick Al bottom contact and a 100-nm-thick Al top contact.

Film thickness and optical constants were obtained using a J.A. Woollam variable-angle spectroscopic ellipsometer (VASE). Steady-state photoluminescence was measured using a Photon Technology International QuantaMaster 400 Fluorometer with excitation from a Xe lamp under illumination at 70º with respect to sample normal. Transient photoluminescence decays were measured using Thorlabs APD430A Avalanche Photodiode Detector recorded on a Tektronix TDS5104B Digital Phosphor Oscilloscope, with excitation from an Optical Building Blocks N_2 (λ=337.1 nm) laser operating at 3 Hz with attenuated 1.67 mJ pulses of ~1 ns in width. Measured PL decays are fit to a biexponential decay, characteristic to D-A mixtures exhibiting delayed fluorescence [37], to extract the prompt and delayed lifetimes presented in Table S1. Current density-voltage characteristics were measured in air using an Agilent 4155C parameter analyzer. Additionally, measured J-V characteristics of single-carrier devices are fit to a model of

SCLC with Poole-Frenkel enhancement, $J = \frac{9}{8}\mu_0\epsilon\epsilon_0\frac{V^2}{d^3}e^{0.89\gamma\sqrt{\frac{V}{d}}}$ [133], to extract zero-field electron and hole mobilities (μ_0).

4.3. Measurement of exciplex diffusion length

4.3.1. Thickness-dependent photoluminescence quenching validation

Photoluminescence quenching is frequently applied to probe the diffusion of local, Frenkel excitons in either transient or steady-state configurations, as discussed in Section 3.5 [62,113,134–136]. Applied here is thickness-dependent PL quenching (TDPQ), which has been widely used to probe L_D in organic semiconductors [58]. TDPQ relies on comparing the steady-state PL intensity from the material of interest both with and without an adjacent quenching layer. Changing the active layer thickness varies the initial exciton generation profile, and a global fit of the measured PL ratio (quenched divided by unquenched) versus thickness yields L_D. The PL ratio is fit using a one-dimensional diffusion equation that includes generation and recombination [65]. In order to apply this methodology to CT states, the D-A mixture capable of generating CT states becomes the effective material of interest. While direct optical pumping of the CT state is inefficient, pumping of the local singlet exciton of m-MTDATA leads to rapid charge transfer to form the CT state [37,80]. CT states capable of diffusing through the mixture and reaching a quenching interface, here with a strong electron acceptor, undergo charge transfer and are dissociated. Alternately, CT states that do not reach the interface may recombine radiatively. A schematic of the diffusion-limited quenching pathway for CT states is shown in Figure 4.1 (a), with the architectures used for TDPQ shown in Figure 4.1 (b).

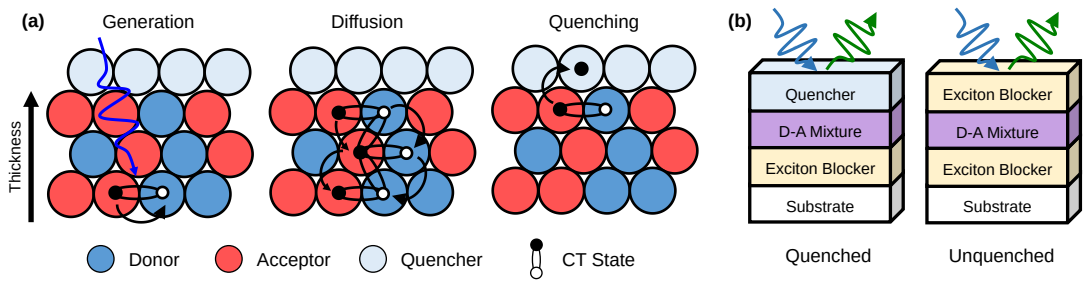

Figure 4.1 Photoluminescence quenching of charge-transfer states. (**a**) CT state generation, diffusion, and quenching pathway for thickness-dependent photoluminescence quenching (TDPQ) experiments. (**b**) Schematic of TDPQ quenching experiment.

In order to demonstrate TDPQ as a viable technique to probe CT state diffusion, initial investigation focused on probing equal mixtures of m-MTDATA-3TPYMB. Here, 10-nm-thick exciton blocking layers of 3TPYMB and a 10-nm-thick exciton quenching layer of 1,4,5,8,9,11-hexaazatriphenylenehexacarbonitrile (HATCN) are utilized [117]. Example unquenched and quenched PL spectra from m-MTDATA-3TPYMB thin films are shown in Figure 4.2 (a). Figure 4.2 (b) shows the resulting PL ratio as a function of mixture thickness yielding L_D = (5.0 ± 0.5) nm, consistent with prior work using PL spreading microscopy [80]. Although Deotare et al. reported the diffusion in the plane of the deposited layers, while our measurement is of diffusion out-of-plane, the agreement between L_D values further expresses the isotropy of mixtures formed between amorphous donor and acceptor components measured here. However, TDPQ measurements in systems with well-defined donor or acceptor domains, as are often employed in optimized OPVs, would likely underestimate the scale of L_D. In these systems, a high degree of anisotropy may be present and the diffusion length in each direction may differ substantially. Thus, TDPQ would measure only the projection in the out-of-plane direction. Further measurement of donor-acceptor bilayers may be employed to study diffusion along a well-oriented D-A interface. In-plane diffusion measurements, such as photoluminescence

spreading microscopy, would serve as key complements in fully characterizing such systems. TDPQ thus provides a simple, steady-state, technique to explore the role of the donor and acceptor in mixtures of varied composition with sensitivity on the nanometer scale. Additionally, the agreement between measurement and model in describing the TDPQ characteristic in Figure 4.2 (b) supports the description of CT state motion as by a single, tightly bound, mobile state.

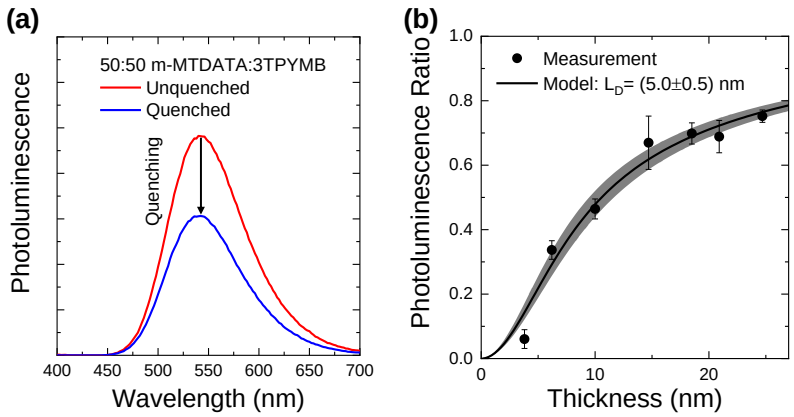

Figure 4.2 Photoluminescence quenching of charge-transfer states. (a) Photoluminescence (PL) spectra of pure donor (D) and acceptor (A) materials and D-A mixture showing red-shifted emission, evidencing complete CT formation. (b) Measured and modeled PL ratios for the equal D-A mixture of m-MTDATA-3TPYMB. Error bars on CT state diffusion length (L_D) represent one standard deviation of the fitted parameter, which is used to generate the shaded region for the modeled PL ratios.

Since generation of the CT state is accomplished by charge transfer from m-MTDATA, the motion of the local exciton prior to charge transfer may lead to an overestimate of the CT state L_D. To estimate the magnitude of the contribution, the L_D of neat m-MTDATA was measured using TDPQ. Figure B.1 of Appendix B shows measured PL ratios with corresponding fits for m-MTDATA yielding L_D = (4.8 ± 0.5) nm. In D-A mixtures, the contribution of the local m-MTDATA exciton will be substantially diminished due to CT state formation. This is confirmed by the lack of local exciton PL from equal D-A mixtures (Figure 4.2 (a)). Thus, it is concluded that the contribution of the

initially generated local exciton to the assigned CT state L_D is negligible, and that the absence of local emission can be further used to reinforce this conclusion for other mixtures.

A plausible impediment to the accurate assignment of the CT state L_D is the possible contribution of local exciton diffusion prior to formation of the CT state. Although measurable local exciton fluorescence would be expected with local exciton diffusion, we sought to further quantify this potential source of error. By using a range of monochromatic excitation wavelengths, the fraction of excitons that originate on the donor versus acceptor components in the mixtures may be systematically varied. If local exciton diffusion is significantly impacting the assigned CT state L_D, then a dependence of L_D on excitation wavelength is expected. A mixture of 25% m-MTDATA in BPhen was used to explore this effect as the two components have drastically different values of L_D in neat film (~5 nm vs. <1 nm, respectively) [137]. The high concentration of BPhen permits efficient exciton generation at smaller pump wavelengths, despite weak absorption relative to the smaller energy gap m-MTDATA. At smaller excitation wavelengths, most excitons are initially generated on BPhen. At larger excitations wavelengths most excitons originate on m-MTDATA. In mixed films, pumping of BPhen may also result in energy transfer to m-MTDATA. Even so, it is expected that if local exciton diffusion appreciably affects the assignment of L_D, then the extracted L_D of the CT state should show a dependence on excitation wavelength.

Figure 4.3 (a) shows the results of TDPQ for films of 25% m-MTDATA in BPhen with an exciton quenching layer of HATCN. LiF was used as the exciton blocking material, as excitation of the outside of the D-A mixture layer would confound further analysis. Under

each excitation condition, ranging from predominantly BPhen absorption to uniquely m-MTDATA absorption, extracted values of L_D are within ~5-7 nm. Additionally, spectrally resolved photoluminescence quenching (SRPQ) of 18-nm-thick mixtures are shown in Figure 4.3 (b) [113]. The spectral variation of the SRPQ characteristic reflects the difference in absorption of the film as seen in the case modeled without diffusion (L_D = 0 nm, dashed line). Thus, it is concluded that the contribution of the initially generated local exciton to the assigned CT state L_D is negligible and that the absence of local emission can be further used to reinforce this conclusion for other mixtures.

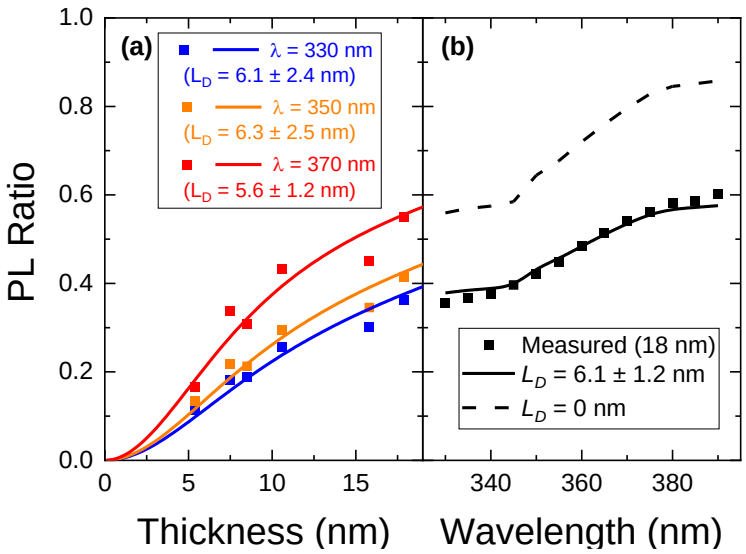

Figure 4.3 Photoluminescence quenching for a mixture of 25% m-MTDATA in BPhen at various excitation wavelengths. (a) Measured photoluminescence (PL) ratio as a function of mixture thickness (symbols) and the associated fit (line) at excitation wavelengths of λ = 330 nm, λ = 350 nm, and λ = 270 nm. (b) Spectrally resolved PL ratio (symbols), fit (solid line) and model excluding transport (dashed line) for an 18-nm-thick mixture.

Additionally, the possible effects of CT state dissociation should be considered in interpreting diffusion lengths in these measurements. An earlier report has noted spontaneous dissociation of CT states formed in D-A mixtures without external application of field to drive dissociation, although it is unclear what fraction of states dissociate at room temperature [138]. Dissociated CT states can be considered in our analysis in a few ways:

1) CT states that dissociate generate charges that move freely throughout the donor-acceptor mixture but contribute minimally to luminescence via non-geminate recombination and 2) dissociated carriers recombine non-geminately providing measurable luminescence. In case 1, whether few or many CT states are dissociated their products cannot be propped via luminescence measurements such as TDPQ and the dissociation of CT states can be considered as a non-radiative recombination or quenching process that reduced the exciton density and thus emission of both quenched and unquenched samples. In case 2, emission can be detected from non-geminate carrier recombination breaking the assumptions of Equation 2.6, namely that recombination occurs geminately. This equation would require modification and careful measurement of excitation fluence would be required to treat the dynamics of non-geminate charge carrier recombination, which will depend on the excitation density. Further, the dependance of PLQ characteristics on sample thickness would diverge from the typical characteristics of Figure 4.3 (a). However the close agreement of the TDPQ characteristics recorded in this chapter, especially of those measured at several excitation wavelengths and intensities of Figure 4.3 (a) suggest that the model of Equation 2.6 are sufficient to describe the diffusion and geminate recombination of CT states in the materials considered.

4.3.2. Donor-acceptor pairing and CT state migration

The excited-state recombination dynamics of D-A mixtures exhibiting delayed fluorescence have previously been shown to depend on the relative energetic alignment of the donor and acceptor local triplet energies and that of the CT state [85,130]. To explore the potential impact of the local triplet toward identifying the mechanism for CT state

transport, a series of acceptors were paired with m-MTDATA. Molecular structures for the electron acceptors tris(8-hydroxy-quinolinato)aluminum (Alq_3), bathophenanthroline (BPhen) and bathocuproine (BCP) in addition to 3TPYMB can be found in Figure 2.5. Figure 4.4 (a) shows PL spectra collected from equal mixtures of m-MTDATA and each acceptor excited at a wavelength of λ = 370 nm, leading primarily to excitation of m-MTDATA. All mixtures show broad, red-shifted PL with negligible m-MTDATA fluorescence, indicating efficient formation of the CT state. Figure 4.4 (b) shows the extracted L_D values for mixtures of m-MTDATA with the acceptors of Figure 4.4 (a) plotted as a function of CT state energy, also denoted are local donor and acceptor triplet energies extracted from literature reports of phosphorescence [37,85,139,140]. PL ratios for all m-MTDATA-acceptor mixtures can be found in Figure B.2.

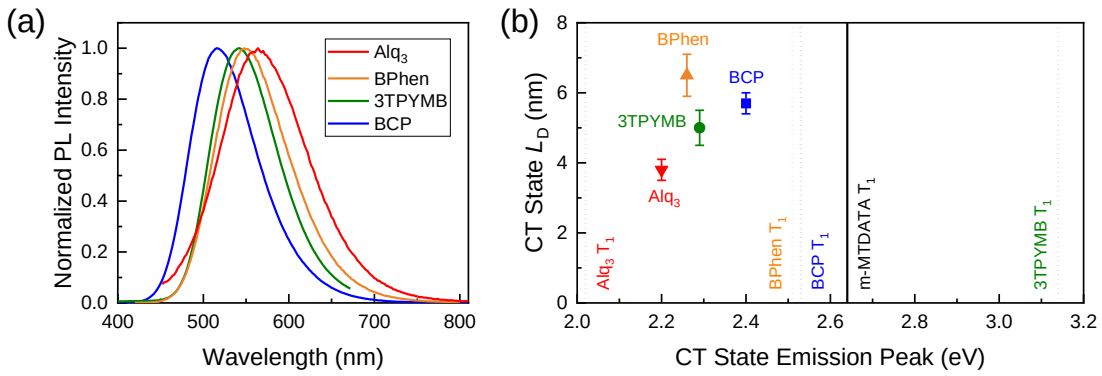

Figure 4.4 Acceptor sweep. (a) Photoluminescence (PL) emission spectra. **(b)** CT state diffusion length (L_D) measured by PL quenching as a function of CT emission peak energy for m-MTDATA-acceptor systems. Triplet levels (T_1) of donor and acceptor materials are also shown. Spectra for BPhen and BCP systems were collected by Dr. Tao Zhang.

Complementing the results of Figure 4.4, the role of the donor in determining L_D was considered by pairing several donor materials with the acceptor BCP. Besides m-MTDATA, BCP was paired with N,N'-bis(3-methylphenyl)-N,N'-diphenylbenzidine (TPD), 4,4'-cyclohexylidenebis[N,N-bis(4-methylphenyl)benzenamine] (TAPC) and

tris(4-carbazoyl-9-ylphenyl)amine (TCTA), whose structures are depicted in Figure 2.5. Figure 4.5 (a) shows the PL spectra collected from equal mixtures of the various donors and BCP. Finally, Figure 4.5 (b) shows the extracted L_D values for mixtures of BCP with the donors used in Figure 4.5 (a) plotted as a function of CT state energy, along with local triplet energies extracted from literature reports of phosphorescence [37,85,140,141]. PL ratios for all donor-BCP mixtures can be found in Figure B.3.

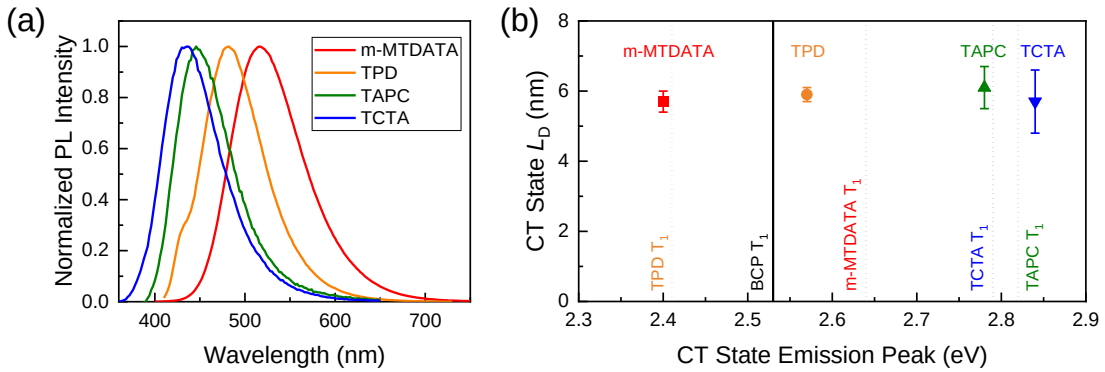

Figure 4.5 Donor sweep. (a) PL emission spectra. (b) CT state L_D as a function of CT emission peak energy for donor-BCP systems. Triplet levels (T_1) of donor and acceptor materials are also shown. These measurements were collected by Dr. Tao Zhang.

The acceptor sweep (Figure 4.4 (b)) with a donor of m-MTDATA reveals a moderate variation in L_D between ~4-6 nm with little variation in CT state energy. These mixtures form CT states with energies well below the m-MTDATA triplet, providing little access to this local state. As noted in Figure 4.4 (b), while the acceptor triplet levels vary considerably, no correlation is found with the CT state L_D [85,130]. For the corresponding donor sweep (Figure 4.5 (b)), some CT states lie above the triplet energies of BCP and several of the donors, offering a possible quenching pathway. Despite this, all pairings yield a similar CT state L_D. Further, the m-MTDATA-BCP CT state shows a nearly identical L_D to other donor-BCP systems despite having no deep-lying local triplets. Thus, it is concluded that relative energy alignment between the CT state and the donor and

acceptor local triplet levels has little impact on L_D, suggesting relaxation from the CT state to the triplet states does not occur appreciably. Further, the lack of any noticeable change in L_D despite the wide variation in CT state energy sampled in the acceptor (~2.2-2.4 eV) and donor (~2.4-2.8 eV) sweeps suggests that CT state energy alone is also not a primary factor determining L_D.

As noted previously, the low self-absorption characteristic of interfacial CT states frustrates efficient Förster energy transfer [58]. Similarly, the negligible spectral overlap between CT state emission and local exciton absorption in either the donor or acceptor material prevents migration of the CT state via Förster transfer to a local singlet state. Förster transfer is thus unlikely to be the transport mechanism for CT states. Additional work from Kim et al. considered exciplex energy transfer from TCTA:PO-T2T to m-MTDATA:PO-T2T in ternary mixtures to investigate transfer rates in these systems [81]. Their analysis of transient PL decays with varying m-MTDATA concentrations reveal that the energy transfer rate is much faster and scales differently with m-MTDATA concentration than Förster energy transfer would predict. They similarly conclude that exciplex energy transfer is unlikely to be dominated by Förster energy transfer.

An alternative transport mechanism is via Dexter electron exchange between CT states or between a CT state and a local triplet state [123]. The latter has been addressed above in analyzing the role of relative CT state and local triplet exciton energy on L_D. Some form of Dexter transfer between CT states via carrier exchange is thus the most likely mechanism. This is consistent with prior work [80], where a variation in electron-hole separation was described during CT state diffusion supporting a mechanism via asynchronous electron and hole transfer, whereby individual carrier transfer events lead to

a net displacement of the bound interfacial exciton. Further, other prior work has considered the transfer of local triplet excitons, for which Förster transfer is unavailable, by sequential electron and hole transfer processes, although ultimately finding this process to be inefficient due to the need to form a delocalized intermediate between the exciton donor and acceptor [142]. For CT state transfer, the initial and final states are already delocalized, so such a penalty is not born by using a delocalized intermediate, allowing this mechanism to progress at a significant rate.

4.4. Exploring the mechanism of exciplex diffusion

4.4.1. CT state migration and charge carrier hopping

The proposed link between charge transport and CT state diffusion leads to several deeper implications about how CT state L_D might be engineered. Of interest here is the potential link between experimentally measured values of the CT state L_D and the charge carrier mobilities in the mixture. For instance, if the CT state moves via an electron exchange mechanism at the D-A interface, motion of the slower charge carrier can limit CT state diffusivity as transport of both electron and hole is essential to complete each CT state hop. Such an explicit connection to the carrier hopping rate (via the mobility) can explain the results of the donor sweep with the acceptor BCP. Based on previous reports, BCP has a lower electron mobility than the hole mobilities of the donors shown in Figure 4.5 [143]. The slow electron motion in BCP would thus limit the CT state diffusion, leading to similar L_D regardless of donor. In contrast, m-MTDATA-acceptor systems show more variation in CT state L_D and hence can be used to further examine the role of the slowest moving charge carriers.

To explore the relationship between CT state diffusion and charge carrier hoping, the charge carrier mobilities of the component materials used in the acceptor sweep of this study were experimentally determined. Since TDPQ measurements are carried out under zero applied bias, the zero-field mobility is used to compare charge transport properties across different materials [133,144]. Space-charge limited current (SCLC) measurements have been previously used to extract carrier mobilities for a wide range of electron and hole transport materials, including several materials used in this study [143,145,146]. The zero-field mobility of holes in m-MTDATA and electrons in the acceptor materials were extracted using SCLC measurements, with measured and modeled current density-voltage characteristics found in Figure B.4. The neat film hole mobility of m-MTDATA is found to be $\sim 3 \cdot 10^{-6}$ cm^2/Vs, comparable to the literature report of $\sim 2 \cdot 10^{-6}$ cm^2/Vs [145], and notably exceeding the typical electron mobilities reported for common acceptor materials [143,146]. It is again suggested that in equal D-A mixtures, like those studied here, the low electron mobility of common acceptor materials limits the transport of CT states. The earlier presented values of L_D for equal D-A mixture films are compared to measured and literature values of the zero-field electron mobilities for the pure acceptor materials in Table 4.1. While appropriate SCLC data for 3TPYMB was not found in the literature, the higher zero-field mobility of 3TPYMB compared to Alq_3 has been previously established via time-of-flight measurements [147]. A clear correlation is observed in Table 4.1 with a larger acceptor electron mobility leading to increased CT state L_D when paired with m-MTDATA. It is thus concluded that improved electron mobility, through choice of acceptor material, improves CT state diffusivity and thus L_D. As CT state lifetime may

change drastically between D-A pairs, the role of CT state lifetime in determining L_D is considered explicitly in the next section.

4.4.2. Mixture composition and CT state migration

In establishing a correlation between the CT state L_D and the mobility of the slowest component carrier, a more rational process can be applied to engineering L_D. It is well-established that charge carrier mobilities in D-A mixtures depend strongly on composition, with the mobilities often showing variations over several orders of magnitude [148]. The composition dependence of L_D for CT states has not been previously reported, and in a naïve model might be expected to peak when the D-A interface area is maximized. Experimentally, a different behavior is observed for the dependence of CT state L_D on m-MTDATA concentration when paired with three different acceptors of BPhen, BCP and 3TPYMB (Figure 4.6). PL ratios for mixtures with various compositions are shown in Figure B.5, B.6, and B.7 of Appendix B. In all three cases, L_D increases with decreasing donor concentration. It should be noted that the diffusion length of 90% m-MTDATA in 3TPYMB shows very little quenching for the thicknesses measured, leading to a fitted L_D below 1 nm. This is likely below our threshold for accurate diffusion length assignment

Table 4.1 CT state diffusion length (L_D) and pure-component electron mobility (μ_0) for equal mixtures of m-MTDATA and various acceptors.

Acceptor	L_D [nm]	Measured μ_0 [$cm^2\ V^{-1}\ s^{-1}$]	Literature μ_0 [$cm^2\ V^{-1}\ s^{-1}$]	Ref
BPhen	6.5	4.4×10^{-7}	5.5×10^{-7}	[146]
BCP	5.7	2.1×10^{-8}	2.3×10^{-8}	[143]
3TPYMB	5.0	1.3×10^{-9}	/	/
Alq_3	3.8	9.7×10^{-10}	4.7×10^{-9}	[143]

but is nominally < 1 nm, and thus nearly immobile. The observed compositional dependence is consistent with the proposed transport mechanism since reduced donor concentration facilitates electron transport while also frustrating hole transport. More balanced carrier transport leads to a faster slowest carrier and increased L_D. For donor-rich mixtures, where electron transport is slowed, L_D shows a strong dependence on the acceptor material, with increased L_D observed for acceptors with larger neat film electron mobilities (Table 4.1). This indicates that electron transport is a limiting factor for CT state diffusion in equal and donor-rich mixtures.

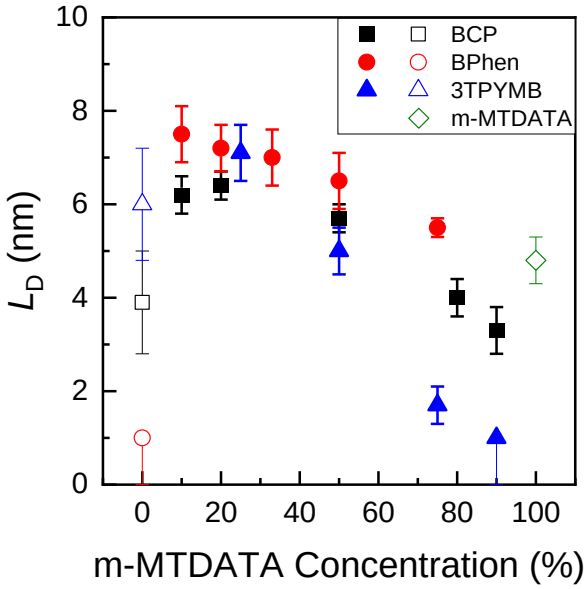

Figure 4.6 Impact of D-A composition. CT state diffusion length (LD) as a function of donor m-MTDATA concentration for three acceptor materials BCP, BPhen and 3TPYMB, shown as filled symbols. L_D of pure donor and acceptor local singlet excitons are shown as open symbols.

Figure 4.6 also indicates the local singlet exciton diffusion length of the donor m-MTDATA (L_D = (4.8 ± 0.5) nm) and the acceptors 3TPYMB (L_D = (6.0 ± 1.2) nm), BCP (L_D = (3.9 ± 1.1) nm), and BPhen (L_D < 1 nm) [137]. The TDPQ results of m-MTDATA and 3TPYMB can be found in Figure B.1, while BCP and BPhen have been previously reported [137]. It is noted that in equal mixtures, the CT states investigated here have

similar or longer diffusion lengths than their component materials, despite the CT state being unable to transfer by long-range Förster transfer. This likely reflects an increased excited state lifetime for the CT state due to increased delocalization and reduced electron-hole coupling, as has been previously observed for organic D-A CT states and inorganic interlayer TMDC excitons [37,120]. Delocalization realized through the formation of an interfacial excited state thus presents an opportunity to increase the exciton diffusion length for application in organic optoelectronic devices.

To better understand the dependence of L_D on composition in Figure 4.6, corresponding measurements of the carrier mobilities in D-A mixtures are required. The acceptor materials of interest here have low electron mobilities in neat film, complicating measurements in donor-rich mixtures. As such, the m-MTDATA-BPhen system, having the highest electron mobility acceptor, was selected to investigate the impact of carrier mobility on CT state diffusion. Additionally, for a fixed D-A system, we will show that the recombination dynamics and CT state lifetimes do not vary drastically with composition, allowing for the lifetime and diffusivity of the CT state to be decoupled. To investigate carrier mobilities, SCLC characteristics were measured for hole- (Figure 4.7 (a)) and electron-only (Figure 4.7 (b)) devices as a function of donor concentration and used to extract electron and hole mobilities. The hole and electron mobilities drop rapidly upon dilution of the donor and acceptor, respectively. To investigate CT lifetime across composition, transient PL decays of m-MTDATA-BPhen mixtures were collected as a function of donor concentration (Figure 4.7 (c)). Given the intersystem and reverse intersystem crossing between the singlet and triplet CT states, the measured transient PL reflects the dynamics of both states [37]. Importantly, the PL decay does not vary with

mixture composition, suggesting that the dependence of L_D on composition observed in Figure 4.6 for m-MTDATA-BPhen does not simply reflect a change in lifetime or a change in the balance of singlet and triplet CT state population. The extracted electron and hole mobilities along with prompt and delayed lifetimes are summarized in Table B.1 [85].

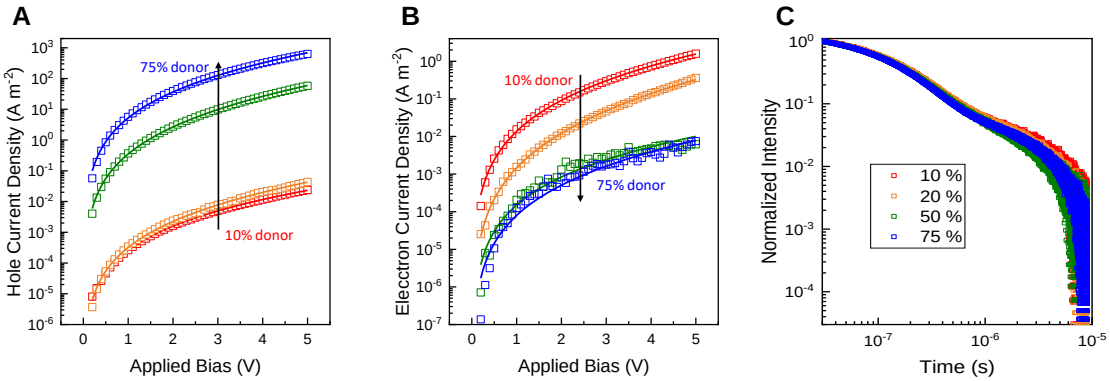

Figure 4.7 m-MTDATA-BPhen single–carrier device current-voltage and photoluminescence decay characteristics. (a) Hole-only current-voltage characteristics and space-charge limited current (SCLC) fitting as a function of donor m-MTDATA concentration. (b) Electron-only current-voltage characteristics and SCLC fitting as a function of donor concentration. (c) Transient photoluminescence decay as a function of donor concentration. These measurements were collected by Dr. Tao Zhang.

Having established that the diffusivity is varying with mixture composition, Figure 4.8 (a) shows the zero-field electron and hole mobilities measured by SCLC as a function of donor concentration along with measured CT state L_D. The electron is identified as the slowest carrier in equal mixtures and donor-rich compositions (μ_0^e ~ (0.9-2.5)·10^{-11} cm^2/Vs), while the hole is slowest for acceptor-rich compositions (μ_0^h ~ (3.0-3.4)·10^{-11} cm^2/Vs). The mobility of the slowest carrier increases and plateaus with decreasing donor concentration, consistent with the composition dependence of the CT state L_D. This result further suggests that the transport of the slowest carrier determines the diffusivity and thus L_D. To realize long-range transport of CT states, active materials with high charge carrier mobilities, especially acceptors with highly mobile electrons, are essential.

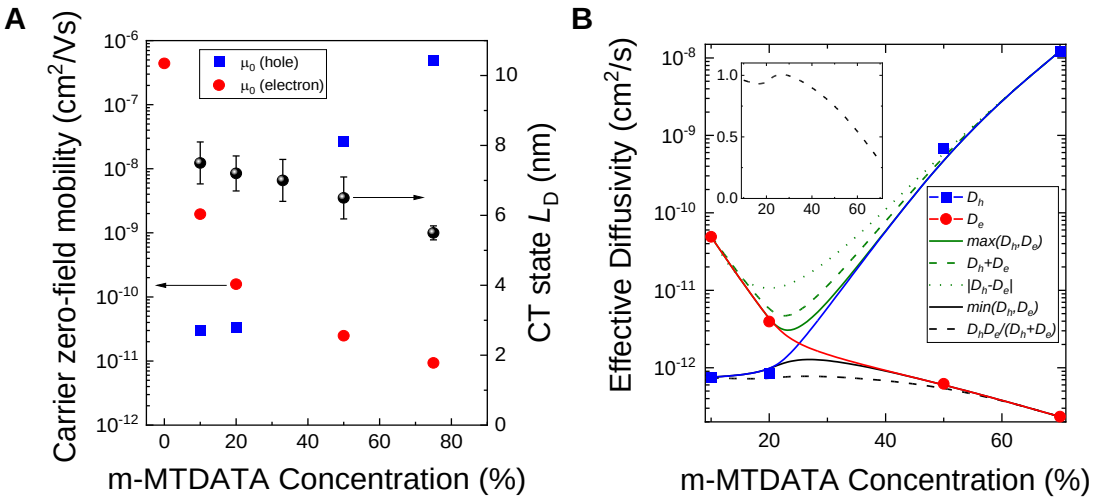

Figure 4.8 Dependence of CT state diffusion length and charge carrier mobilities on composition. (a) CT state diffusion length (L_D) and zero-field charge carrier mobilities as a function of composition for mixtures of m-MTDATA-BPhen**.** **(**b) Effective CT state diffusivities as a function of D-A mixture composition. Points are derived from mobilities, while guidelines are added for clarity. Several possible curves representing the CT state diffusivity are given as a function of the component mobilities for each concentration. Inset: Effective diffusivity from Equation 4.1 is normalized and reproduced on linear scale to show magnitude of variation with composition.

An alternate view of the relationship between carrier mobility and CT state diffusivity may suggest that the faster carrier mobility, a sum of mobilities, or a difference in mobilities may predict the ranking and variation of CT state diffusivities. In fact, a sum of carrier mobilities is used to describe the Langevin recombination and Onsager-Braun dissociation rates of excitons and CT states in organic semiconductors [51,149], In these processes, the fate of the composite CT state can be decided by the motion of just one carrier, i.e. if either the electron *or* hole dissociates or recombines, the geminate carrier is automatically dissociated or recombined. A schematic comparison of the predicted effective CT state diffusivity from the sum, difference and maximum carrier diffusivities, which are linearly related to the carrier mobilities by the Einstein relation [150], are shown in Figure 4.8 (b) (dashed, dotted, and solid green lines, respectively). We observe that the sum, difference, and maximum carrier diffusivities do not reproduce the observed ranking or scaling of CT state diffusion length across composition.

CT state diffusion differs from recombination and dissociation in that to accomplish coordinated motion between the electron and hole, i.e. motion of *both* carriers must occur to fully displace the state. If we use carrier diffusivity as a proxy for carrier transfer rate, we may express the probability of a charge transfer event involving a given carrier comprising a CT state, P_{h-t} and P_{e-t} in terms of the hole diffusivity (D_h) and electron diffusivity (D_e) as: $\mathrm{P_{h-t}} = \frac{\mathrm{D_h}}{\mathrm{D_h+D_e}}$, $\mathrm{P_{e-t}} = \frac{\mathrm{D_e}}{\mathrm{D_h+D_e}}$. Full transfer of the CT state requires both electron *and* hole transfer, thus the probability of this process follows the product of each component transfer probabilities as: $P_{CT-t} \propto P_{h-t}P_{e-t}$. Further, the probability of the CT state transfer (P_{CT-t}) may be analogously defined in terms of an effective diffusivity (D_{CT}) of the composite state by: $P_{CT-t} = \frac{D_{CT}}{D_h+D_e}$. These relations may be further applied to predict the scaling of the effective CT state diffusivity in terms of component carrier diffusivities as in Equation 4.1:

$$D_{CT} \propto \frac{D_h D_e}{D_h+D_e} \qquad (4.1)$$

This is an expected result for a process, i.e. CT state transfer, that results from two other processes occurring in sequence, i.e. electron and hole transfer, by the harmonic mean of the component rates, proxied by diffusivities. In the limit of highly-mismatched carrier transfer rates and diffusivities, the exciton transfer rate is limited by the slowest carrier, and thus the scaling of Equation 4.1 reduces to $D_{CT} \propto min(D_h, D_e)$, which we earlier concluded from our measurements in terms of mobilities.

The predicted effective CT state diffusivity given by the precise form of Equation 4.1 or the approximate minimum carrier diffusivity are also shown in Figure 4.8 (b) (dashed and solid black lines, respectively) and do indeed to follow the trend in L_D and thus

diffusivity implied by Figure 4.8 (a). The effective CT state diffusivity from Equation 4.1 is reproduced on a linear scale in the inset of Figure 4.8 (b). The effective diffusivity is reduced by two-thirds across composition, which by $L_D \propto \sqrt{D_{CT}}$, would predict a ~42% reduction in L_D, while a ~27% reduction is measured by PLQ, slightly overestimating the variation. The mismatch between the predicted and measured variation of L_D may be due to a slight change across composition of the Einstein relation factor or an enhancement factor, which are noted in the following section. Although Equation 4.1 and the following approximate limit are only subtly different, we presume that the observed extension of L_D with an increase of the slowest carrier mobility or diffusivity reflects that the CT state transfer rate follows the composite probability of electron and hole transfer.

4.4.3. Interpretation of the scale of CT state migration

With a qualitative relationship between carrier motion and CT state motion established, a quantitative analysis of carrier and CT state diffusivities can provide insight into a microscopic picture of diffusion. CT state diffusivity (D_{CT}) may be calculated from the diffusion length (L_D) and lifetime (τ) by $D_{CT} \sim \frac{L_D^2}{\tau}$ [58], and is of order ~10^{-6} cm^2/s for m-MTDATA-BPhen. Minimum carrier diffusivities may be calculated from the zero-field mobility using the Einstein relation and are of order ~10^{-12} cm^2/s in m-MTDATA-BPhen, as shown in Figure 4.8 (b). Although the Einstein relation has been shown to only be approximate in organic semiconductors and varies with charge density, the relation holds to within approximately a factor of ten [150].

The CT state diffusivity in m-MTDATA-BPhen is ~10^6 times larger than the value calculated from the zero-field carrier mobilities. This enhancement may reflect the

influence of the other carrier present in the CT state, and its role in creating a local electric field comparable to or larger than those that can be applied externally. Indeed, Yasuda *et al.* has shown a field enhancement of up to 10^5 times to the electron mobility in BCP, strengthening the argument for a role played by the mutual interaction of component carriers in determining the CT state diffusivity [143].

As the transfer rate of CT states far exceeds that of single carriers without an applied field, the proposed field-enhanced carrier transfer must occur efficiently and with minimal rate-limiting energy barriers. Deotare *et al.* previously described displacement of the CT state occurring through an "inch-worm"-like motion of the component carriers [80]. In this picture, the CT state may elongate and contract in successive carrier transfer events while remaining bound. Elongation of the CT state would involve endothermic hops to balance a reduction in binding energy.

Alternately, in a D-A mixture, multiple donor molecules may surround a single acceptor molecule or vice-versa. This provides several approximately iso-energetic sites for the electron and hole at a fixed electron-hole separation and thus binding energy. Successive carrier hops to neighboring molecules are possible without an endothermic elongation of the CT state to drive motion. Additionally, energetic disorder may further impact transport as low energy sites may be more easily sampled, but is not the primary driving force for motion, which is the multiplicity of approximately iso-energetic donor and acceptor sites. Repeated sampling of degenerate CT state configurations leads to diffusive motion of the CT state. This mechanism does not require infrequent large endothermic hops to drive transfer and thus likely dominates the motion of CT states. It is expected that the true trajectory of many CT states falls somewhere between these two

extremes of elongation/contraction and fixed-length transfer. With a deeper understanding of the rate at which CT states transfer, we have presented a clearer picture of the path that carriers and CT states may follow in traversing the D-A heterointerface.

4.5. Summary and conclusion

4.5.1. Implications for OPVs and other materials systems

We may further predict how CT state diffusion, which occurs in tandem with other processes such as geminate recombination and dissociation, may impact the operation of organic photovoltaic devices. The D-A heterojunction of an OPV provides a variety of relative donor-acceptor orientations and thus a distribution of recombination and dissociation rates for residing CT states [151]. The ability to sample several donor-acceptor pairs presents a method for CT states to redistribute amongst these sites, beyond those initially populated via exciton dissociation. It is thus possible that diffusion of the CT state provides a further relaxation pathway, akin to the concomitant red-shift described by Deotare et al. [80], favoring geminate recombination. Alternately, in their transit, the CT state may reorient relative to the built-in-field of the device, possibly favoring dissociation into mobile charge carriers. As these mechanisms, and likely more, represent competing influences on CT state dissociation, it is not immediately clear if CT state diffusion provides a net positive or negative impact on photocurrent generation, and thus further work is required to quantify the impact of CT state diffusion in devices and decouple these effects.

Alternately, the explicit connection made here between CT state diffusion and charge carrier transfer can also help to explain previous reports of long-distance diffusion of

interfacial electron-hole pairs in crystalline organic, inorganic, and hybrid heterojunctions. The CT state formed in a donor-acceptor co-crystal of distyrylbenzene derivatives was observed to diffuse over 30-40 nm [129]. Hybrid organic-inorganic CT states formed between the transition metal dichalcogenide (TMDC) monolayer WS_2 and tetracene have shown diffusion over 450 nm [122], while diffusion exceeding ~5 μm has been reported for the interlayer exciton between monolayers of WSe_2 and MoS_2 [120]. Using our work and literature reports of these diverse systems, CT state diffusivities (D) may be estimated from the diffusion length (L_D) and lifetime (τ). [58] These properties are summarized in Table 4.2 and estimate CT state diffusivities to be of order 10^{-6}, 10^{-3}, 1, and 10^{2} cm^2/s for amorphous D-A mixtures, D-A co-crystals, hybrid organic-inorganic TMDC heterostructures, and inorganic TMDC heterostructures, respectively. It is concluded that bulk crystallinity, which may improve both electron and hole mobility, drastically improves CT state diffusivity. Additionally, separating donor and acceptor materials into pure and ordered phases, providing high mobility for electrons and holes, likely leads to further improvements in diffusivity. The connection between carrier mobility and CT state diffusivity suggests a general need for high mobility donor and acceptor components to drive a long diffusion length.

Table 4.2 Comparison of interfacial exciton diffusion lengths across material systems

Material Type	Crystallinity	Donor Material	Acceptor Material	CT L_D (nm)	Lifetime (ns)	Diffusivity (cm^2/s)	Ref
Organic	Amorphous	m-MTDATA	BPhen	6	150-2000	$\sim10^{-6}$	/
Organic	Cocrystal	4M-DSB	CN-TFPA	30-40	17	$\sim10^{-3}$	[129]
Organic/Inorganic TMDC ML	Polycrystal/ TMDC ML	Tetracene	WS_2	450	2	1	[159]
Inorganic TMDC ML	TMDC ML	MoS_2	WSe_2	5500	~1	$\sim10^{2}$	[158]

CN-TFPA: (2Z,2′Z)-3,3′-(1,4-phenylene)bis(2-(3,5-bis-(trifluoromethyl)phenyl)acrylonitrile), 4M-DSB: 1,4-bis(3,5-dimethylstyryl)-benzene, TMDC ML: Transition metal dichalcogenide monolayer

4.5.2. Conclusions

In summary, the diffusion of CT states is measured via thickness-dependent photoluminescence quenching and is found to vary depending on the component charge carrier mobilities. CT state diffusivity is shown to trend with the slowest carrier mobility in the mixture. Other factors like CT state energy, Förster energy transfer and access to local triplet levels do not significantly impact CT state diffusion. These results suggest that CT states move through an electron exchange mechanism along the D-A interface. The motion is described as, potentially field-enhanced, sequential carrier transfer between neighboring donor and acceptor molecules. This work also explains trends observed in the literature for the diffusion of CT states in a broader range of excitonic materials, including organic D-A co-crystals and transition metal dichalcogenide monolayer heterostructures. This work finds that in order to maximize CT state diffusivity, the carrier mobility of the slowest carrier must also be maximized.

5. Field-induced emissive shifts at donor-acceptor bilayer interfaces

The giant Stark effect for organic donor-acceptor exciplex photoluminescence (PL) is observed with shifts of ~10-100 meV via electric fields from applied bias and photogenerated charges. Electrostatic modeling reveals an excited state dipole moment of 1.25 e·nm (60 Debye) for the archetypical electron donor-acceptor pairing of 4,4',4''-tris[phenyl(m-tolyl)amino]triphenylamine (*m*-MTDATA)-tris(2,4,6-trimethyl-3-(pyridin-3-yl)phenyl)borane (3TPYMB). The intermolecular nature of the exciplex enables shifts that exceed those reported for bulk excitons in organic semiconductors and interlayer excitons of transition metal dichalcogenide bilayers. Successful tuning of the dipole moment and giant Stark effect is realized by diluting the donor-acceptor bilayer with a wide-energy gap material. These findings expand the range of methods available to realize electrical control over exciton behavior.

5.1. Background

The interlayer nature of excited states in diverse material systems including III-V semiconductor, transition metal dichalcogenide (TMDC), hybrid two-dimensional (2D) inorganic-organic, and multilayer 2D perovskites has led to the observation of a variety of emergent exciton physics not displayed by the constituent materials such as exciton condensation [152,153], exciton-exciton repulsion [154–157], long-range diffusion [156–159], and the giant Stark effect (GSE) [160–163], among others. In particular, GSE permits profound tunability of exciton energy (E) via an applied electric field (F) mediated by an interlayer excited state dipole moment (μ) as: $\Delta E = -\vec{\mu} \cdot \vec{F}$ [164], often exceeding the

scale of the common linear Stark effect by an order of magnitude or greater. Amongst the largest GSE observations, multilayer TMDC photoluminescence (PL) has displayed large energy shifts up to $\Delta E = 80$ meV for electric field strengths up to $\left|\vec{F}\right| = 200$ mV/nm (2 MV/cm) [161,163]. Such shifts, as well as other emergent interfacial excitonic properties in TMDCs, owe their origin to the delocalization of the electron-hole pair across the layered interface, leading to large dipole moments on order of $|\vec{\mu}| = 0.5$ e·nm (25 D).

However, organic bulk excitons, important in the operation of organic optoelectronic devices such as photovoltaic cells (OPVs) and light-emitting devices (OLEDs), only display a small linear Stark effect with dipole moments of order 0.1-0.2 e·nm (5-10 D) providing shifts below 10 meV, limited by the highly localized nature of their Frenkel-type excitons [165,166]. However, intermolecular and interlayer excitons may form at organic electron donor-acceptor (D-A) interfaces and are termed charge-transfer (CT) states or exciplexes, which possess spatially delocalized electrons and holes, potentially better suited to exhibit the giant Stark effect. In fact, prior work on exciplex electroluminescence (EL) in OLEDs with D-A bulk and interfacial heterojunctions has observed a bias-induced sensitivity of emission energy, but a detailed investigation and connection to the applied field that decouples the role of injected polarons is lacking, leaving open questions regarding exciplex GSE existence and scale [104].

As critical intermediates in the operation of organic photovoltaic cells (OPVs) and OLEDs, D-A interfacial excited states have been intensely studied for their energetic [79,103,167], formation [36,47], transport [80,168], dissociation [47,51], and emergent properties such as thermally-activated delayed fluorescence (TADF) [36,47]. Recent advances in OPV heterojunction design have reduced the required interfacial

energy offsets for efficient charge generation to 10's of meV, while dissociation barriers of several meV have been measured [78,169]. In OLEDs, prior studies of exciplexes showed that 10's of meV can determine whether a given system exhibits TADF, providing efficient emission, or are otherwise quenched by local triplet states [85,167]. In OPVs and OLEDs, internal fields which often exceed 10^5 V/cm (10 mV/nm) [51,52,170] could lead to 10's of meV changes in interfacial state energies, enough to meaningfully impact device performance, if interfacial states possessed dipole moments of even 1 e·nm.

In this chapter, we quantify the behavior of interfacial exciplex luminescence under the influence of an applied field to demonstrate the giant Stark effect. We observe a reversible and field-dependent blue shift of exciplex emission energy in non-injection-type devices over a wide range of applied fields. We further explore the effect of a reverse-bias pulse on exciplex emission energy in our devices, identifying a transient blue-shift upon bias removal. Finally, solid-state dilution of the donor and acceptor layers is demonstrated as a method to tune the magnitude of the effect by modulating the dipole moment, leveraging the sensitivity of the delocalized excited state to the surrounding environment to manipulate the magnitude of the GSE with respect to field for a given donor-acceptor pairing.

5.2. Experimental methods

5.2.1. Sample preparation and analytical framework

To observe the GSE for organic exciplexes two measurement considerations must be met: I) an exciplex-forming medium must be excited, and the energy of the resultant exciton must be recorded, and II) a tunable, independently calculable electric field strength must be applied to the excitonic medium. Criterion I has been met in previous work by

measuring the photoluminescence of, amongst others, the exciplex formed between the HOMO of the electron donor 4,4',4"-tris[phenyl(m-tolyl)amino]triphenylamine (*m*-MTDATA) and LUMO of the electron acceptor tris(2,4,6-trimethyl-3-(pyridin-3-yl)phenyl)borane (3TPYMB. The donor-acceptor combination of *m*-MTDATA-3TPYMB has been thoroughly studied for its intense green exciplex emission when excited in the near ultraviolet [37,168]. Criterion II can be achieved by placing layers of an insulating material, such as lithium fluoride (LiF) [171], between the exciplex-forming medium and the electrodes, frustrating charge injection while applying an out-of-plane electric field [Fig. 1(b)]. By minimizing the charge density within the insulated bilayer, a linear relationship between the electric field ($F_{D/A}$) at the donor-acceptor interface and applied bias (V) is derived as a function of insulator, acceptor, and donor layer thicknesses (t_{Ins}, t_A, t_D respectively) and dielectric constants ($\epsilon_{D/A}, \epsilon_{Ins}$ respectively and further detail can be found in Appendix C.2) [172]:

$$F_{D/A} = \frac{V}{\frac{\epsilon_{D/A}}{\epsilon_{Ins}} t_{Ins} + t_A + t_D} \qquad (5.1)$$

Since prior work on organic exciplexes has established the ability of moderate-to-large electric fields (1-100 mV/nm) to dissociate excited donor-acceptor excitons [51,149], special care must be taken to limit field-induced emission quenching. This can be achieved by sequentially depositing the acceptor 3TPYMB and donor *m*-MTDATA, via vacuum thermal evaporation, such that an exciplex would be oriented with the hole on the high-electric-potential side of the heterojunction. A molecular orbital energy level diagram for devices fabricated on patterned indium-tin-oxide (ITO) coated glass substrates with the architecture: glass/ITO/LiF/3TPYMB/*m*-MTDATA/LiF/Al is shown in Figure 5.1 under

forward bias, here defined as positive bias between the top Al and the bottom ITO electrodes. The resulting electric field favors carrier association, limiting dissociation of the exciplex formed between the hole in the donor layer and the electron in the acceptor layer. Devices were fabricated by thermal vacuum evaporation of organic powders on ITO-coated glass.

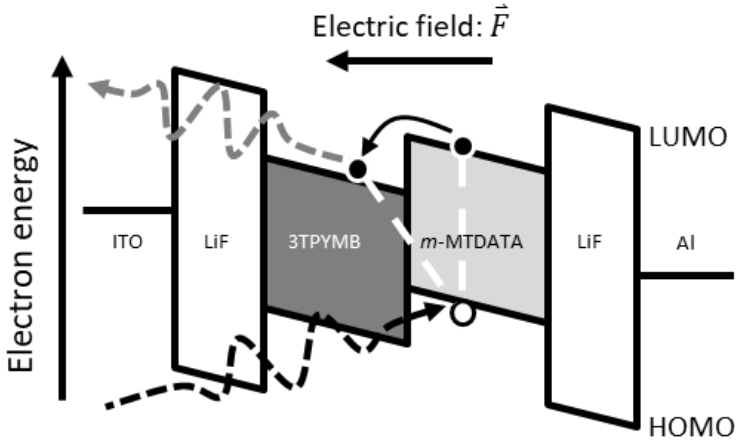

Figure 5.1 Electronic energy diagram of a non-injection-type device displaying exciplex photoluminescence. Absorption leads to exciton formation on *m*-MTDATA, with exciplexes formed via D-A charge transfer, leading to exciplex emission. An electric field is applied within the device by external bias between of the ITO and Al contacts.

5.2.2. Biased photoluminescence setup

Intrinsically low exciplex absorption makes direct optical excitation challenging for observation of photoluminescence and the GSE. Instead, optical excitation occurs exclusively in the donor layer of *m*-MTDATA at a wavelength of $\lambda = 370$ nm from a laser-driven light source leading to formation of bulk excitons (extinction coefficient spectra are provided in Figure C.1 of Appendix C) which subsequently undergo charge-transfer at the donor-acceptor interface to form exciplexes. Exciplex photoluminescence is optically filtered to remove scattered pump light and collected into a fiber-coupled, thermoelectric-cooled CCD spectrograph. Spectra are collected for a range of applied biases, and thus applied fields, in batches of 5 averaged spectra each with 200 ms of integration, selected

to minimize sample exposure and possible degradation. It is observed that significant fluctuations in the LDLS light intensity led to unstable absolute sample PL intensity, thus in this work spectra are normalized to the intensity of PL from local excitons that do not form exciplexes. While the relative emission intensity of the exciplex compared to local exciton emission is more consistent during testing, sample-to-sample variations have been observed, thus we limit our discussion of emission intensities as a function of applied field to normalized spectra from individual samples. As expected, fluctuations in illumination intensity had no effect on extracted exciplex energies.

The biased photoluminescence setup is home built, and a photograph of the system is shown in Figure 5.2. This includes a broadband white light laser driven light source (LDLS, Energetiq EQ 99X). The white light is focused to a ~2 cm excitation spot, which passes through a long-pass filter to select the excitation wavelength band. The light can then pass through a neutral-density filter mounted on a wheel equipped with filters for ND 0.5-2.5 or it may pass through unattenuated. The light finally passes through an aperture iris which provides an excitation spot ~1 mm in diameter before reaching the device sample area defined by a shadow mask. The sample luminescence is biased with electrical leads connected to a Keithley SourceMeter and emission is collected through a lens, a long-pass filter that removed stray excitation light, and then a microscope objective (NA 0.65) focuses the beam into a fiber optic cable coupled to the CCD spectrograph (Princeton Instruments FERGIE). Collection is automated using home-built software controlled written in Python, which was originally developed by Dr. John Bangsund and edited by the author for custom use.

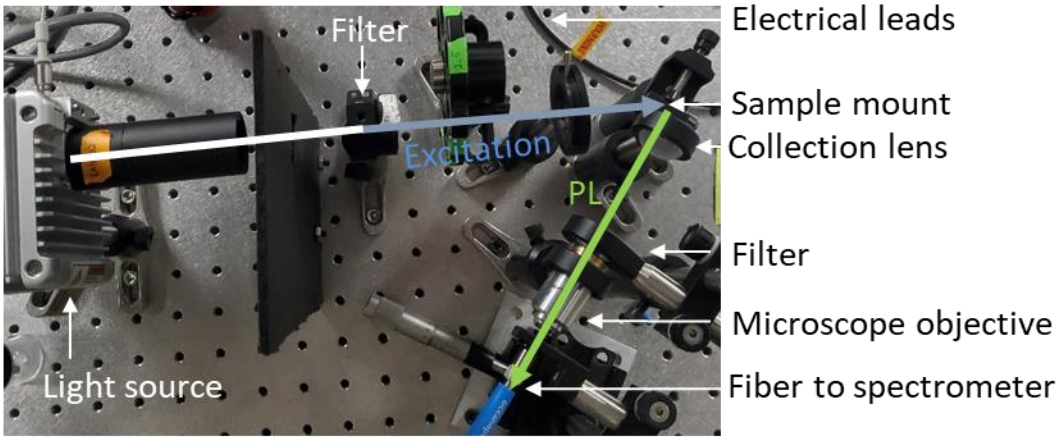

Figure 5.2 Biased-photoluminescence measurement setup. A broadband laser-driven light source (LDLS) provides illumination that is filtered to select 370 nm light and focused on a sample. The sample is connected to an electrical source meter by a pair of electrical leads. Sample PL under bias is filtered, focused with a microscope objective, and recorded through a fiber optic cable by a thermoelectric-cooled charge-coupled device (CCD) equipped with a visible-light diffraction grating.

5.3. Bilayer emission in forward bias

5.3.1. Preliminary identification of shifts

To establish the impact of applied bias on exciplex photoluminescence in non-injection-type devices, spectra were collected for a sample with the architecture: ITO/130 nm LiF/20 nm 3TPYMB/10 nm *m*-MTDATA/70 nm LiF/Al under one cycle of 0, 10, and 0 V conditions, Figure 5.3 (a). The sample emission can be divided into two emission bands, with local *m*-MTDATA emission between ~2.5-3.1 eV (400-500 nm) and exciplex emission below 2.5 eV (> 500 nm) as identified by comparison with emission spectra of pure *m*-MTDATA and an even mixture of *m*-MTDATA:3TPYMB (provided in Figure C.1). The observed reversible blue-shift of the exciplex occurs in the direction that is predicted for the Stark effect of an exciplex with a dipole moment aligned anti-parallel to the applied electric field, i.e. $\Delta E = |\vec{\mu}|\left|\vec{F}\right| \geq 0$. Further, the bulk *m*-MTDATA PL does not exhibit an energy shift with applied bias, as expected for a localized, Frenkel exciton. The energy of the exciplex is extracted via Gaussian deconvolution of PL spectra as a function

of energy (full detail and example fits are provided in Appendix C.4). The exciplex energy for each spectrum is depicted as a dashed line in Figure 5.3 (a), indicating a 55 meV shift. Assuming this is caused by the Stark effect, such a shift over a 10 V range for a total layer thickness of 230 nm suggests an initial assignment of a dipole moment of ~1.2-1.3 e·nm, which is on the order of an electron-hole pair spanning adjacent molecules.

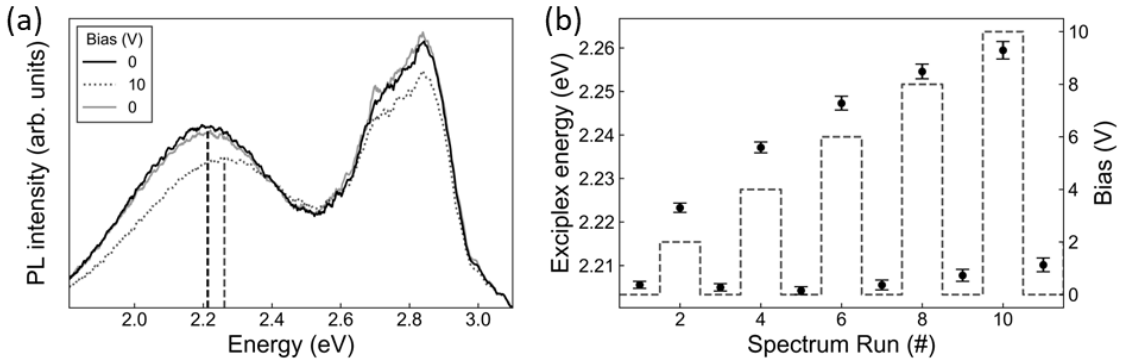

Figure 5.3 (a) Photoluminescence (PL) spectra of a device under forward-bias cycled between 0 and 10 V. Dashed lines show exciplex center energy. (b) Exciplex energies (symbols) extracted from biased photoluminescence under step-ramp bias testing (dashed line).

In order to more thoroughly explore the dependance of exciplex energy on applied field, devices were subjected to increasing applied voltage, with a return to zero bias before each increase, (i.e. 0, 2, 0, 4, … V). This pulse train was designed to investigate whether there was an appreciable shift in the zero-bias emission energy, perhaps reflecting degradation or polaron accumulation, Figure 5.3 (b). At middling biases ($0 < V < 10$ V), shifts intermediate to those at zero-bias (0 V) and high-bias (10 V) are observed suggesting the shift is indeed dependent on applied field strength. Interspersed zero-bias scans indicate the emergence of a slight testing-induced shift (~5 meV), which may reflect a low-level of polarons accumulating within the sample, leading to a retained field upon removal of bias. Importantly, current-voltage and luminance-voltage characteristics revealed no measurable electroluminescence and current densities below 10^{-2} mA/cm^2. Thus, minimal charge

injection occurs supporting the designation as a non-injection-type device and allowing electrostatic modeling to be applied considering the electric field distribution. Further, the relationship between energy and bias in Figure 5.3 (b) is plausibly linear, but more accurate identification of this dependance and assignment of an exciplex dipole moment can be made by tuning field via more than one method, i.e. bias and layer thicknesses, over a wider range of applied electric fields, and for several samples of each architecture.

Additionally, spectra were recorded at several illumination power densities to identify any relevant fluence dependent effects on the shift behavior, such as charge carrier screening or exciton-exciton repulsion [173]. Biased-PL spectra were collected from devices of architecture ITO/ 200 nm LiF/ 20 nm 3TPYMB/ 10 nm m-MTDATA/ 80 nm LiF/ Al at illumination power densities between 0.5-5 W/m^2 under 0, 2, and 10 V biases, as shown in Figure 5.4. The observed spectra show that under zero-bias, low-bias, and high-bias the spectra do not significantly vary with illumination power over a decade of intensity. Extracted exciplex energies do not vary more that ~10 meV, within fitting sensitivity, between fluences for any of the bias conditions. Slight variations are seen in

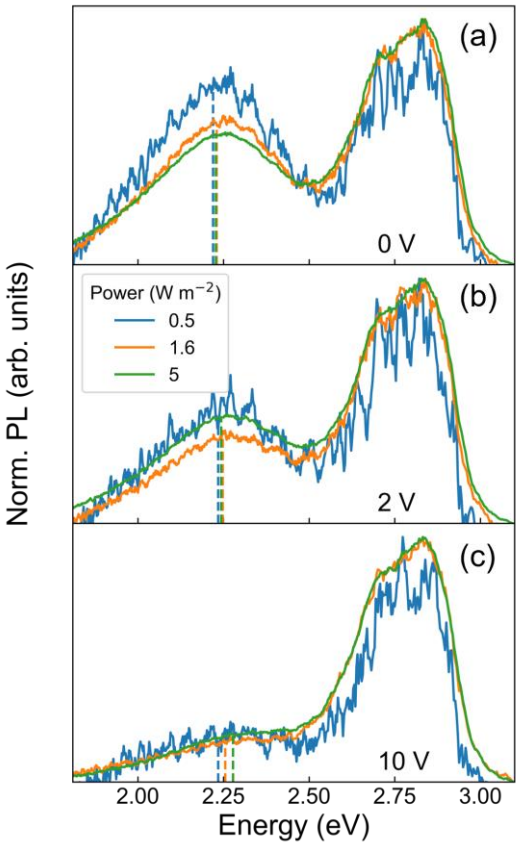

Figure 5.4 Normalized PL spectra recorded at several illumination powers under bias. Spectra measured under forward bias of **(a)** 0 V, **(b)** 2 V, and **(c)** 10 V. Dashed lines show exciplex center energy.

the relative intensity of the exciplex emission to that of local emission, but this is attributed to errors in normalization due to low-illumination intensity noise and device pixel-to-pixel variation. This result is expected as ~1 in 10^6 donor molecule sites is expected to be occupied at steady-state (details of the site occupation calculation are provided in Section C.5). Such low carrier and exciton densities predict negligible interaction between electrons and holes not comprising the same exciplex state. As such, observations of shifts are understood as the direct effect of field on isolated exciplexes, although heterogeneity of energy between individual exciplex states is likely present and will be discussed further in Section 5.3.3.

5.3.2. Quantitative shift evaluation via field-tuning

To further establish the role of field, rather than bias on exciplex emission spectra, field can be tuned by varying the thickness of material layers in non-injection-type devices. To this end, bias-dependent spectra were recorded as a function of the top insulating layer thickness in devices with architecture: ITO/40 nm LiF/20 nm 3TPYMB/5 nm *m*-MTDATA/ X nm LiF/Al, where X = 20, 55, or 90 nm LiF. Normalized PL spectra under applied biases between 0 and 10 V, in 2 V steps, of representative samples are shown in Figure 5.5 (a)-(c). Layer thicknesses were selected to apply a range of fields spanning approximately an order of magnitude allowing sensitive energy shift and dipole moment extraction. Again, dashed lines represent center energies extracted by Gaussian deconvolution

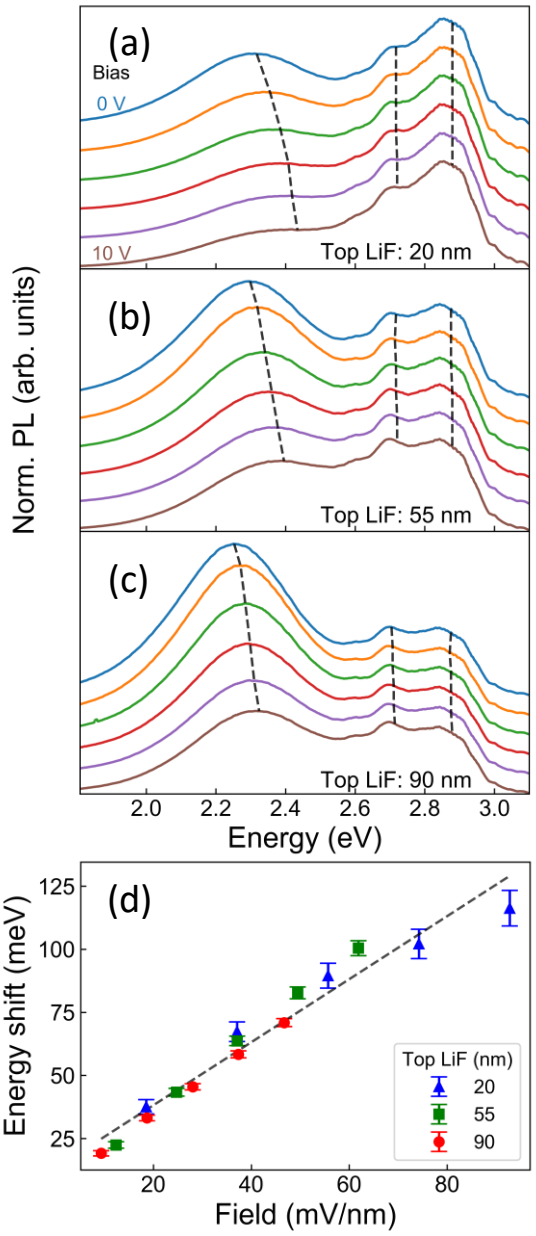

Figure 5.5 (a)-(c) Cascade plots of normalized PL spectra of devices under forward-bias between 0 and 10 V in 2 V steps. Architectures have top insulating LiF layer thickness of (a) 20 nm, (b) 55 nm, (c) 90 nm. Dashed lines denote peak energies. Spectra are normalized to local emission intensity (2.8 eV). (d) Exciplex energy shifts (vs. zero-bias spectrum) plotted vs. interfacial electric field. Dashed line shows a linear fit with slope: $1.25 \pm 0.07\ e \cdot nm$.

with the field-sensitive, lowest energy feature assigned as the exciplex. Measurements from each thickness exhibit steadily increasing exciplex emission energies under sequentially higher bias. Meanwhile, thicker devices show more closely spaced energies with bias, arising from a shallower scaling with voltage. Figure 5.5 (d) compares the exciplex energy shifts, averaged over several devices of the same architecture, with applied fields, found by applying Equation 5.1. The zero-bias energy for each device is used as the zero-shift reference energy, i.e. $\Delta E = E(V) - E(0)$ while $\epsilon_{D/A} = 2.9$ and $\epsilon_{Ins} = 1.8$, as extracted via spectroscopic ellipsometry in the near-IR, which has been previously shown to be a sufficient proxy of the static dielectric constant in organic small-molecule semiconductors [174]. Importantly, a single linear relationship, independent of sample thickness, is adequate to describe the effect of applied field on exciplex energy, with a GSE slope of (1.25 ± 0.07) e·nm, which is understood to be the exciplex dipole moment. The scale of the exciplex dipole moment far exceeds the dipole moments of organic Frenkel-type excitons [165,166] and interlayer TMDC excitons [161,163], due to the intramolecular delocalization of the component electrons and holes. Thus, a large field-linear, reversible excitonic energy shift is assigned as the giant Stark effect.

5.3.3. Alternate sources of shifts

In identifying the origin of the observed blue-shift as the giant Stark effect, we note that this is not the only field or quenching-induced emissive shift that could be observed in this system. One notable limitation of our treatment of the exciplex as a single state that shifts uniformly is that exciplex PL exhibits inhomogeneous broadening, caused by disorder in the relative orientation of the component donor, acceptor, and surrounding molecules [80,175]. Thus, there is an energetic distribution of exciplexes, commonly

described by a density of states, rather than a single unique exciplex state emitting PL. It follows that independent of the Stark effect, emissive shifts could reflect a change in filling or sampling of this exciplex energy density of states via a field or quenching effect that depends on state energy.

The exciplex density of states arises from two sources: I) the respective densities of state associated with the donor HOMO and acceptor LUMO arising from variations in the local dielectric environment and II) the exciplex binding energy depending on relative arrangements of the charged donor and acceptor molecules via the electron-hole separation. Source I, subject to spatially random variations, would not predict a sensitivity of exciplex energy to applied field, since carriers will favor shallower HOMO and deeper LUMO energy states, regardless of field. Source II, via the electron-hole separation and exciplex binding energy, could depend on field in two ways, either by changing the electron-hole separation or by energy-dependent quenching via carrier dissociation. Al Attar et al. considered a model where the electron-hole separation is compressed via the applied field which favors carrier pinning to the donor-acceptor interface [104]. Reduction of the electron-hole separation should increase binding energy, leading to a red-shift in emission energy. Additionally, exciplexes with larger electron-hole separations and hence smaller binding energy are more easily dissociated, thus quenching of these high energy exciplexes would also lead to a red-shift in emission [51,149]. Taken together, these consideration of the exciplex density of states would predict a field-dependent red shift in energy, although with unclear magnitude and scaling with applied field. It is possible that these effects arising from the exciplex density of states are also present here but occur in much smaller

magnitude than the field-linear Stark effect component. Indeed, these effects may be partially responsible for the sub-linear deviation of shift versus field above ~70 mV/nm.

5.4. Bilayer emission in reverse bias

To further solidify the interpretation of luminescence blue-shifts observed under forward-bias measurements as the GSE, we also examined the behavior of biased-PL under reverse bias for devices with a structure of ITO/ 115 nm LiF/ 20 nm 3TPYMB/ 10 nm *m*-MTDATA/ 55 nm LiF/Al. Bias was again applied between the top Al contact and the ITO contact, but under 0, -10, and 0 V biases, measured in sequence with ~0.9s between scans, as shown in Figure 5.6 (a). The exciplex emission shifts by a small amount (~10 meV) when -10 V is applied with a slight decrease in intensity of exciplex emission relative to local *m*-MTDATA emission. Upon removing the bias, returning to 0 V, the exciplex intensity falls significantly and shifts blue by ~140 meV. Although the exciplex feature lacks a clear peak, there is a distinct excess emission feature above that of neat m-MTDATA which can be unambiguously extracted via the Gaussian deconvolution method discussed above. Even the weakest exciplex emission features matched or exceeded the intensity of local emission tail, thus comprising ≥ 50% of the total spectrum intensity near the extracted exciplex center energy. Additionally, subsequent zero-bias spectra were collected over the following ~20 s and are shown in Figure C.3 (a). The extracted exciplex energy is plotted against time since application of the -10 V pulse in Figure 5.6 (b), while the relative exciplex intensity is shown in Figure C.3 (b). Both the energy and intensity of the exciplex emission return toward their initial, zero-bias, values and then plateau. The relaxation of the energy shift is well fit by an exponential decay with a time constant of 2.2 s, with only ~20 meV of the maximum >140 meV shift retained, while the relative exciplex

intensity recovers with a time constant of 4.9 s to approximately half the pre-bias intensity. The recovery of energy and intensity on timescales different by a factor of >2 suggests that these factors may vary independently and that luminescence quenching is not the origin of the observed shifts. This transient behavior is in sharp contrast to the corresponding behavior under a forward bias (+10 V) pulse, as shown in Figure 5.6 (c), which shows a blue-shift that is immediately eliminated upon return to zero-bias, with exciplex energy tracked against time in Figure 5.6 (d) (subsequent spectra reported in Figure C.4.

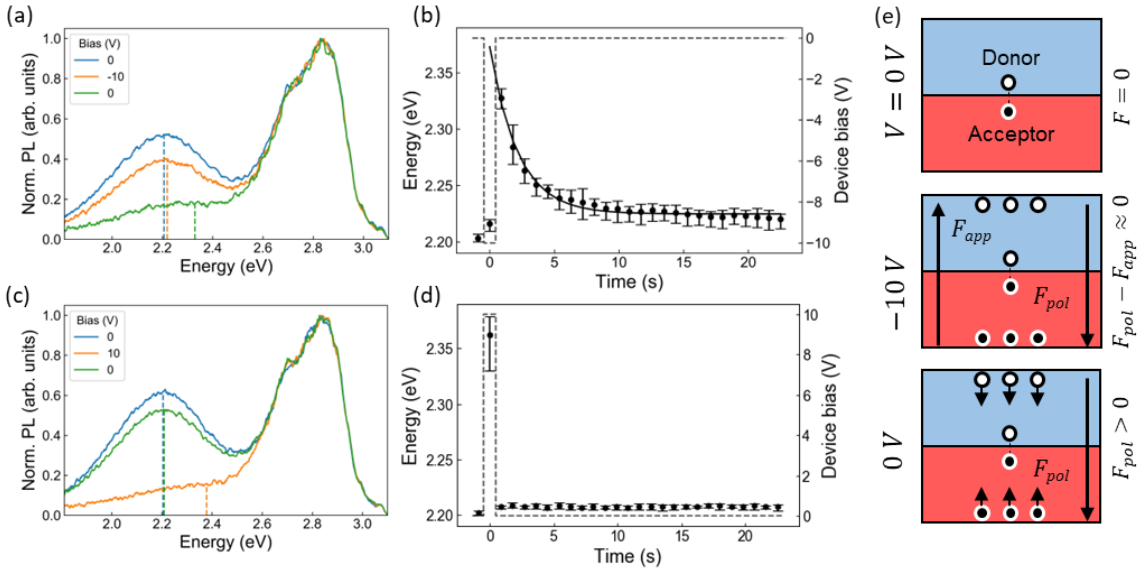

Figure 5.6 (a) Normalized biased PL spectra measured before, during, and after a -10 V bias pulse (reverse-bias). (b) Extracted exciplex emission energy as a function of time after a -10 V bias pulse at t=0. (c) Normalized biased PL spectra at before, during, and after 10 V bias pulse (forward-bias). (d) Normalized biased PL spectra at zero-bias measured as a function of time after 10 V pulse. (e) Schematic of field and carrier concentrations in the D-A bilayer during the 0, -10, 0 V pulse sequence and subsequent relaxation.

In considering the contrasting behavior observed in exciplex PL between forward and reverse bias, it is important to note that the electric field generated in the former confines photogenerated carriers to the donor-acceptor interface, while in the latter it favors exciplex dissociation. Under reverse bias, exciplexes at the D-A interface may act as a reservoir for free charges via field-assisted dissociation. Free holes can then migrate and accumulate at the donor-top LiF interface while electrons accumulate at the acceptor-bottom LiF

interface, since the insulator layers frustrate carrier extraction, as depicted in Figure 5.6 (e). Accumulation stops when the field from the resultant sheet charge counteracts the applied field in the organic active layers, leaving no net field, ceasing dissociation. In addition, under this condition of complete screening, no field is present at the D-A interface and exciplexes experience no Stark shift, consistent with the limited shift observed in Figure 5.6 (a) for a -10 V reverse bias. The carrier densities required at the organic-LiF interfaces to fully screen the applied field is ~10^{16} m^{-2} which can be readily supplied by dissociating only 1% of the exciplexes formed at a rate of ~10^{18} $m^{-2}s^{-1}$ over the ~1 s measurement time (see Appendix C.5). While removal of the reverse bias will immediately impact the field at the D-A interface, accumulated carriers remain, leaving an electric field of equal magnitude, but opposite direction as the original applied field, mimicking a forward-bias field and inducing a blue-shift via the Stark effect. In fact, by extrapolating the decay in exciplex energy post-reverse-bias back to t=0, as in Figure 5.6 (b), we can closely reproduce the energy observed at 10 V in Figure 5.6 (d) of ~2.36 eV. The relative intensity of exciplex PL post-reverse-bias is also remarkably similar to that of forward-bias condition in Figure 5.6 (d), further reflecting that the net fields in each condition are comparable. This manifestation of the giant Stark effect is a transient effect as carriers are attracted to the D-A interface and recombine, causing the shift to decay back to the zero-field energy, as observed in Thus, we summarize the observed behavior under reverse bias as the combination of screening at reverse bias followed by a decaying blue-shift due to recombination. This provides another means of observing a Stark shift for exciplexes via a field generated by dissociated carriers as opposed to an applied polarization field. Further, the contrasting sources of electric field in post-reverse-bias and forward-bias

measurements underscores the dominant role of the applied field in determining the blue-shift in exciplex PL energy.

5.5. Dilute bilayer emission behavior

Prior work on emissive exciplex-forming donor-acceptor mixtures has shown a sensitivity of several photophysical properties, such as PL quantum yield and emission energy to dilution in a wide-energy material [103,167]. A related dilution-induced impact on the exciplex dipole moment may be present and could be observed via a change in the GSE slope using the methods described here. Additionally, the Giant Stark effect could be applied to probe and track changes in the electron-hole separation of exciplexes, which is often understood indirectly via estimations from the binding energy [79,104,174]. To probe the role of dilution on the dipole moment, an additional wide-energy gap organic semiconductor, 1,1-bis[(di-4-tolylamino)phenyl]cyclohexane (TAPC), Figure 5.7 (a), was added with varying volume percent(s) to the acceptor and/or donor layers in the layer structure: ITO/80 nm LiF/20 nm 3TPYMB:TAPC/10 nm *m*-MTDATA:TAPC/40 nm LiF/Al, as depicted in Figure 5.7 (b). TAPC possesses a LUMO similar to *m*-MTDATA, while its HOMO is between those of *m*-MTDATA and 3TPYMB, maintaining formation of the *m*-MTDATA:3TPYMB exciplex as the lowest-energy state [80,85].

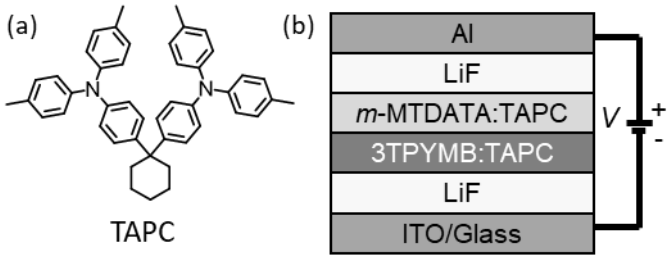

Figure 5.7 (a) Molecular structure for wide-gap semiconductor TAPC. (b) Layer architecture for dilute-bilayer devices.

Biased PL spectra were recorded between 0 and 10 V in 2 V steps for each dilution, with the spectra shown in Figure 5.8. Exciplex center energies are extracted using the same methodology as earlier described and energies for each bias condition can be found in Figure C.5. The spectra of Figure 5.8 show a blue-shift in energy with increasing applied bias, but with visibly different scaling of energy vs. field, suggesting a range of dipole moments for different dilution conditions. The extracted dipole moments for each dilute bilayer are shown in Table 5.1. While no reduction in dipole moment is observed when diluting the *m*-MTDATA donor with 20 vol.% TAPC, a large reduction in the dipole moment to 0.99 e·nm is found with dilution of the 3TPYMB acceptor with 20 vol.% TAPC. Further diluting to 50 vol.% TAPC in the donor and/or acceptor layers reduces the dipole moment to ~0.83-0.92 e·nm in all cases. This dependance suggests that sufficient inclusion of a wide-energy gap dilutant in at least one of the layers reduces the dipole moment.

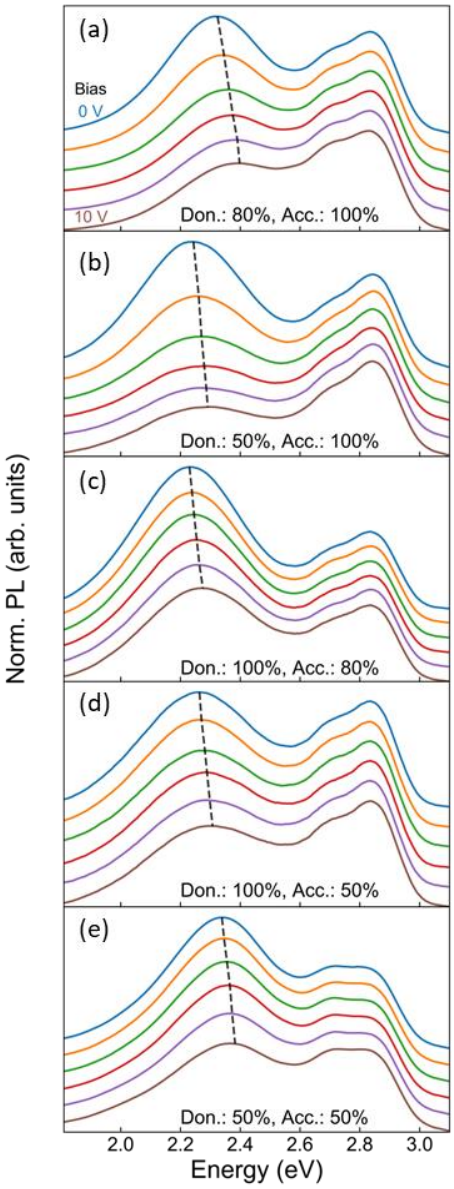

Figure 5.8 Cascade plots of normalized emission spectra for dilute donor-acceptor bilayer devices under biases between 0 and 10 V in 2 V steps, with donor and acceptor content noted by volume percent. Dashed lines denote exciplex energies. Spectra are normalized to local emission intensity (2.8 eV).

Table 5.1 Summary of extracted exciplex dipole moments for donor-acceptor bilayers diluted on one or both sides with wide-gap TAPC. Donor and acceptor concentrations are given as volume percentages, with the remainder constituted by dilutant TAPC.

Donor (vol %)	Acceptor (vol %)	Dipole moment (e·nm)
0	100	1.32 ± 0.08
50	100	0.83 ± 0.05
50	50	0.92 ± 0.05
100	50	0.91 ± 0.05
100	80	0.99 ± 0.05

This dilution effect on dipole moment could arise from more than one mechanism as dilution may impact, for example, the relative orientation of donor or acceptor molecules at the donor-acceptor interface, as has been reported in organic host-guest systems [176]. Face-on donor and acceptor molecules would be more closely packed than two edge-on or randomly oriented molecules, leading to a smaller electron-hole separation and a reduction in the dipole moment. Donor *m*-MTDATA has been reported to exhibit slight preference for horizontal alignment, which may be impacted by dilution in a host material, impacting electron-hole separation [177]. Alternately, if the component electrons and holes are delocalized beyond nearest neighbor molecules at the D-A interface, then disruption of donor-donor or acceptor-acceptor interactions may pin the component carriers at the interface. Similar observations have been reported for interfacial excitons in a blend whereby the electron-hole separation is reduced as the acceptor fraction is reduced below 0.5 due to carrier confinement in the acceptor domains [174]. Regardless of mechanism, further work is required to detail the morphological impact of dilution in the donor and

acceptor phases, however the observation of the giant Stark effect for exciplex PL offers a direct means to quantify changes in the exciplex dipole moment with dilution.

5.6. Summary and conclusion

In conclusion, we demonstrate the giant Stark effect for luminescent exciplexes formed at organic donor-acceptor planar heterojunctions, with a reversible, field-linear energy shift in photoluminescence on the scale of 10's-100's of meV observed under forward-bias. This steep relationship between energy and field arises due to the large electron-hole separation of charge carriers in the exciplex which is delocalized across the donor-acceptor interface, enhanced by careful anti-alignment of the excited state dipole moment with respect to the applied electric field. Under reverse-bias, a transient blue-shift arising from the giant Stark effect reflects screening and recombination of photogenerated charges. The giant Stark effect is further applied to probe a tuning in the exciplex dipole moment realized through the dilution of the donor and acceptor materials. Observation of the giant Stark effect offers a new means to probe interfacial excited starts at organic interfaces, while solid-state dilution offers a means to tune excited state energies. Additionally, a clearer description of the dipolar nature of organic exciplexes can be employed for further study of interfacial excited state energetics and dynamics for organic photovoltaic and light-emitting device applications.

6. Exciplex energy sensitivity to binary dilution

6.1. Background

Reiterating earlier discussion, excitonic device performance can be determined by as small as 5-10 meV differences in state energies, making even subtle variation in exciton energies critical to their performance [165,166]. Various methods have been identified to tune the energy of molecular excited states via material selection or functional group substitution [178,179], or for a given organic semiconductor by solid-state solvation in a polar or nonpolar medium [111,112]. Additional methods for tuning exciplex emission energies have been identified including dilution in a host, compression of thin films, and the earlier mentioned electric-field tuning via Stark effect [103,130,167]. Methods using pressure or electric field require continuous application of a large external stimulus, complicating application to existing devices. Dilution in a wide-gap host offers a method to tune exciplex energy with existing processing of codeposition with a tertiary component, rather than redesigning the sample architecture, for example to induce residual strain [103,167]. However, including an optically inactive host material in OPV active layers would limit absorption and reduce efficiency. In an OLED emissive layer, the host could limit charge transport and lead to higher carrier concentrations leading to quenching. An alternative paradigm for tuning the energy of an exciplex formed by a donor acceptor pair could be by varying the ratio of donor and acceptor. In fact, many exciplex-based OLEDs have unequal donor:acceptor compositions to optimize charge transport and the resulting efficiency, often between 25-75 vol. % donor [180,181]. However, systematic study of the effect of D:A ratio in binary mixtures has not been reported.

Additionally, preliminary data from earlier measurements of unequal D:A mixtures in the work discussed in Chapter 4 suggested that some D-A mixtures indeed exhibit a significant change in emission energy and underlying exciton energy when excess donor or acceptor is present. In that work, photoluminescence of three acceptors, 3TYPMB, BCP, and BPhen paired with a single donor, m-MTDATA, was measured for various doping concentrations of donor from 10-90%. Molecular structures for these materials can be found in Figure 2.5. While minimal variations in peak exciplex energy were observed for BCP- and BPhen-containing systems, m-MTDATA:3TPYMB showed energies spanning more than 50 meV across compositions. Additionally, OLED architectures are increasingly employing more complicated TADF emission architectures. Emissive layers containing molecular TADF emitters that also form exciplexes with a host material, ternary mixtures containing exciplex forming cohosts and an emitter molecule, and hyperfluorescent OLEDs complicate device analysis requiring deeper understanding of the photophysical properties of simpler exciplex-forming mixtures [36,101,182]. In this chapter, measurements of binary D:A mixtures with varying compositions were investigated via photoluminescence spectroscopy to identify the scale of such shifts for a pair of D:A systems. Compositions will be primarily noted using D:A ratio $R_{D:A}$, but this can be converted to donor fraction by volume, f_d, (or donor percent) via the following equation:

$$f_d = \left(1 - \frac{1}{1+R_{D:A}}\right)(100\%) \quad (6.1)$$

6.2. Experimental methods

Thin film mixtures of donor and acceptor materials were prepared by vacuum thermal co-evaporation from two sources of purified organic powders, similar to methods in previous chapters. Deposition rates were monitored using separate QCMs to achieve a

desired doping concentration or donor:acceptor ratio. Photoluminescence spectra were recorded by exciting samples at 350 nm by filtering emission from a Xe arc lamp. Sample preparation and emission spectra were recorded by Colton Gerber under the direction of the author. For more detail on sample preparation and thin film photoluminescence measurements, please refer to Section 4.2.

6.3. Results and discussion

6.3.1. m-MTDATA:3TPYMB binary dilution

To clarify the role of binary dilution on exciplex energy, a more detailed study of m-MTDATA:3TPYMB energy versus doping was carried out. Mixtures of m-MTDATA:3TPYMB in doping ratios of between 16:1 and 1:16 were illuminated at 370 nm and their emission spectra were recorded. Example photoluminescence spectra for each mixture is shown in Figure 6.1 as a function of energy.

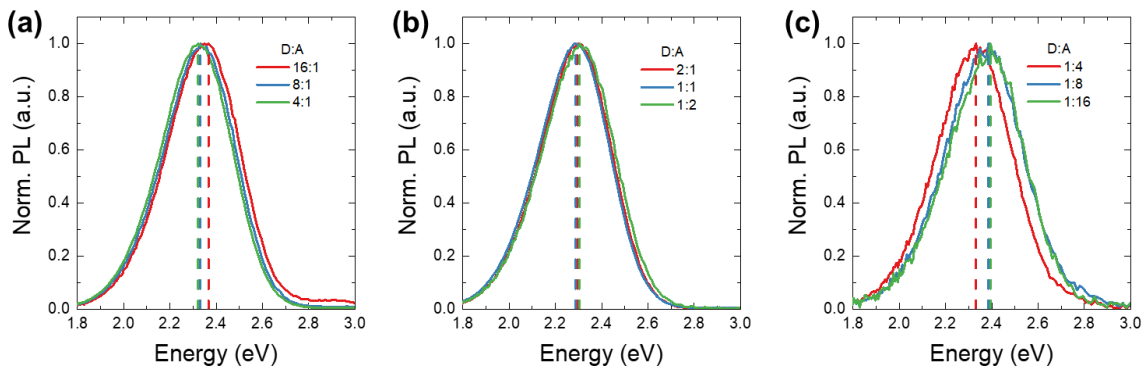

Figure 6.1 m-MTDATA:3TPYMB emission spectra as a function of donor:acceptor (D:A) ratio. (a) Donor-rich mixtures with donor:acceptor ratios of 16:1, 8:1, and 4:1. (b) Near-equal mixtures with donor:acceptor ratios of 2:1, 1:1, and 1:2. (c) Acceptor-rich mixtures with donor:acceptor ratios of 1:4, 1:8, and 1:16. The peak energy of each spectrum is indicated by a dashed line.

For donor-rich m-MTDATA:3TPYMB mixtures, shown in Figure 6.1 (a), the peak energy increases with increasing donor content from ~2.33 eV for 4:1 D:A to ~2.36 eV for 16:1 D:A. Near-equal mixtures of donor and acceptor, shown in Figure 6.1 (b), have peak

emission energies of ~2.29-2.31 eV, with 1:1 D:A as the lowest energy. Acceptor-rich mixtures, Figure 6.1 (c), exhibit increasing peak exciplex energy with increasing acceptor content rising from ~2.33 eV for 1:4 D:A to ~2.39 eV for 1:16 D:A. Error bars are determined by taking the larger of the range of extracted peak energies for a given mixture composition or the instrument resolution (± 2 nm) at the relevant measurement energy to reflect uncertainty of sample-to-sample and measurement uncertainty. Shifts were observed to be reproducible across several samples. In addition to the peak energy for each mixture, the full width at half maximum (FWHM), characterizing the breadth of the emission feature, of each emission spectra was extracted for each mixture composition. Peak energies and FWHMs of each sample composition are shown as a function of D:A ratio in Figure 6.2.

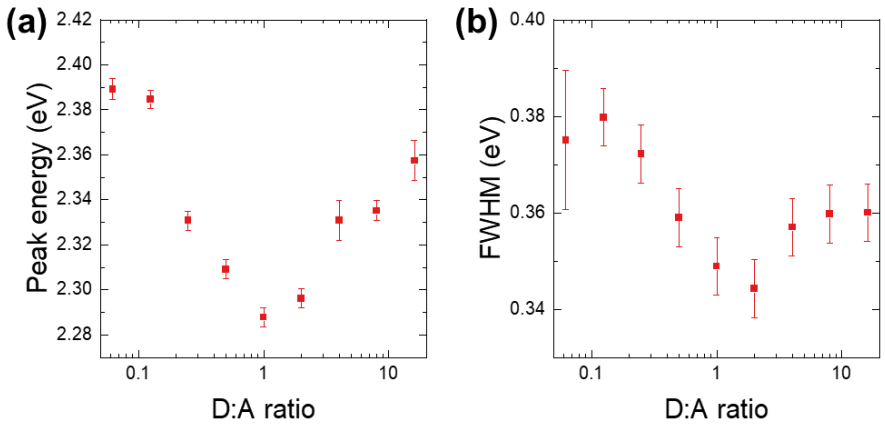

Figure 6.2 m-MTDATA:3TPYMB photoluminescence spectrum properties for mixture of various D:A ratios. (a) Peak emission energy (b) Full width at half maximum (FWHM).

Reflecting the same trends seen in Figure 1, the extracted peak energies noted in Figure 6.2 exhibit increasing energy as the composition becomes more unequal. With highly unequal donor:acceptor compositions, the energy increases from ~2.29 eV to as high as 2.39 eV for 1:8 or 1:16 D:A mixtures. This represents a 100 meV shift in exciplex energy without changing the molecular structure of either the donor or acceptor component or

introducing any new dopant. Such a profound modulation in exciplex energy without introduction of a new or different constituent or thermal treatment has not been previously identified.

In addition to the shift in peak energy of the exciplex, the FWHM of the m-MTDATA:3TPYMB exciplex varies between ~0.34-0.38 eV, with lower energies near 1:1 or 2:1 D:A and highest for acceptor-rich mixtures between 1:4 and 1:16 D:A. Since the broadening is only ~30-40 meV between the equal or near-equal donor:acceptor mixtures, a clear dependance on composition cannot be extracted, but a sensitivity to composition can still be identified.

6.3.2. mCP:PO-T2T binary dilution

As noted earlier, the exciplex emission energy of m-MTDATA:BCP and m-MTDATA:BPhen exhibited minimal changes in energy across composition between ~10-90% donor (D:A ratios 1:9-9:1), so questions remain about the generality and origin of the binary dilution induced shifts for m-MTDATA:3TPYMB. To further investigate the generality of the observed shift behavior the exciplex formed in 1,3-Bis(N-carbazolyl)benzene (mCP): 2,4,6-tris[3-(diphenylphosphinyl)phenyl]-1,3,5-triazine (PO-T2T) was considered, whose molecular structures can be found in Figure 2.5. This exciplex pairing is of particular interest for OLEDs employing TADF cohosts as it provides efficient blue emission (472 nm or 2.63 eV). It has been commonly used as a sky blue emitter in tandem, all-exciplex white OLEDs, including the first demonstration of such a device [32,183]. This exciplex has also been shown to form an excellent host for blue phosphorescent OLED emission with a device reported with 30.3% EQE and low driving voltage, resulting from efficient energy transfer from the exciplex to phosphor with

minimal energy loss [127]. With these device applications of mCP:PO-T2T, it is clear this system is an appropriate model system for observation of exciplex properties.

Emission spectra for neat mCP and a 1:1 D:A mixture of mCP:PO-T2T are shown in Figure 6.3, excited at 300 nm (4.13 eV) and 350 nm (3.54 eV), respectively. Emission spectra of neat PO-T2T show negligible emission when excited between 300-350 nm, likely reflecting very low PL efficiency. PO-T2T emission has been reported in the solution phase to possess peak emission ~400 nm (3.10 eV) [127]. As seen in Figure 6.3, mCP exhibits highly structured emission with several distinct peaks with energies between ~2.9-3.5 eV. When mixed with the acceptor PO-T2T, the emission spectrum shifts to much lower energy, with peak energy of ~2.63 eV, and loses vibronic structure, consistent with previous reports [32,127].

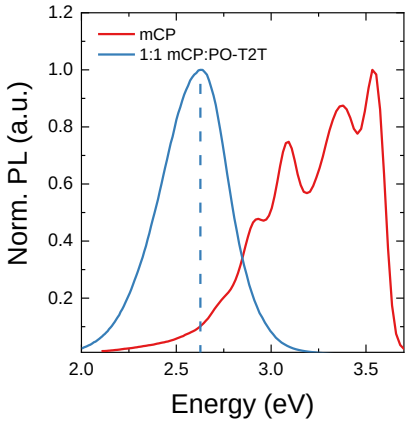

Figure 6.3 Normalized photoluminescence spectra of neat mCP and 1:1 mCP:PO-T2T. The peak energy of the mCP:PO-T2T exciplex formed in a mixture of 1:1 D:A is indicated with a dashed line.

Similar to earlier measurements, mCP:PO-T2T mixtures with doping ratios of between 1:16 and 8:1 were illuminated at 350 nm and their emission spectra were recorded. Samples with a 16:1 D:A ratio showed notable local emission due to minimal acceptor content restricting quenching of donor excitons, which is not adequately treated in this analysis.

Example photoluminescence spectra for each mixture is shown in Figure 6.4 as a function of energy.

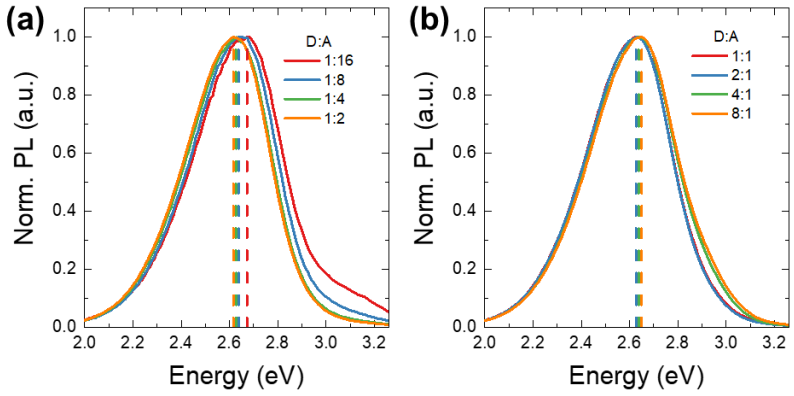

Figure 6.4 mCP:PO-T2T emission spectra as a function of donor:acceptor (D:A) ratio. (a) Acceptor-rich mixtures with donor:acceptor ratios of 1:16, 1:8, 1:4, and 1:2. (b) Equal and donor-rich mixtures with donor:acceptor ratios of 1:1, 2:1, 4:1, and 8:1. The peak energy of each spectrum is indicated by a dashed line.

Acceptor-rich samples of mCP:PO-T2T mixtures, shown in Figure 6.4 (a) exhibit peak energies rising with increasing acceptor content from ~2.62 eV for 1:2 D:A to ~2.66 eV for 1:16 for highly acceptor rich mixtures with D:A ratios of 1:16 and 1:8, emission is also observed between 3.0-3.2 eV, likely arising from acceptor PO-T2T excitons, despite minimal emission in neat films of PO-T2T. It is hypothesized that acceptor emission is enhanced with slight doping of donor mCP by host-induced suppression of non-radiative recombination, despite strong charge-transfer quenching [118,127]. Equal and donor-rich mixture emission spectra are shown in Figure 6.4 (b) and have peak emission energies of ~2.62-2.65 eV, with negligible donor emission above 3 eV. Although only small shifts are observed in mCP:PO-T2T across composition, shifts of this scale were observed to be reproducible.

Peak energies and FWHMs of each sample composition are shown as a function of D:A ratio in Figure 6.5. Notably, the observed exciplex energy only varies by ~40 meV across

composition, much smaller than those observed for m-MTDATA:3TPYMB mixtures across compositions. Despite such small changes in energy, lower exciplex energies are observed in equal or near equal mixtures of mCP:PO-T2T with D:A ratios between 1:4 and 2:1. Higher exciplex energies are observed for highly unequal mixtures, with acceptor-rich D:A ratios of 1:16 and 1:8, or donor-rich samples with D:A ratios of 4:1 and 8:1, similar to observations for the exciplex of m-MTDATA:3TPYMB. Similar to the broadening accompanying shifts observed earlier, the emission spectrum of mCP:PO-T2T also broadens from ~0.40 eV to ~0.42 eV between equal or near equal mixtures and highly donor or acceptor rich samples, such as 1:16 or 8:1 D:A mixtures. However, the broadening is only ~20 meV, smaller than for m-MTDATA:3TPYMB mixtures.

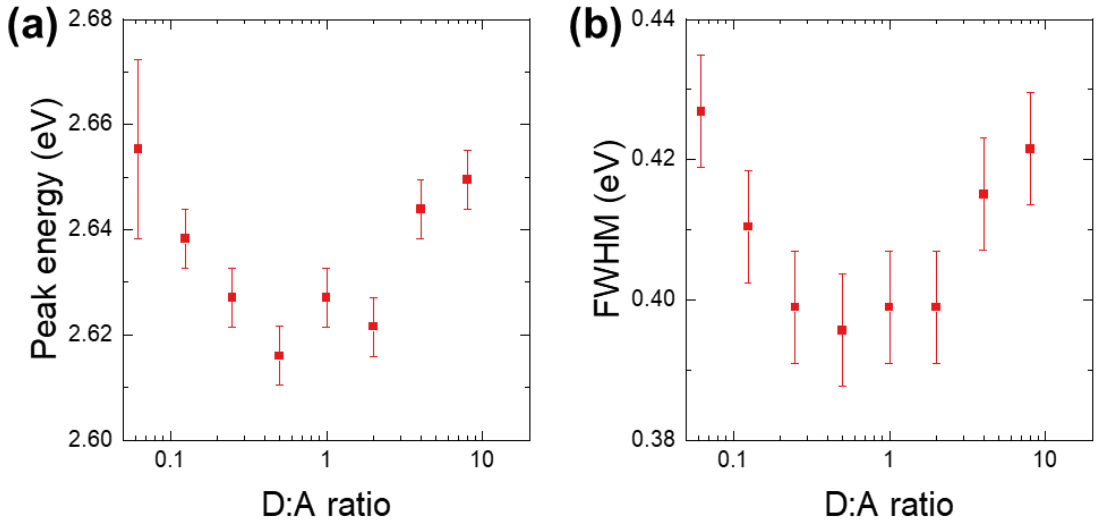

Figure 6.5 mCP:PO-T2T photoluminescence spectrum properties for mixture of various D:A ratios. (a) Peak emission energy (b) Full width at half maximum (FWHM).

6.3.3. Potential origins of energy variation

Further work would be required to specify the mechanism and provide a framework to predict the prevalence and scale of composition-dependent exciplex energy shifts across

materials, however several mechanisms seem plausible immediately, while others can likely be disregarded after brief consideration.

First, from the work of Chapter 4 it has been established that the diffusion length of exciplex-forming mixtures varies across composition, warranting consideration of the role of diffusion in composition-dependent energy shifts. Perhaps diffusion allows exciplexes to migrate through the exciplex energy density of states relaxing to a lower energy during the process. In Chapter 4 it was observed that exciplex diffusion seems to be limited by the motion of the slowest component charge carrier, leading to increased energy transfer for mixtures rich in the lower mobility component. One report estimated that sampling of different donor-acceptor pairs by the exciplex of m-MTDATA:3TPYMB could lead to an observed ~40 meV red-shift between emission collected below 1 μs and beyond 30 μs [80]. Although a smaller effect than the ~100 meV shift observed here, this could prove a significant contribution. In the case of m-MTDATA:3TPYMB, acceptor 3TPYMB is limiting and the largest diffusion length of ~7 nm for a 25% donor (1:3 D:A) mixture and a diffusion length below 1 nm for 90% donor (9:1 D:A). This trend was monotonic unlike the observations of exciplex energy for this pairing. If exciplex diffusion played a significant role in the observed emission energy of m-MTDATA:3TPYMB a monotonic trend of energy with composition would also be expected. It is expected that with a longer diffusion length, any red-shift due to relaxation in the exciplex energy density of states, resulting from sampling of lower energy sited for electrons and holes near the D-A interface, would increase. Regardless of whether diffusion leads to a blue- or red-shift in energy, the trend in L_D vs composition in the range of D:A compositions explored in Figure 4.6 predicts a monotonic energy trend as well. However, a minimum in energy is observed

near mixture compositions of 1:1 D:A and as such the role of diffusion in composition dependent exciplex energy shifts is rejected in the case of m-MTDATA:3TPYMB. Since diffusion length and time-dependent emission spectra data is not available for mCP:PO-T2T, this theory cannot be fully considered.

Second, molecular alignment is known to be influenced by the inclusion of a host material, impacting optical properties such as birefringence and absorption anisotropy [89]. Perhaps mixtures rich in one component orient in a manner that the resulting donor-acceptor pair comprising the exciplex is oriented in a state of higher energy, possibly with larger donor-acceptor spacing and lower binding energy. However, both m-MTDATA and 3TPYMB exhibit no or minimal spontaneous orientation of the transition dipole moment in pure thin films prepared by vacuum thermal evaporation, so such effects orientation effects would be surprising [89,177]. Additionally, the apparent shifts observed for mixtures rich in either component suggest that such orientation effect must behave similarly for donor-rich or acceptor-rich films, which is unlikely. This cannot be ignored out of hand, but such orientation effects could be corroborated or rejected with supplemental measurements of optical anisotropy to reveal any composition dependent orientation effects.

Finally, the shifts could arise from delocalization of the exciplex changing with different amounts of each material in the mixture, leading to a variation in electron-hole separation, binding energy, and thus exciton energy. In such a view, the electron is shared amongst several acceptor molecules near the D-A interface while the hole is shared amongst donor molecules. The findings of Chapter 5 suggest that exciplexes formed at planar m-MTDATA:3TPYMB interfaces possess electron-hole separations in excess of

nearest-neighbor donor and acceptor molecules. Additionally, diluting one or both sides of the bilayer showed a reduction in this separation, suggesting substituting donor or acceptor molecules can affect exciplex size. With increasing donor:acceptor ratio, more sites are available for the hole to sample allowing it to be further delocalized. Similarly, fewer acceptor sites are available leading to electron localization. If the delocalization of the carrier in the majority phase, i.e. holes in a donor-rich mixture, is of a larger scale than the localization of the minority phase carrier, a net delocalization of the exciplex will result, reducing binding energy and increasing emission energy.

Earlier work studying the effect of dilution with a wide-gap semiconductor on bilayer emission of Chapter 5.5 exhibited a reduction in electron-hole spacing predicting a red-shift in energy with dilution. However, here the dilution is with one of the active components allowing delocalization of one carrier to occur adding the possibility for a blue-shift in emission, as observed. The competition between localization of the minority component carrier and delocalization of the majority component carrier is critical to the balance of whether a net red- or blue-shift occurs. Such competition between localization and delocalization may be the cause of some D:A pairings exhibiting small or no composition dependent shifts, while m-MTDATA:3TPYMB exhibits profound shifts. A preliminary model is presented in the next section considering how delocalization could be understood in terms of the donor fraction or donor:acceptor ratio.

6.4. Dilution-dependent domain size model

To illustrate one method to consider the role of delocalization within continuous donor or acceptor domains, a one-dimensional model of a donor:acceptor mixture can be considered. For a mixture with a defined donor fraction f_d, a random sequence can be

generated with donor or acceptor sites with probability f_d for the site being a donor molecule and $f_a = 1 - f_d$ for the site being occupied by an acceptor site. One of many possible arrangements of sites for a pair for each of two donor fractions are illustrated in Figure 6.6. A characteristic domain size for donor and acceptor regions can be extracted by taking the number of sites occupied by the same type in an uninterrupted row. These donor domain and acceptor lengths are denoted as *D* and *A* respectively. One limitation of a one-dimensional domain model is that percolation of domains cannot occur, however this greatly simplifies analysis for a preliminary model.

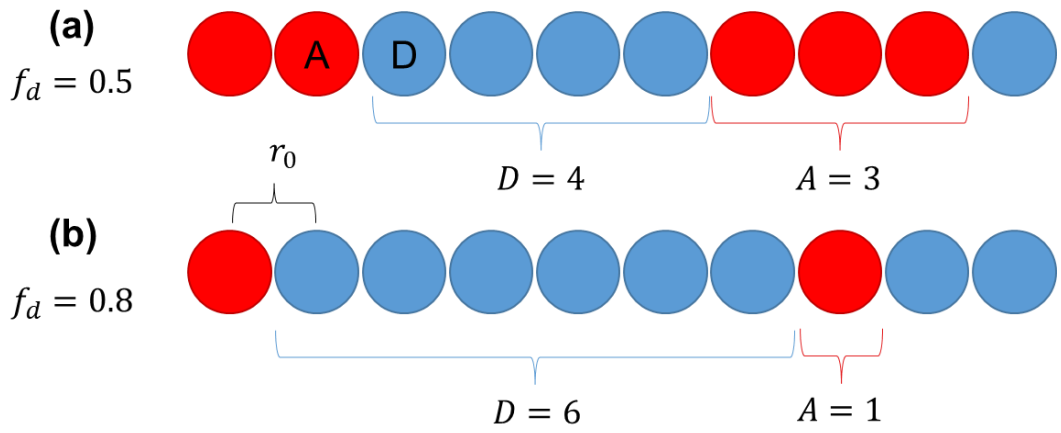

Figure 6.6 Possible one-dimensional donor-acceptor mixture arrangements with defined donor fraction f_d. (a) $f_d = 0.5$: One continuous domain of donor and acceptor sites are indicated. (b) $f_d = 0.8$: increasing donor content increases the likelihood of longer donor domains while reducing the average length of acceptor domains.

Next, an electron-hole separation can be estimated by assuming the carriers delocalize away from the D-A interface by some fraction of the domain size. Additionally, the distance between sites is assigned as r_0, which is treated as ~0.8 nm taken from the lower bound of electron-hole separations observed in Chapter 5. If a domain is larger than one site, a carrier can be spread among sites extending the electron-hole separation. The precise scaling of carrier position with domain size is critical for precise evaluation of this model,

however coarse observations can be made by assuming that the carrier spreads to an average position that is some fraction $x \in [0,1]$ of the domain size D or A, although the spreading fraction will likely be much << 0.5, since carriers is attracted to the D-A interface and will likely only delocalize over the first few sites. From this an electron-hole separation can be defined as:

$$r = r_0(1 + x * (A + D - 2)) \qquad (6.2)$$

For single donor-acceptor pairs ($A = D = 1$), the separation reduces to r_0, while only increasing by fractions of r_0 for each additionally available site. A more complex relationship $r(D, A)$ would likely require that separation does not continue indefinitely with available sites since it is expected that for example, the 50th donor site will not meaningfully contribute to carrier delocalization. However, predicted separations below fall within a few nanometers, so this issue is likely absorbed into the precise value of x selected.

Next, a method to predict the likelihood of each domain size pair, *D* or *A*, is required to predict the average, or expectation, value of the separation between electrons and hole for a given D:A mixture composition. Since exciplexes must form at the interface between a donor and acceptor domain, the donor fraction can be used to predict the likelihood that the next site is a donor using the overall donor fraction of the sample, i.e. f_d. This can then be repeated to generate a probability distribution $P_D(D)$ for the likelihood of a selected donor site at an interface belonging to a domain of size D, which is treated as a random variable with integer values, as:

$$P_D(D, f_d) = (1 - f_d) \cdot f_d^{D-1}, D \geq 1 \qquad (6.3)$$

where the likelihood of a single donor surrounded by only acceptor ($D = 1$) is $1 - f_d$, decreasing with increasing donor content. Similar consideration can be applied to the acceptor domain size using the acceptor fraction:

$$P_A(A, f_d) = f_d \cdot (1 - f_d)^{A-1}, A \geq 1 \qquad (6.4)$$

Treating donor and acceptor domain sizes as statistically independent, with their common dependance on total donor and acceptor abundance captured by f_d, the joint probability distribution $P = P_D P_A$ of donor and acceptor domain sizes may be defined. Importantly, unity total probability is preserved, i.e. $\sum_{D=1}^{\infty} \sum_{A=1}^{\infty} P_D(D) P_A(A) = 1$. Average or expectation values of the electron-hole separation may be computed using Equation 6.4 for a prescribed donor concentration.

$$\langle r \rangle = \sum_{D=1}^{\infty} \sum_{A=1}^{\infty} P(A, D, f_d) \cdot r(A, D, f_d) \qquad (6.5)$$

Average exciplex sizes are simulated as for several values of *x*, the delocalization fraction, as a function of D:A ratio in Figure 6.7 (a). Values of *x* are selected well below 0.5 to reflect spreading among only the first few adjacent sites. For the least spreading curve, the exciplex stays ~0.8-0.85 nm large, reflecting the minimum donor-acceptor separation set of 0.8 nm. For higher values of *x*, the exciplex spreads beyond 1 nm in size.

With a methodology to predict the distribution of electron-hole separation and their likelihood, the average energy of the exciplex can be predicted using a simple Coulombic binding model expressed as:

$$E = E_0 - \frac{C}{r} \quad (6.6)$$

where $C = \frac{e}{4\pi\epsilon_0\epsilon_r} = 0.48\ eV \cdot nm$ for a mixture with relative dielectric constant of 3. As previously discussed, the exciplex size, r, is a distributional quantity, and due to the non-linearity of Equation 6.6, the average separation cannot be used since: $\langle\frac{1}{r}\rangle \neq \frac{1}{\langle r\rangle}$. Rather, the average exciplex energy is computed as:

$$\langle E\rangle = \langle E_0 - \frac{A}{r}\rangle = E_0 - C\,\langle\frac{1}{r_0(1+x\cdot(A+D))}\rangle \quad (6.7)$$

From this, energy shifts can be computed by taking differences between energy and the minimum energy, which occurs at $f_d = 0.5$ or D:A ratio of 1:1. Shifts can similarly be evaluated for measured energies extracted for m-MTDATA:3TPYMB and mCP:PO-T2T systems, for which the later the minimum energy is observed near 1:1 D:A ratio. A comparison between shifts predicted by this model for delocalization ratios used in Figure 6.7 (a) are shown in Figure 6.7 (b-c). Best fitting simulations are indicated with a dashed line.

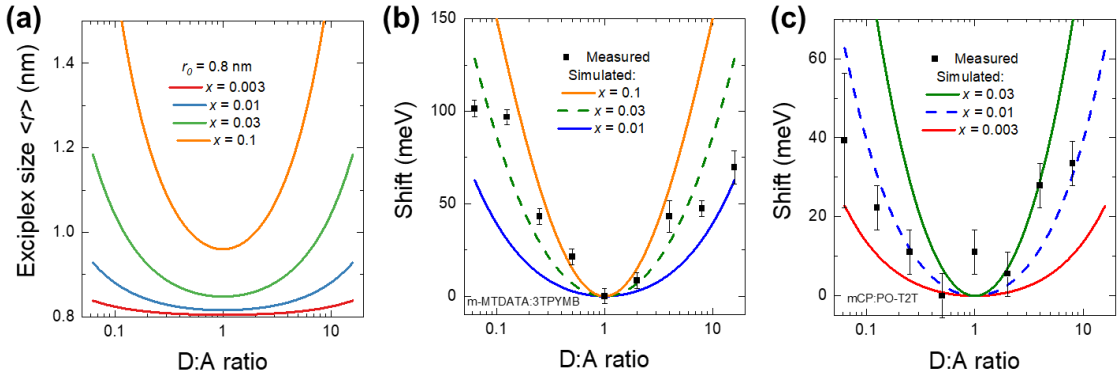

Figure 6.7 (a) Average electron-hole separations for exciplexes simulated for various delocalization ratios (*x*) across donor:acceptor ratios. (b) Simulated and measured exciplex energy shifts for m-MTDATA:3TPYMB mixtures (c) Simulated and measured exciplex energy shifts for mCP:PO-T2T.

The modeled shifts of Figure 6.7 reflect the roughly parabolic relationship between shift and the logarithm of D:A ratio observed in energies extracted from measurements of

mixture PL. Reasonable agreement between simulated and measured shifts can be achieved for x=0.03 for m-MTDATA:3TPYMB mixtures and x=0.01 for mCP:PO-T2T mixtures. For these delocalization ratios, the exciplex size is expected to extend from ~0.85 nm to 1.18 nm in m-MTDATA:3TPYMB and from ~0.82-0.93 in mCP:PO-T2T. The resulting reductions in binding energies for each mixture leads to the observed increases in energy. In this model, the property that is sensitive to the material system is the delocalization factor, which likely reflects the degree of orbital overlap between neighboring donor or acceptor molecules, leading to easier or harder delocalization. Further study would focus on physical interpretation of this parameter between different material systems. Alternate models beyond a simple delocalization factor are likely required, possibly including a self-limiting function for exciplex size where the size plateaus for highly unequal compositions. However, in this model, although exciplex size continues to increase, since exciplex energy varies inversely with carrier separation, the energy does plateau for extreme compositions.

6.5. Summary and future work

In this chapter, binary donor:acceptor mixture photoluminescence was measured across various D:A ratio compositions. In particular, m-MTDATA:3TPYMB was observed to blue-shift in emission energy at compositions rich one component compared to equal mixtures (1:1 D:A). Exciplex emission energy increases by 100 meV for 1:16 D:A mixtures and 70 meV for 16:1 D:A mixtures. A broadening of the exciplex emission spectra is observed of 20-40 meV, or about ~40% of the energy shift. Additionally, mCP:PO-T2T was measured at several compositions with a smaller 40 meV energy shift between donor or acceptor rich mixtures and equal or near-equal D:A mixtures, with up to 20 meV broadening, or ~50% of the observed shift. Possible sources of the shift effect are

considered with presentation of a carrier delocalization model dependent on donor and acceptor domain size, determined by mixture composition, is presented. Preliminary modeling results are able to reasonably predict an extension of the electron-hole separation for exciplexes in unequal mixtures of donor and acceptor. Further, the model can be fit to measured exciplex energy shift data to reflect the observed dependance across D:A ratios.

Significant further work is required to satisfactorily describe the dilution-dependent shift behavior observed, despite promising preliminary data and modeling findings. Future work should include examination of several more donor-acceptor systems to observe the composition-dependent shifts in a broader class of materials and provide further data for identification of material properties that impact the degree of shifts observed more generally. Further measurements are required to support the mechanism of shifts. Possible techniques include GIWAXS to identify any structural changes related to molecular orientation changing with composition. To explore the primary theory of delocalization, luminescence measurements with a wide-gap tertiary component could be used to disrupt delocalization, similar to the observations of Chapter 5 in doped bilayers. Additional spectroscopies for directly probing the domain size, electron-hole separation, or exciplex binding energy via optical or electrical means in the transient domain or across temperature could be used to provide further insight into the nanoscale variations of the D-A heterojunction and exciplex. Finally, improved models for carrier delocalization in blends can be developed to account for more physical treatment of spreading of the carrier in donor and acceptor domains. Treatment of domain size in higher dimensions that manage percolation of domains would be desirable, likely requiring a more complicated methodology such as kinetic Monte Carlo techniques. Additionally, advanced modeling

should consider sources of the asymmetry of shifts observed between donor and acceptor rich mixtures, which has initially been treated as effectively symmetric.

Although the results and mechanistic model for this work are preliminary, a significant sensitivity to mixture composition in binary mixtures is identified for a pair of donor-acceptor systems. In addition, a model that provides a framework for further detailed description of the effect is provided for later consideration.

7. Conclusion

This thesis explores emergent optical phenomena occurring at organic semiconductor interfaces. In Chapter 4, findings are presented pertaining to the length scale and mechanism of diffusion of exciplexes in donor-acceptor mixtures. Exciplex diffusion is measured via thickness-dependent photoluminescence quenching for the first time. This technique is applied for a variety of donor-acceptor pairings at various compositions to observe diffusion over ~1-7 nm. Exciton lifetime and carrier mobility data were used to decouple factors contributing to the exciton diffusion length and present design rules for extending or restricting the scale of exciplex diffusion. Additional findings clarified a novel mechanism of diffusion via sequential electron and hole transfer, which has not previously been observed for molecular excitons.

In Chapter 5, the influence of electric fields on the emission energy of exciplexes oriented at donor-acceptor bilayers is discussed. In forward bias, an applied-field dependent shift was observed through tuning of field via device architecture and bias to observe the giant Stark effect for organic exciplexes. Energy shifts up to 100 meV are observed. Further observations with reverse bias pulses showed carrier-generated fields can also shift emission in a transient manner, providing observation of the giant Stark effect in the time-domain. In addition, dilute bilayer devices were studied demonstrating the GSE as a sensitive probe of exciplex electron-hole separation.

In Chapter 6, preliminary measurements of binary donor-acceptor mixtures with various compositions are presented for a pair of systems. One system showed a composition-dependent emission energy shift of ~100 meV between equal and highly

donor- or acceptor-rich mixtures. Several sources of this sensitivity to composition are presented, with an initial model of carrier delocalization presented. The spreading of electrons and holes between molecules adjacent to the D-A interface is shown to predict the scaling of energy with composition observed. Further steps for more concrete observation of the effect of binary dilution on exciplex energy and determination of the origin of the effect are discussed.

Altogether, the results of this thesis provide further detail into methods to tune excited state energy transfer and manipulate the energy of exciplexes through materials selection or device engineering. These findings also provide mechanistic insights into phenomena observed in both thin film samples and devices, enriching the depth of knowledge of photophysical phenomena at organic donor-acceptor interfaces. These fundamental observations and practical strategies for tuning properties can be applied in device studies to more deeply understand the role of exciplex and CT state diffusion on OPV performance or to more precisely design complicated energy-transfer schemes in emissive layers of OLEDs. Additionally, phenomena previously observed in other emerging semiconductors such as III-V semiconductors or transition metal dichalcogenide heterostructures have been observed at organic interfaces, with relaxed requirements for low-temperature measurements on samples prepared with complicated materials synthesis and sample preparation. It is the author's hope that this work is applied to improving OPV and OLED device efficiency and possibly aids development of novel optoelectronics leveraging the emergent photophysics of semiconductor heterointerfaces.

8. References

[1] Y. Y. Deng, M. Haigh, W. Pouwels, L. Ramaekers, R. Brandsma, S. Schimschar, J. Grözinger, and D. de Jager, *Quantifying a Realistic, Worldwide Wind and Solar Electricity Supply*, Glob. Environ. Chang. **31**, 239 (2015).

[2] D. Gielen, F. Boshell, D. Saygin, M. D. Bazilian, N. Wagner, and R. Gorini, *The Role of Renewable Energy in the Global Energy Transformation*, Energy Strateg. Rev. **24**, 38 (2019).

[3] *EIA Fact Sheet- Generation*, https://www.eia.gov/tools/faqs/faq.php?id=427&t=3.

[4] *EIA Fact Sheet- Lighting*, https://www.eia.gov/tools/faqs/faq.php?id=99&t=3.

[5] S. K. Gupta, P. Jha, A. Singh, M. M. Chehimi, and D. K. Aswal, *Flexible Organic Semiconductor Thin Films*, J. Mater. Chem. C **3**, 8468 (2015).

[6] H. Bechert, T. Wehlus, S. Wittmann, and C. J. Brabec, *Flexible and Highly Segmented OLED for Automotive Applications*, 24 (2018).

[7] *Best Research-Cell Efficiencies*, https://www.nrel.gov/pv/assets/pdfs/pv-efficiency-chart.20190103.pdf.

[8] D. Kearns and M. Calvin, *Photovoltaic Effect and Photoconductivity in Laminated Organic Systems*, J. Chem. Phys. **29**, 950 (1958).

[9] B. R. Weinberger, M. Akhtar, and S. C. Gau, *Polyacetylene Photovoltaic Devices*, Synth. Met. **4**, 187 (1982).

[10] G. A. Chamberlain, *Organic Solar Cells: A Review*, Sol. Cells **8**, 47 (1983).

[11] C. W. Tang, *Two-Layer Organic Photovoltaic Cell*, Appl. Phys. Lett. **48**, 183 (1986).

[12] Y. Cui, Y. Xu, H. Yao, P. Bi, L. Hong, J. Zhang, Y. Zu, T. Zhang, J. Qin, J. Ren, Z. Chen, C. He, X. Hao, Z. Wei, and J. Hou, *Single-Junction Organic Photovoltaic Cell with 19% Efficiency*, Adv. Mater. **33**, (2021).

[13] P. Heinstein, C. Ballif, and L. E. Perret-Aebi, *Building Integrated Photovoltaics (BIPV): Review, Potentials, Barriers and Myths*, Green **3**, 125 (2013).

[14] A. Ghosh, *Potential of Building Integrated and Attached/Applied Photovoltaic (BIPV/BAPV) for Adaptive Less Energy-Hungry Building's Skin: A Comprehensive Review*, J. Clean. Prod. **276**, 123343 (2020).

[15] *Heliatek GmbH*, https://www.heliatek.com/.

[16] J. E. Carlé, M. Helgesen, O. Hagemann, M. Hösel, I. M. Heckler, E. Bundgaard, S. A. Gevorgyan, R. R. Søndergaard, M. Jørgensen, R. García-Valverde, S. Chaouki-Almagro, J. A. Villarejo, and F. C. Krebs, *Overcoming the Scaling Lag for*

Polymer Solar Cells, Joule **1**, 274 (2017).

[17] A. Karki, A. J. Gillett, R. H. Friend, and T. Q. Nguyen, *The Path to 20% Power Conversion Efficiencies in Nonfullerene Acceptor Organic Solar Cells*, Adv. Energy Mater. **2003441**, 1 (2020).

[18] *Ubiquitous Energy, Inc.*, https://ubiquitous.energy/.

[19] R. R. Lunt and V. Bulovic, *Transparent, near-Infrared Organic Photovoltaic Solar Cells for Window and Energy-Scavenging Applications*, Appl. Phys. Lett. **98**, (2011).

[20] E. Ravishankar, R. E. Booth, C. Saravitz, H. Sederoff, H. W. Ade, and B. T. O'Connor, *Achieving Net Zero Energy Greenhouses by Integrating Semitransparent Organic Solar Cells*, Joule **4**, 490 (2020).

[21] R. Meitzner, U. S. Schubert, and H. Hoppe, *Agrivoltaics—The Perfect Fit for the Future of Organic Photovoltaics*, Adv. Energy Mater. **11**, (2021).

[22] C. W. Tang and S. A. Vanslyke, *Organic Electroluminescent Diodes*, Appl. Phys. Lett. **51**, 913 (1987).

[23] *LG Group*, https://www.lg.com/.

[24] *Motorola, Inc.*, https://www.motorola.com/.

[25] R. Pode, *Organic Light Emitting Diode Devices: An Energy Efficient Solid State Lighting for Applications*, Renew. Sustain. Energy Rev. **133**, 110043 (2020).

[26] N. C. Giebink and S. R. Forrest, *Quantum Efficiency Roll-off at High Brightness in Fluorescent and Phosphorescent Organic Light Emitting Diodes*, Phys. Rev. B - Condens. Matter Mater. Phys. **77**, 1 (2008).

[27] K. W. Hershey and R. J. Holmes, *Unified Analysis of Transient and Steady-State Electrophosphorescence Using Exciton and Polaron Dynamics Modeling*, J. Appl. Phys. **120**, (2016).

[28] N. C. Erickson and R. J. Holmes, *Investigating the Role of Emissive Layer Architecture on the Exciton Recombination Zone in Organic Light-Emitting Devices*, Adv. Funct. Mater. **23**, 5190 (2013).

[29] R. J. Holmes, S. R. Forrest, Y. J. Tung, R. C. Kwong, J. J. Brown, S. Garon, and M. E. Thompson, *Blue Organic Electrophosphorescence Using Exothermic Host-Guest Energy Transfer*, Appl. Phys. Lett. **82**, 2422 (2003).

[30] C. Adachi, M. A. Baldo, M. E. Thompson, and S. R. Forrest, *Nearly 100% Internal Phosphorescence Efficiency in an Organic Light Emitting Device*, J. Appl. Phys. **90**, 5048 (2001).

[31] M. A. Baldo, D. F. O'Brien, Y. You, A. Shoustikov, S. Sibley, M. E. Thompson, and S. R. Forrest, *Highly Efficient Phosphorescent Emission from Organic*

Electroluminescent Devices, Nature **395**, 151 (1998).

[32] W. Y. Hung, G. C. Fang, S. W. Lin, S. H. Cheng, K. T. Wong, T. Y. Kuo, and P. T. Chou, *The First Tandem, All-Exciplex-Based Woled*, Sci. Rep. **4**, 4 (2014).

[33] P. Xiao, J. Huang, Y. Yu, and B. Liu, *Recent Developments in Tandem White Organic Light-Emitting Diodes*, Molecules **24**, (2019).

[34] P. Xiao, J. Huang, Y. Yu, J. Yuan, D. Luo, B. Liu, and D. Liang, *Recent Advances of Exciplex-Based White Organic Light-Emitting Diodes*, Appl. Sci. **8**, 1 (2018).

[35] Q. Wang, Q. S. Tian, Y. L. Zhang, X. Tang, and L. S. Liao, *High-Efficiency Organic Light-Emitting Diodes with Exciplex Hosts*, J. Mater. Chem. C **7**, 11329 (2019).

[36] M. Sarma and K. T. Wong, *Exciplex: An Intermolecular Charge-Transfer Approach for TADF*, ACS Appl. Mater. Interfaces **10**, 19279 (2018).

[37] K. Goushi, K. Yoshida, K. Sato, and C. Adachi, *Organic Light-Emitting Diodes Employing Efficient Reverse Intersystem Crossing for Triplet-to-Singlet State Conversion*, Nat. Photonics **6**, 253 (2012).

[38] Z. Yang, Z. Mao, Z. Xie, Y. Zhang, S. Liu, J. Zhao, J. Xu, Z. Chi, and M. P. Aldred, *Recent Advances in Organic Thermally Activated Delayed Fluorescence Materials*, Chem. Soc. Rev. **46**, 915 (2017).

[39] A. Köhler and H. Bässler, *Electronic Processes in Organic Semiconductors*, 1st ed. (Wiley-VCH Verlag GMbH & Co, Weinheim, Germany, 2015).

[40] N. J. Turro, *Modern Molecular Photochemistry* (Benjamin/Cummings Pub., Menlo Park, CA, 1978).

[41] J. L. Bredas, *Mind the Gap!*, Mater. Horizons **1**, 17 (2014).

[42] P. Peumans, A. Yakimov, and S. R. Forrest, *Small Molecular Weight Organic Thin-Film Photodetectors and Solar Cells*, J. Appl. Phys. **93**, 3693 (2003).

[43] T. R. Kafle, B. Kattel, T. Wang, and W. L. Chan, *The Relationship between the Coherent Size, Binding Energy and Dissociation Dynamics of Charge Transfer Excitons at Organic Interfaces*, J. Phys. Condens. Matter **30**, (2018).

[44] M. Muntwiler, Q. Yang, W. A. Tisdale, and X. Y. Zhu, *Coulomb Barrier for Charge Separation at an Organic Semiconductor Interface*, Phys. Rev. Lett. **101**, 1 (2008).

[45] X. Y. Zhu, Q. Yang, and M. Muntwiler, *Charge-Transfer Excitons at Organic Semiconductor Surfaces and Interfaces*, Acc. Chem. Res. **42**, 1779 (2009).

[46] M. Knupfer, *Exciton Binding Energies in Organic Semiconductors*, Appl. Phys. A Mater. Sci. Process. **77**, 623 (2003).

[47] C. Deibel, T. Strobel, and V. Dyakonov, *Role of the Charge Transfer State in Organic Donor-Acceptor Solar Cells*, Adv. Mater. **22**, 4097 (2010).

[48] S. B. Nam, D. C. Reynolds, C. W. Litton, R. J. Almassy, T. C. Collins, and C. M. Wolfe, *Free-Exciton Energy Spectrum in GaAs*, Phys. Rev. B **13**, 761 (1976).

[49] M. A. Green, *Improved Value for the Silicon Free Exciton Binding Energy*, AIP Adv. **3**, (2013).

[50] C. Kittel, *Introduction to Solid State Physics*, 5th ed. (John Wiley & Sons, Inc, New York, 1976).

[51] C. L. Braun, *Electric Field Assisted Dissociation of Charge Transfer States as a Mechanism of Photocarrier Production*, J. Chem. Phys. **80**, 4157 (1984).

[52] A. Liu, S. Zhao, S. B. Rim, J. Wu, M. Könemann, P. Erk, and P. Peumans, *Control of Electric Field Strength and Orientation at the Donor-Acceptor Interface in Organic Solar Cells*, Adv. Mater. **20**, 1065 (2008).

[53] M. Dressel, B. Gompf, D. Faltermeier, A. K. Tripathi, J. Pflaum, and M. Schubert, *Kramers-Kronig-Consistent Optical Functions of Anisotropic Crystals: Generalized Spectroscopic Ellipsometry on Pentacene*, Opt. Express **16**, 19770 (2008).

[54] G. M. Akselrod, P. B. Deotare, N. J. Thompson, J. Lee, W. A. Tisdale, M. A. Baldo, V. M. Menon, and V. Bulovic, *Visualization of Exciton Transport in Ordered and Disordered Molecular Solids*, Nat. Commun. **5**, 1 (2014).

[55] A. Köhler and H. Bässler, *Triplet States in Organic Semiconductors*, Mater. Sci. Eng. R Reports **66**, 71 (2009).

[56] M. Segal, A. Baldo, J. Holmes, R. Forrest, and G. Soos, *Excitonic Singlet-Triplet Ratios in Molecular and Polymeric Organic Materials*, Phys. Rev. B - Condens. Matter Mater. Phys. **68**, 1 (2003).

[57] S. R. Forrest and D. F. O'Brien, *Excitonic Singlet-Triplet Ratio in a Semiconducting Organic Thin Film*, Phys. Rev. B - Condens. Matter Mater. Phys. **60**, 14422 (1999).

[58] S. M. Menke and R. J. Holmes, *Exciton Diffusion in Organic Photovoltaic Cells*, Energy Environ. Sci. **7**, 499 (2014).

[59] K. W. Hershey and R. J. Holmes, *Unified Analysis of Transient and Steady-State Electrophosphorescence Using Exciton and Polaron Dynamics Modeling*, J. Appl. Phys. **120**, (2016).

[60] J. S. Bangsund, K. W. Hershey, and R. J. Holmes, *Isolating Degradation Mechanisms in Mixed Emissive Layer Organic Light-Emitting Devices*, ACS Appl. Mater. Interfaces **10**, 5693 (2018).

[61] J. S. Bangsund, J. R. Van Sambeek, N. M. Concannon, and R. J. Holmes, *Sub – Turn-on Exciton Quenching Due to Molecular Orientation and Polarization in Organic Light-Emitting Devices*, Sci. Adv. **6**, 1 (2020).

[62] W. A. Luhman and R. J. Holmes, *Investigation of Energy Transfer in Organic Photovoltaic Cells and Impact on Exciton Diffusion Length Measurements*, Adv. Funct. Mater. **21**, 764 (2011).

[63] T. Förster, *10th Spiers Memorial Lecture. Transfer Mechanisms of Electronic Excitation*, Discuss. Faraday Soc. **27**, 7 (1959).

[64] D. R. Haynes, A. Tokmakoff, and S. M. George, *Distance Dependence of Electronic Energy Transfer between Donor and Acceptor Adlayers: P-Terphenyl and 9,10-Diphenylanthracene*, J. Chem. Phys. **100**, 1968 (1994).

[65] L. A. A. Pettersson, L. S. Roman, and O. Inganäs, *Modeling Photocurrent Action Spectra of Photovoltaic Devices Based on Organic Thin Films*, J. Appl. Phys. **86**, 487 (1999).

[66] O. V. Mikhnenko, P. W. M. Blom, and T.-Q. Nguyen, *Exciton Diffusion in Organic Semiconductors*, Energy Environ. Sci. **8**, 1867 (2015).

[67] B. Yurash, H. Nakanotani, Y. Olivier, D. Beljonne, C. Adachi, and T. Q. Nguyen, *Photoluminescence Quenching Probes Spin Conversion and Exciton Dynamics in Thermally Activated Delayed Fluorescence Materials*, Adv. Mater. **31**, 1 (2019).

[68] J. D. A. Lin, O. V Mikhnenko, J. Chen, A. Ruseckas, A. Mikhailovsky, R. P. Raab, J. Liu, P. W. M. Blom, A. Loi, C. J. Garc, and D. W. Samuel, *Systematic Study of Exciton Di Ff Usion Length in Organic Semiconductors by Six Experimental Methods †*, Mater. Horizons **1**, 280 (2014).

[69] T. Zhang, D. B. Dement, V. E. Ferry, and R. J. Holmes, *Intrinsic Measurements of Exciton Transport in Photovoltaic Cells*, Nat. Commun. **10**, 1 (2019).

[70] P. L. Dos Santos, F. B. Dias, A. P. Monkman, and F. B. D. and A. P. M. Paloma L.dos Santos, *Investigation of the Mechanisms Giving Rise to TADF in Exciplex States*, J. Phys. Chem. C **11**, 6 (2013).

[71] X. Xiao, K. J. Bergemann, J. D. Zimmerman, K. Lee, and S. R. Forrest, *Small-Molecule Planar-Mixed Heterojunction Photovoltaic Cells with Fullerene-Based Electron Filtering Buffers*, Adv. Energy Mater. **4**, 1 (2014).

[72] W. Y. Hung, G. C. Fang, Y. C. Chang, T. Y. Kuo, P. T. Chou, S. W. Lin, and K. T. Wong, *Highly Efficient Bilayer Interface Exciplex for Yellow Organic Light-Emitting Diode*, ACS Appl. Mater. Interfaces **5**, 6826 (2013).

[73] M. Young, C. J. Traverse, R. Pandey, M. C. Barr, and R. R. Lunt, *Angle Dependence of Transparent Photovoltaics in Conventional and Optically Inverted Configurations*, Appl. Phys. Lett. **103**, (2013).

[74] C. M. Proctor, M. Kuik, and T. Q. Nguyen, *Charge Carrier Recombination in Organic Solar Cells*, Prog. Polym. Sci. **38**, 1941 (2013).

[75] K. Vandewal, L. Goris, I. Haeldermans, M. Nesládek, K. Haenen, P. Wagner, and J. V. Manca, *Fourier-Transform Photocurrent Spectroscopy for a Fast and Highly Sensitive Spectral Characterization of Organic and Hybrid Solar Cells*, Thin Solid Films **516**, 7135 (2008).

[76] K. Vandewal, K. Tvingstedt, A. Gadisa, O. Inganäs, and J. V. Manca, *On the Origin of the Open-Circuit Voltage of Polymer-Fullerene Solar Cells*, Nat. Mater. **8**, 904 (2009).

[77] S. N. Hood and I. Kassal, *Entropy and Disorder Enable Charge Separation in Organic Solar Cells*, J. Phys. Chem. Lett. **7**, 4495 (2016).

[78] L. Perdigón-Toro, H. Zhang, A. Markina, J. Yuan, S. M. Hosseini, C. M. Wolff, G. Zuo, M. Stolterfoht, Y. Zou, F. Gao, D. Andrienko, S. Shoaee, and D. Neher, *Barrierless Free Charge Generation in the High-Performance PM6:Y6 Bulk Heterojunction Non-Fullerene Solar Cell*, Adv. Mater. **32**, (2020).

[79] Y. Zou and R. J. Holmes, *Correlation between the Open-Circuit Voltage and Charge Transfer State Energy in Organic Photovoltaic Cells*, ACS Appl. Mater. Interfaces **7**, 18306 (2015).

[80] P. B. Deotare, W. Chang, E. Hontz, D. N. Congreve, L. Shi, P. D. Reusswig, B. Modtland, M. E. Bahlke, C. K. Lee, A. P. Willard, V. Bulovic, T. Van Voorhis, and M. A. Baldo, *Nanoscale Transport of Charge-Transfer States in Organic Donor-Acceptor Blends*, Nat. Mater. **14**, 1130 (2015).

[81] H. Kim and J. Kim, *Diffusion Mechanism of Exciplexes in Organic Optoelectronics*, Phys. Rev. Appl. **10**, 1 (2020).

[82] C. K. Lee, L. Shi, and A. P. Willard, *A Model of Charge-Transfer Excitons: Diffusion, Spin Dynamics, and Magnetic Field Effects*, J. Phys. Chem. Lett. **7**, 2246 (2016).

[83] B. Siegmund, A. Mischok, J. Benduhn, O. Zeika, S. Ullbrich, F. Nehm, M. Böhm, D. Spoltore, H. Fröb, C. Körner, K. Leo, and K. Vandewal, *Organic Narrowband Near-Infrared Photodetectors Based on Intermolecular Charge-Transfer Absorption*, Nat. Commun. **8**, (2017).

[84] Z. Tang, Z. Ma, A. Sánchez-Díaz, S. Ullbrich, Y. Liu, B. Siegmund, A. Mischok, K. Leo, M. Campoy-Quiles, W. Li, and K. Vandewal, *Polymer:Fullerene Bimolecular Crystals for Near-Infrared Spectroscopic Photodetectors*, Adv. Mater. **29**, 1 (2017).

[85] P. L. Dos Santos, F. B. Dias, and A. P. Monkman, *Investigation of the Mechanisms Giving Rise to TADF in Exciplex States*, J. Phys. Chem. C **120**, 18259 (2016).

[86] J. Shi and C. W. Tang, *Doped Organic Electroluminescent Devices with Improved*

Stability, Appl. Phys. Lett. **70**, 1665 (1997).

[87] W. Brütting and C. Adachi, *Physics of Organic Semiconductors*, 2nd ed. (Wiley-VCH Verlag & Co., Weinheim, Germany, 2012).

[88] N. C. Erickson and R. J. Holmes, *Engineering Efficiency Roll-Off in Organic Light-Emitting Devices*, Adv. Funct. Mater. **24**, 6074 (2014).

[89] A. Hofmann, M. Schmid, and W. Brütting, *The Many Facets of Molecular Orientation in Organic Optoelectronics*, Adv. Opt. Mater. **9**, (2021).

[90] T. D. Schmidt, T. Lampe, M. R. Daniel Sylvinson, P. I. Djurovich, M. E. Thompson, and W. Brütting, *Emitter Orientation as a Key Parameter in Organic Light-Emitting Diodes*, Phys. Rev. Appl. **8**, 037001 (2017).

[91] J. H. Lee, C. H. Chen, P. H. Lee, H. Y. Lin, M. K. Leung, T. L. Chiu, and C. F. Lin, *Blue Organic Light-Emitting Diodes: Current Status, Challenges, and Future Outlook*, J. Mater. Chem. C **7**, 5874 (2019).

[92] B. Zhao, Y. Miao, Z. Wang, K. Wang, H. Wang, Y. Hao, B. Xu, and W. Li, *High Efficiency and Low Roll-off Green OLEDs with Simple Structure by Utilizing Thermally Activated Delayed Fluorescence Material as the Universal Host*, Nanophotonics **6**, 1133 (2017).

[93] Y. Kawamura, K. Goushi, J. Brooks, J. J. Brown, H. Sasabe, and C. Adachi, *100% Phosphorescence Quantum Efficiency of Ir (III) Complexes in Organic Semiconductor Films*, Appl. Phys. Lett. **86**, 1 (2005).

[94] V. Bulović, A. Shoustikov, M. A. Baldo, E. Bose, V. G. Kozlov, M. E. Thompson, and S. R. Forrest, *Bright, Saturated, Red-to-Yellow Organic Light-Emitting Devices Based on Polarization-Induced Spectral Shifts*, Chem. Phys. Lett. **287**, 455 (1998).

[95] Y. Im, M. Kim, Y. J. Cho, J. A. Seo, K. S. Yook, and J. Y. Lee, *Molecular Design Strategy of Organic Thermally Activated Delayed Fluorescence Emitters*, Chem. Mater. **29**, 1946 (2017).

[96] Y. S. Park, K. H. Kim, and J. J. Kim, *Efficient Triplet Harvesting by Fluorescent Molecules through Exciplexes for High Efficiency Organic Light-Emitting Diodes*, Appl. Phys. Lett. **102**, 1 (2013).

[97] B. Zhang and Z. Xie, *Recent Applications of Interfacial Exciplex as Ideal Host of Power-Efficient OLEDs*, Front. Chem. **7**, 1 (2019).

[98] T. Hosokai, H. Matsuzaki, A. Furube, K. Tokumaru, H. Nakanotani, M. Yahiro, and C. Adachi, *58-2: Revealing the Excited-State Dynamics of Thermally Activated Delayed Fluorescence Molecules by Using Transient Absorption Spectroscopy*, Dig. Tech. Pap. - Soc. Inf. Disp. Int. Symp. **47**, 786 (2016).

[99] D. Graves, V. Jankus, F. B. Dias, and A. Monkman, *Photophysical Investigation of*

the Thermally Activated Delayed Emission from Films of M-MTDATA:PBD Exciplex, Adv. Funct. Mater. **24**, 2343 (2014).

[100] H. Abroshan, V. Coropceanu, and J. L. Brédas, *Hyperfluorescence-Based Emission in Purely Organic Materials: Suppression of Energy-Loss Mechanisms via Alignment of Triplet Excited States*, ACS Mater. Lett. **2**, 1412 (2020).

[101] C. Y. Chan, M. Tanaka, Y. T. Lee, Y. W. Wong, H. Nakanotani, T. Hatakeyama, and C. Adachi, *Stable Pure-Blue Hyperfluorescence Organic Light-Emitting Diodes with High-Efficiency and Narrow Emission*, Nat. Photonics **15**, 203 (2021).

[102] H. Nakanotani, T. Higuchi, T. Furukawa, K. Masui, K. Morimoto, M. Numata, H. Tanaka, Y. Sagara, T. Yasuda, and C. Adachi, *High-Efficiency Organic Light-Emitting Diodes with Fluorescent Emitters*, Nat. Commun. **5**, 1 (2014).

[103] M. Colella, A. Danos, and A. P. Monkman, *Less Is More: Dilution Enhances Optical and Electrical Performance of a TADF Exciplex*, J. Phys. Chem. Lett. **10**, 793 (2019).

[104] H. A. Al Attar and A. P. Monkman, *Electric Field Induce Blue Shift and Intensity Enhancement in 2D Exciplex Organic Light Emitting Diodes; Controlling Electron–Hole Separation*, Adv. Mater. **28**, 8014 (2016).

[105] M. Baldo, M. Deutsch, P. Burrows, H. Gossenberger, M. Gerstenberg, V. Ban, and S. Forrest, *Organic Vapor Phase Deposition*, Adv. Mater. **10**, 1505 (1998).

[106] H. Kim and J. Kim, *Recent Progress on Exciplex-Emitting OLEDs*, J. Inf. Disp. **20**, 105 (2019).

[107] Y. Kawamura, H. Sasabe, and C. Adachi, *Simple Accurate System for Measuring Absolute Photoluminescence Quantum Efficiency in Organic Solid-State Thin Films*, Japanese J. Appl. Physics, Part 1 Regul. Pap. Short Notes Rev. Pap. **43**, 7729 (2004).

[108] J. Meyer, S. Hamwi, M. Kröger, W. Kowalsky, T. Riedl, and A. Kahn, *Transition Metal Oxides for Organic Electronics : Energetics, Device Physics and Applications*, Adv. Funct. Mater. **24**, 5408 (2012).

[109] J. Kim, Y. Yi, J. W. Kim, S. H. Noh, and H. Kang, *Interfacial Energetics of NaCl-Organic Composite Layer at an OLED Anode*, J. Phys. D. Appl. Phys. **45**, (2012).

[110] B. F. Bory, P. R. F. Rocha, R. A. J. Janssen, H. L. Gomes, D. M. De Leeuw, and S. C. J. Meskers, *Lithium Fluoride Injection Layers Can Form Quasi-Ohmic Contacts for Both Holes and Electrons*, Appl. Phys. Lett. **105**, (2014).

[111] V. Bulović, R. Deshpande, M. E. Thompson, and S. R. Forrest, *Tuning the Color Emission of Thin Film Molecular Organic Light Emitting Devices by the Solid State Solvation Effect*, Chem. Phys. Lett. **308**, 317 (1999).

[112] C. F. Madigan and V. Bulović, *Solid State Solvation in Amorphous Organic Thin*

Films, Phys. Rev. Lett. **91**, 1 (2003).

[113] R. R. Lunt, N. C. Giebink, A. A. Belak, J. B. Benziger, and S. R. Forrest, *Exciton Diffusion Lengths of Organic Semiconductor Thin Films Measured by Spectrally Resolved Photoluminescence Quenching*, J. Appl. Phys. **105**, 053711 (2009).

[114] H. G. Tompkins, *VASE Training Manual*, 2nd ed. (J. A. Woollam Co. Inc., Lincoln, NE, 2008).

[115] D. B. Dement, M. Puri, and V. E. Ferry, *Determining the Complex Refractive Index of Neat CdSe/CdS Quantum Dot Films*, J. Phys. Chem. C **122**, 21557 (2018).

[116] G. E. Jellison, *Data Analysis for Spectroscopic Ellipsometry*, Thin Solid Films **234**, 416 (1993).

[117] S. M. Menke and R. J. Holmes, *Exciton Transport in an Organic Semiconductor Exhibiting Thermally Activated Delayed Fluorescence*, J. Phys. Chem. C **120**, 8502 (2016).

[118] S. M. Menke, W. A. Luhman, and R. J. Holmes, *Tailored Exciton Diffusion in Organic Photovoltaic Cells for Enhanced Power Conversion Efficiency*, Nat. Mater. **12**, 152 (2013).

[119] L. V. Butov, *Excitonic Devices*, Superlattices Microstruct. **108**, 2 (2017).

[120] D. Unuchek, A. Ciarrocchi, A. Avsar, K. Watanabe, T. Taniguchi, and A. Kis, *Room-Temperature Electrical Control of Exciton Flux in a van Der Waals Heterostructure*, Nature **560**, 340 (2018).

[121] K. G. Stamplecoskie, J. S. Manser, and P. V. Kamat, *Dual Nature of the Excited State in Organic-Inorganic Lead Halide Perovskites*, Energy Environ. Sci. **8**, 208 (2015).

[122] T. Zhu, L. Yuan, Y. Zhao, M. Zhou, Y. Wan, J. Mei, and L. Huang, *Highly Mobile Charge-Transfer Excitons in Two-Dimensional WS2/Tetracene Heterostructures*, Sci. Adv. **4**, 1 (2018).

[123] C. M. Proctor, M. Kuik, and T. Nguyen, *Charge Carrier Recombination in Organic Solar Cells*, Prog. Polym. Sci. **38**, 1941 (2013).

[124] S. M. Menke, A. Sadhanala, M. Nikolka, N. A. Ran, M. K. Ravva, S. Abdel-Azeim, H. L. Stern, M. Wang, H. Sirringhaus, T. Q. Nguyen, J. L. Brédas, G. C. Bazan, and R. H. Friend, *Limits for Recombination in a Low Energy Loss Organic Heterojunction*, ACS Nano **10**, 10736 (2016).

[125] Y. S. Park, S. Lee, K. H. Kim, S. Y. Kim, J. H. Lee, and J. J. Kim, *Exciplex-Forming Co-Host for Organic Light-Emitting Diodes with Ultimate Efficiency*, Adv. Funct. Mater. **23**, 4914 (2013).

[126] D. Zhang, M. Cai, Y. Zhang, Z. Bin, D. Zhang, and L. Duan, *Simultaneous*

Enhancement of Efficiency and Stability of Phosphorescent OLEDs Based on Efficient Forster Energy Transfer from Interface Exciplex, ACS Appl. Mater. Interfaces **8**, 3825 (2016).

[127] J. Lee, S. Cheng, S. Yoo, H. Shin, J. Chang, C. Wu, K. Wong, and J. Kim, *An Exciplex Forming Host for Highly Effi Cient Blue Organic Light Emitting Diodes with Low Driving Voltage,* Adv. Funct. Mater. **25**, 361 (2015).

[128] B. P. Rand, D. P. Burk, and S. R. Forrest, *Offset Energies at Organic Semiconductor Heterojunctions and Their Influence on the Open-Circuit Voltage of Thin-Film Solar Cells*, Phys. Rev. B - Condens. Matter Mater. Phys. **75**, 115327 (2007).

[129] M. Wykes, S. K. Park, S. Bhattacharyya, S. Varghese, J. E. Kwon, D. R. Whang, I. Cho, R. Wannemacher, L. Lüer, S. Y. Park, and J. Gierschner, *Excited State Features and Dynamics in a Distyrylbenzene-Based Mixed Stack Donor-Acceptor Cocrystal with Luminescent Charge Transfer Characteristics*, J. Phys. Chem. Lett. **6**, 3682 (2015).

[130] W. Chang, D. N. Congreve, E. Hontz, M. E. Bahlke, D. P. McMahon, S. Reineke, T. C. Wu, V. Bulović, T. Van Voorhis, and M. A. Baldo, *Spin-Dependent Charge Transfer State Design Rules in Organic Photovoltaics*, Nat. Commun. **6**, 6415 (2015).

[131] T. R. Kafle, B. Kattel, S. Wanigasekara, T. Wang, and W. Chan, *Spontaneous Exciton Dissociation at Organic Semiconductor Interfaces Facilitated by the Orientation of the Delocalized Electron – Hole Wavefunction*, Adv. Energy Mater. **10**, 1904013 (2020).

[132] M. Zhang, Y. Li, C. Li, W. Qin, and K. Gao, *Charge Separation from a " Cold " Charge-Transfer State Driven by a Nonuniform Electric Field in Polymer-Based Donor / Acceptor Heterojunctions*, J. Phys. Chem. C **122**, 20676 (2018).

[133] G. G. Malliaras, J. R. Salem, P. J. Brock, and C. Scott, *Electrical Characteristics and Efficiency of Single-Layer Organic Light-Emitting Diodes*, Phys. Rev. B **58**, 411 (1998).

[134] S. R. Scully and M. D. McGehee, *Effects of Optical Interference and Energy Transfer on Exciton Diffusion Length Measurements in Organic Semiconductors*, J. Appl. Phys. **100**, 034907 (2006).

[135] P. E. Shaw, A. Ruseckas, and I. D. W. Samuel, *Exciton Diffusion Measurements in Poly(3-Hexylthiophene)*, Adv. Mater. **20**, 3516 (2008).

[136] J. D. A. Lin, O. V. Mikhnenko, J. Chen, Z. Masri, A. Ruseckas, A. Mikhailovsky, R. P. Raab, J. Liu, P. W. M. Blom, M. A. Loi, C. J. García-Cervera, I. D. W. Samuel, and T. Q. Nguyen, *Systematic Study of Exciton Diffusion Length in Organic Semiconductors by Six Experimental Methods*, Mater. Horizons **1**, 280 (2014).

[137] D. Rai, J. S. Bangsund, J. G. Barriocanal, and R. J. Holmes, *Impact of Molecular Structure on Singlet and Triplet Exciton Diffusion in Phenanthroline Derivatives*, J. Mater. Chem. C **5**, (2020).

[138] Y. Ueda, H. Nakanotani, T. Hosokai, Y. Tanaka, H. Hamada, H. Ishii, S. Santo, and C. Adachi, *Role of Spontaneous Orientational Polarization in Organic Donor – Acceptor Blends for Exciton Binding*, Adv. Opt. Mater. **2000896**, (2020).

[139] M. Cölle and C. Gärditz, *Phosphorescence of Aluminum Tris(Quinoline-8-Olate)*, Appl. Phys. Lett. **84**, 3160 (2004).

[140] L. Zhu, K. Xu, Y. Wang, J. Chen, and D. Ma, *High Efficiency Yellow Fluorescent Organic Light Emitting Diodes Based on M-MTDATA/BPhen Exciplex*, Front. Optoelectron. **8**, 439 (2015).

[141] X. K. Liu, Z. Chen, C. J. Zheng, C. L. Liu, C. S. Lee, F. Li, X. M. Ou, and X. H. Zhang, *Prediction and Design of Efficient Exciplex Emitters for High-Efficiency, Thermally Activated Delayed-Fluorescence Organic Light-Emitting Diodes*, Adv. Mater. **27**, 2378 (2015).

[142] G. D. Scholes, R. D. Harcourt, and K. P. Ghiggino, *Rate Expressions for Excitation Transfer. III. An Ab Initio Study of Electronic Factors in Excitation Transfer and Exciton Resonance Interactions*, J. Chem. Phys. **102**, 9574 (1995).

[143] T. Yasuda, Y. Yamaguchi, D. C. Zou, and T. Tsutsui, *Carrier Mobilities in Organic Electron Transport Materials Determined from Space Charge Limited Current*, Jpn. J. Appl. Phys. **41**, 5626 (2002).

[144] P. N. Murgatroyd, *Theory of Space-Charge-Limited Current Enhanced by Frenkel Effect*, J. Phys. D Appl. Phys. **3**, 151 (1970).

[145] T. Matsushima, G. Jin, Y. Kanai, T. Yokota, S. Kitada, T. Kishi, and H. Murata, *Interfacial Charge Transfer and Charge Generation in Organic Electronic Devices*, Org. Electron. **12**, 520 (2011).

[146] W. Xu, Khizar-ul-Haq, Y. Bai, X. Y. Jiang, and Z. L. Zhang, *The Estimation of Electron Mobility of 4,7-Diphyenyl-1, 10-Phenanthroline Using Space-Charge-Limited Currents*, Solid State Commun. **146**, 311 (2008).

[147] D. Tanaka, T. Takeda, T. Chiba, S. Watanabe, and J. Kido, *Novel Electron-Transport Material Containing Boron Atom with a High Triplet Excited Energy Level*, Chem. Lett. **36**, 262 (2007).

[148] R. Pandey, A. A. Gunawan, K. A. Mkhoyan, and R. J. Holmes, *Efficient Organic Photovoltaic Cells Based on Nanocrystalline Mixtures of Boron Subphthalocyanine Chloride and C 60*, Adv. Funct. Mater. **22**, 617 (2012).

[149] L. Onsager, *Initial Recombination of Ions*, Phys. Rev. **54**, 554 (1938).

[150] Y. Roichman and N. Tessler, *Generalized Einstein Relation for Disordered*

Semiconductors - Implications for Device Performance, Appl. Phys. Lett. **80**, 1948 (2002).

[151] C. K. Moon, J. S. Huh, J. M. Kim, and J. J. Kim, *Electronic Structure and Emission Process of Excited Charge Transfer States in Solids*, Chem. Mater. **30**, 5648 (2018).

[152] A. A. High, J. R. Leonard, A. T. Hammack, M. M. Fogler, L. V. Butov, A. V. Kavokin, K. L. Campman, and A. C. Gossard, *Spontaneous Coherence in a Cold Exciton Gas*, Nature **483**, 584 (2012).

[153] Z. Wang, D. A. Rhodes, K. Watanabe, T. Taniguchi, J. C. Hone, J. Shan, and K. F. Mak, *Evidence of High-Temperature Exciton Condensation in Two-Dimensional Atomic Double Layers*, Nature **574**, 76 (2019).

[154] L. V. Butov, A. A. Shashkin, V. T. Dolgopolov, K. L. Campman, and A. C. Gossard, *Magneto-Optics of the Spatially Separated Electron and Hole Layers in GaAs/AlGaAs Coupled Quantum Wells*, Phys. Rev. B **60**, 8753 (1999).

[155] P. Nagler, G. Plechinger, M. V. Ballottin, A. Mitioglu, S. Meier, N. Paradiso, C. Strunk, A. Chernikov, P. C. M. Christianen, C. Schüller, and T. Korn, *Interlayer Exciton Dynamics in a Dichalcogenide Monolayer Heterostructure*, 2D Mater. **4**, 025112 (2017).

[156] J. Wang, Q. Shi, E. M. Shih, L. Zhou, W. Wu, Y. Bai, D. Rhodes, K. Barmak, J. Hone, C. R. Dean, and X. Y. Zhu, *Diffusivity Reveals Three Distinct Phases of Interlayer Excitons in MoSe2/WSe2 Heterobilayers*, Phys. Rev. Lett. **126**, 106804 (2021).

[157] Z. Vörös, R. Balili, D. W. Snoke, L. Pfeiffer, and K. West, *Long-Distance Diffusion of Excitons in Double Quantum Well Structures*, Phys. Rev. Lett. **94**, 226401 (2005).

[158] D. Unuchek, A. Ciarrocchi, A. Avsar, K. Watanabe, T. Taniguchi, and A. Kis, *Room-Temperature Electrical Control of Exciton Flux in a van Der Waals Heterostructure*, Nature **560**, 340 (2018).

[159] T. Zhu, L. Yuan, Y. Zhao, M. Zhou, Y. Wan, J. Mei, and L. Huang, *Highly Mobile Charge-Transfer Excitons in Two-Dimensional WS2/Tetracene Heterostructures*, Sci. Adv. **4**, eaao3104 (2018).

[160] U. Hörmann, S. Zeiske, F. Piersimoni, L. Hoffmann, R. Schlesinger, N. Koch, T. Riedl, D. Andrienko, and D. Neher, *Stark Effect of Hybrid Charge Transfer States at Planar ZnO/Organic Interfaces*, Phys. Rev. B **98**, 155312 (2018).

[161] N. Leisgang, S. Shree, I. Paradisanos, L. Sponfeldner, C. Robert, D. Lagarde, A. Balocchi, K. Watanabe, T. Taniguchi, X. Marie, R. J. Warburton, I. C. Gerber, and B. Urbaszek, *Giant Stark Splitting of an Exciton in Bilayer MoS2*, Nat. Nanotechnol. **15**, 901 (2020).

[162] E. Lorchat, M. Selig, F. Katsch, K. Yumigeta, S. Tongay, A. Knorr, C. Schneider, and S. Höfling, *Excitons in Bilayer MoS2 Displaying a Colossal Electric Field Splitting and Tunable Magnetic Response*, Phys. Rev. Lett. **126**, 037401 (2021).

[163] O. Karni, E. Barré, S. C. Lau, R. Gillen, E. Y. Ma, B. Kim, K. Watanabe, T. Taniguchi, J. Maultzsch, K. Barmak, R. H. Page, and T. F. Heinz, *Infrared Interlayer Exciton Emission in MoS2/WSe2 Heterostructures*, Phys. Rev. Lett. **123**, 247402 (2019).

[164] P. W. Atkins, *Molecular Quantum Mechanics*, 2nd ed. (Oxford University Press, 1983).

[165] F. Schindler, J. M. Lupton, J. Müller, J. Feldmann, and U. Scherf, *How Single Conjugated Polymer Molecules Respond to Electric Fields*, Nat. Mater. **5**, 141 (2006).

[166] M. Orrit, J. Bernard, A. Zumbusch, and R. I. Personov, *Stark Effect on Single Molecules in a Polymer Matrix*, Chem. Phys. Lett. **196**, 595 (1992).

[167] M. Colella, A. Danos, and A. P. Monkman, *Identifying the Factors That Lead to PLQY Enhancement in Diluted TADF Exciplexes Based on Carbazole Donors*, J. Phys. Chem. C **123**, 17318 (2019).

[168] T. Zhang, N. M. Concannon, and R. J. Holmes, *Migration of Charge-Transfer States at Organic Semiconductor Heterojunctions*, ACS Appl. Mater. Interfaces **12**, 31677 (2020).

[169] S. M. Menke, A. Cheminal, P. Conaghan, N. A. Ran, N. C. Greehnam, G. C. Bazan, T. Q. Nguyen, A. Rao, and R. H. Friend, *Order Enables Efficient Electron-Hole Separation at an Organic Heterojunction with a Small Energy Loss*, Nat. Commun. **9**, 1 (2018).

[170] E. Tutiš, D. Berner, and L. Zuppiroli, *Internal Electric Field and Charge Distribution in Multilayer Organic Light-Emitting Diodes*, J. Appl. Phys. **93**, (2003).

[171] I. H. Campbell and B. K. Crone, *Improving an Organic Photodiode by Incorporating a Tunnel Barrier between the Donor and Acceptor Layers*, Appl. Phys. Lett. **101**, 023301 (2012).

[172] D. J. Griffiths, *Introduction to Electrodynamics*, 4th ed. (Pearson Education, 2013).

[173] B. Laikhtman and R. Rapaport, *Exciton Correlations in Coupled Quantum Wells and Their Luminescence Blue Shift*, Phys. Rev. B - Condens. Matter Mater. Phys. **80**, 195313 (2009).

[174] B. Bernardo, D. Cheyns, B. Verreet, R. D. Schaller, B. P. Rand, and N. C. Giebink, *Delocalization and Dielectric Screening of Charge Transfer States in Organic Photovoltaic Cells*, Nat. Commun. **5**, (2014).

[175] A. N. Brigeman, M. A. Fusella, B. P. Rand, and N. C. Giebink, *Nonthermal Site Occupation at the Donor-Acceptor Interface of Organic Solar*, Phys. Rev. Appl. **10**, 1 (2018).

[176] T. D. Schmidt, T. Lampe, M. R. Daniel Sylvinson, P. I. Djurovich, M. E. Thompson, and W. Brütting, *Emitter Orientation as a Key Parameter in Organic Light-Emitting Diodes*, Phys. Rev. Appl. **8**, 037001 (2017).

[177] D. Yokoyama, *Molecular Orientation in Small-Molecule Organic Light-Emitting Diodes*, J. Mater. Chem. **21**, 19187 (2011).

[178] K. Cnops, G. Zango, J. Genoe, P. Heremans, M. V. Martinez-Diaz, T. Torres, and D. Cheyns, *Energy Level Tuning of Non-Fullerene Acceptors in Organic Solar Cells*, J. Am. Chem. Soc. **137**, 8991 (2015).

[179] A. Casey, S. D. Dimitrov, P. Shakya-Tuladhar, Z. Fei, M. Nguyen, Y. Han, T. D. Anthopoulos, J. R. Durrant, and M. Heeney, *Effect of Systematically Tuning Conjugated Donor Polymer Lowest Unoccupied Molecular Orbital Levels via Cyano Substitution on Organic Photovoltaic Device Performance*, Chem. Mater. **28**, 5110 (2016).

[180] J. Zhao, X. Du, S. Yuan, C. Zheng, H. Lin, and S. Tao, *Highly Efficient Green and Red OLEDs Based on a New Exciplex System with Simple Structures*, Org. Electron. **43**, 136 (2017).

[181] M. Cocchi, D. Virgili, G. Giro, V. Fattori, P. Di Marco, J. Kalinowski, and Y. Shirota, *Efficient Exciplex Emitting Organic Electroluminescent Devices*, Appl. Phys. Lett. **80**, 2401 (2002).

[182] S. K. Jeon and J. Y. Lee, *Highly Efficient Exciplex Organic Light-Emitting Diodes by Exciplex Dispersion in the Thermally Activated Delayed Fluorescence Host*, Org. Electron. **76**, 105477 (2020).

[183] Y. Guo, Y. Zhao, Y. Miao, L. Wang, T. Li, H. Wang, B. Xu, and J. Yu, *All-Exciplex-Based White Organic Light-Emitting Diodes by Employing an Interface-Free Sandwich Light-Emitting Unit Achieving High Electroluminescence Performance*, J. Mater. Chem. C **8**, 12247 (2020).

9. Appendices

A. List of Publication and Presentations

Publications

[6] **N. M. Concannon**, R. J. Holmes, "Giant Stark Effect of Organic Exciplex Photoluminescence", Under review **2022**

[5] J. S. Bangsund; J. R. Van Sambeek; **N. M. Concannon**; R. J. Holmes, "Sub–turn-on exciton quenching due to molecular orientation and polarization in organic light-emitting devices", *Science Advances* **2020**, 6 (32), eabb2659.

[4] T. Zhang*; **N. M. Concannon***; R. J. Holmes, "Migration of Charge-Transfer States at Organic Semiconductor Heterojunctions", *ACS Appl. Mater. Interfaces* **2020**, 12 (28), 31677-31686.

[3] C. A. Beaudette; J. T. Held; B. L. Greenberg; P. H. Nguyen; **N. M. Concannon**; R. J. Holmes; K. A. Mkhoyan; E. S. Aydil; U. R. Kortshagen, "Plasmonic nanocomposites of zinc oxide and titanium nitride", *J. Vac. Sci. & Technol. A* **2020**, 38 (4), 042404.

[2] B. Yan; **N. M. Concannon**; J. D. Milshtein; F. R. Brushett; Y. Surendranath, "A Membrane-Free Neutral pH Formate Fuel Cell Enabled by a Selective Nickel Sulfide Oxygen Reduction Catalyst", *Angew. Chemie.* **2017**, 129 (26), 7604-7607.

[1] J. M. Falkowski; **N. M. Concannon**; B. Yan; Y. Surendranath, "Heazlewoodite, Ni3S2: A Potent Catalyst for Oxygen Reduction to Water under Benign Conditions", *J. Am. Chem. Soc.* **2015**, 137 (25), 7978–7981.

Presentations

[6] **N. M. Concannon**; R. J. Holmes, "Electric-Field Induced Luminescence Shift for Excited States at Organic Semiconductor Interfaces", *AIChE Annual Meeting*, 11/2021.

[5] **N. M. Concannon**; R. J. Holmes, "Electrically-Tuning Luminescence from Organic Semiconductor Heterojunctions" *MRS Electronic Materials Conference*, 6/2021

[4] **N. M. Concannon**; R. J. Holmes, "Field-Induced Spectral Shift in Organic Charge-Transfer State Luminescence", *APS March Meeting*, 3/2021.

[3] **N. M. Concannon**; T. Zhang; R. J. Holmes, "Understanding and Tuning Charge-Transfer State Diffusion at Organic Semiconductor Heterojunctions", *AIChE Annual Meeting*, 11/2020.

[2] **N. M. Concannon**; T. Zhang; R. J. Holmes, "Extending Energy Transport Lengths in Organic Semiconductor Mixtures", *UMN IPRIME August Meeting*, 08/2020.

[1] **N. M. Concannon**; T. Zhang; R. J. Holmes, "Engineering Diffusion of Charge-Transfer States at Organic Semiconductor Heterojunctions", *UMN miniAPS March Meeting (a replacement session for the canceled American Physical Society March 2020 meeting)*, 03/2020.

B. Supporting Information for Chapter 4

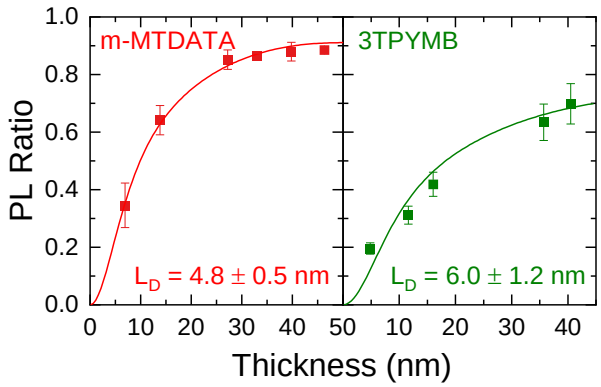

Figure B.1 m-MTDATA and 3TPYMB local singlet exciton diffusion. Measured and modeled thickness-dependent PL ratios for neat m-MTDATA and 3TPYMB with the extracted local singlet exciton diffusion length (L_D). m-MTDATA was pumped at a wavelength of λ = 370 nm on glass substrates with a 10-nm-thick exciton blocking layer of TAPC and a 10-nm-thick quenching layer of HATCN. 3TPYMB was pumped at λ = 330 nm on quartz substrates with a 15-nm-thick quenching layer of HATCN and no exciton blocking layers.

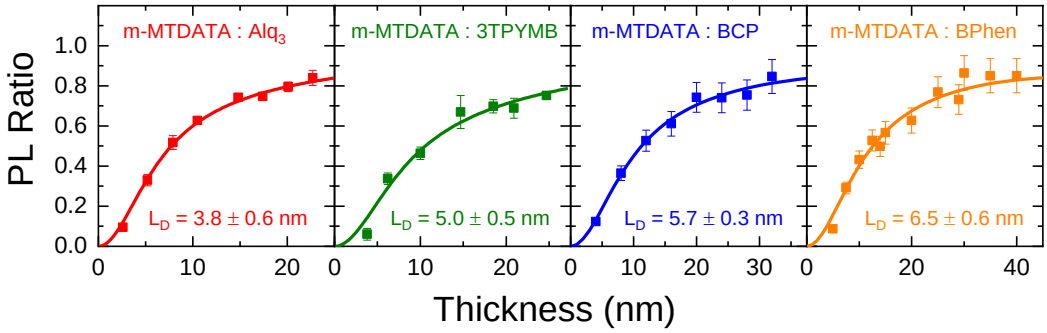

Figure B.2 CT state diffusion in m-MTDATA-acceptor mixtures. Thickness-dependent photoluminescence (PL) ratios and fitting results for equal mixtures of m-MTDATA-Alq_3, m-MTDATA-3TPYMB, m-MTDATA-BCP, and m-MTDATA-BPhen. A 10-nm-thick exciton blocking layer of TAPC are used for measurements with the acceptor Alq_3, while a 10-nm-thick layer of the acceptor is used in this capacity for all other acceptors. The results of m-MTDATA-BCP and m-MTDATA-BPhen mixed films were measured by Tao Zhang.

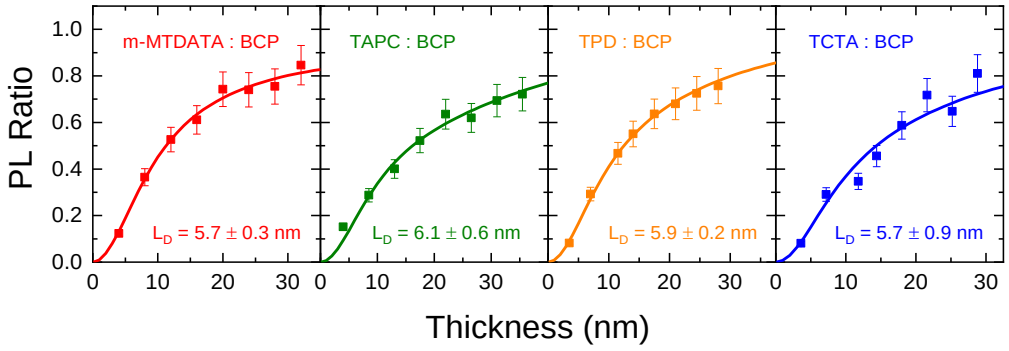

Figure B.3 CT state diffusion in donor-BCP mixtures. Thickness-dependent photoluminescence (PL) ratios and fitting results for equal mixtures of m-MTDATA-BCP, TAPC-BCP, TPD-BCP, and TCTA-BCP. A 3.5-10-nm-thick exciton blocking layer of the acceptor BCP are used for all measurements. Additionally, a 7-10-nm-thick quenching layer of HATCN is used. These measurements were performed by Tao Zhang.

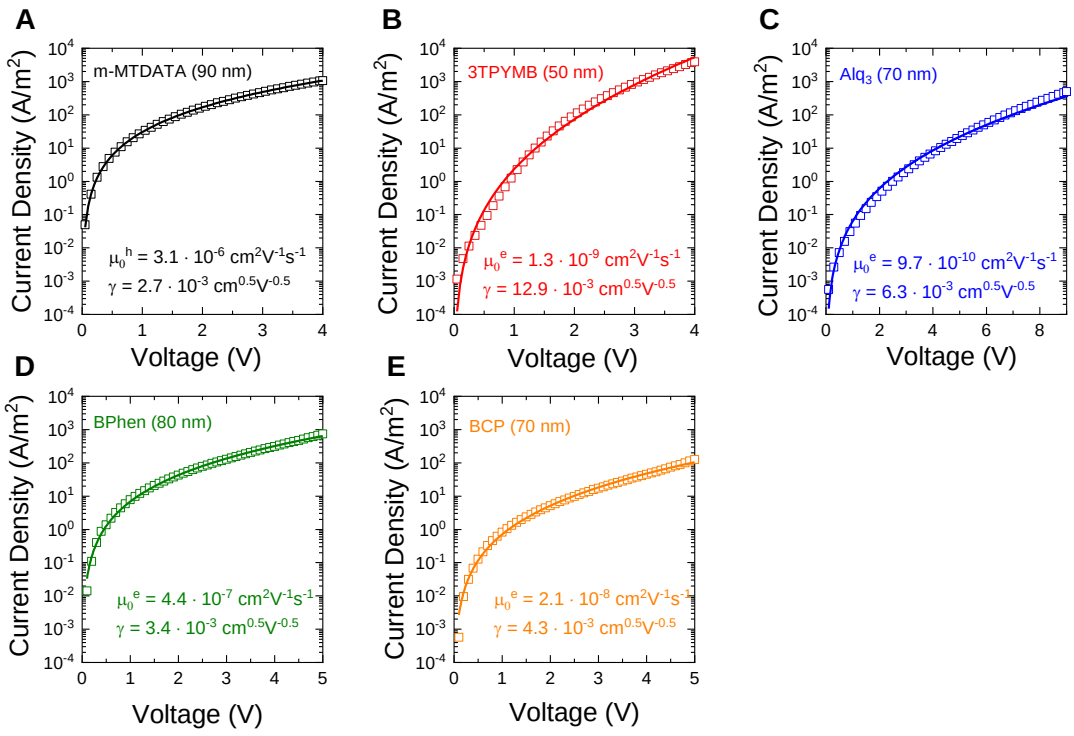

Figure B.4 Carrier mobility extraction for neat films of m-MTDATA and various acceptors. Current density-voltage (J-V) characteristic and space-charge-limited current (SCLC) fit for: (**A**) m-MTDATA (90 nm, hole-only), (**B**) 3TPYMB (50 nm, electron-only), (**C**) Alq_3 (70 nm, electron-only), (**D**) BPhen (80 nm, electron-only), and (**E**) BCP (70 nm, electron-only). Results for Alq_3, BPhen, and BCP were measured by Tao Zhang.

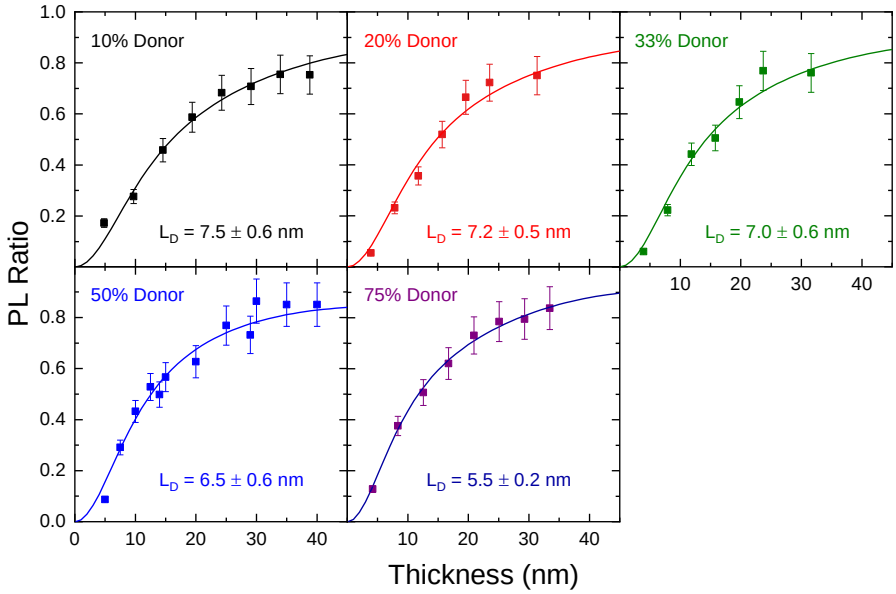

Figure B.5 CT state diffusion as a function of composition in mixtures of m-MTDATA-BPhen. Thickness-dependent photoluminescence (PL) ratios and fitting results for mixtures of 10, 20, 33, 50, and 75% donor m-MTDATA with BPhen. All measurements employed 10-nm-thick exciton blocking layers of the acceptor and 7-10-nm-thick exciton quenching layers of HATCN. These measurements were performed by Tao Zhang.

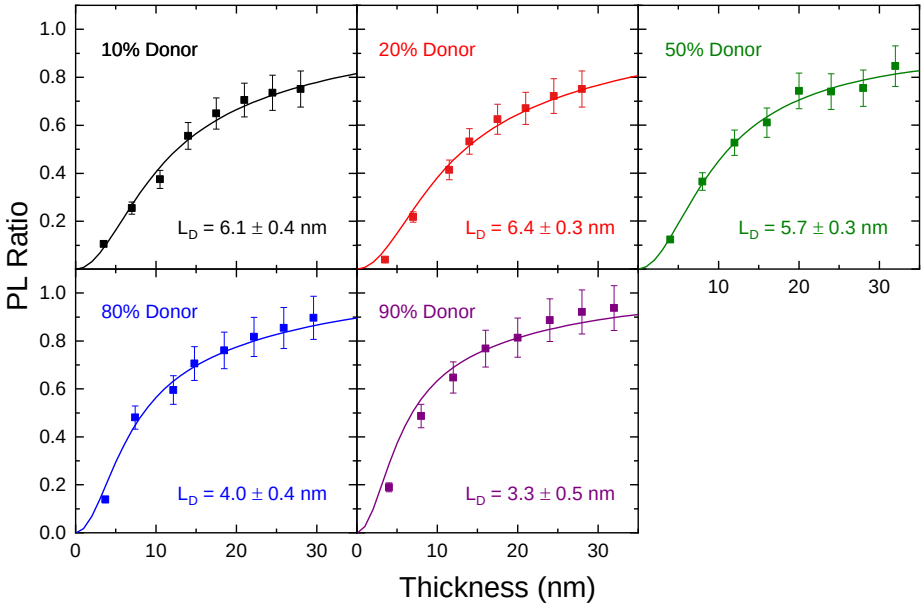

Figure B.6 CT state diffusion as a function of composition in mixtures of m-MTDATA-BCP. Thickness-dependent photoluminescence (PL) ratios and fitting results for mixtures of 10, 20, 50, 80, and 90% donor m-MTDATA with BCP. All measurements employed 10-nm-thick exciton blocking layers of the acceptor and 7-10-nm-thick exciton quenching layers of HATCN. These measurements were performed by Tao Zhang.

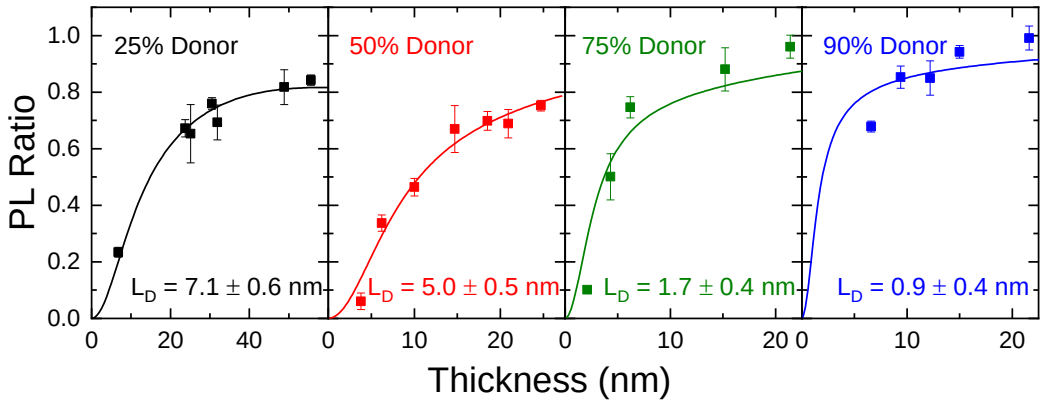

Figure B.7 CT state diffusion as a function of composition in mixtures of m-MTDATA-3TPYMB. Thickness-dependent photoluminescence (PL) ratios and fitting results for mixtures of 25, 50, 75, and 90% donor m-MTDATA with 3TPYMB. All measurements employed 10-nm-thick exciton blocking layers of the acceptor and 7-10-nm-thick exciton quenching layers of HATCN.

Table B.1 m-MTDATA-BPhen photoluminescence lifetime and mobility

Donor content (%)	τ_{prompt} (ns)	$\tau_{delayed}$ (μs)	μ_0^h (cm^2/Vs)	μ_0^e (cm^2/Vs)
10	149	2.04	$3.02 \cdot 10^{-11}$	$1.96 \cdot 10^{-9}$
20	152	1.91	$3.39 \cdot 10^{-11}$	$1.58 \cdot 10^{-10}$
50	154	1.88	$2.69 \cdot 10^{-8}$	$2.48 \cdot 10^{-11}$
75	137	1.95	$4.90 \cdot 10^{-7}$	$9.33 \cdot 10^{-12}$

C. Supporting Information for Chapter 5

C.1 Materials HOMO and LUMO energy levels:

Material	HOMO (eV)	LUMO (eV)	Source
m-MTDATA	5.1	2.0	[80,85]
3TPYMB	6.8	3.3	[80]
TAPC	5.5	2.0	[85]

C.2 Derivation of non-injection-type device field-bias relationship (Eq. 1):

Non-injection-type devices may be modeled as a compound dielectric stack, with negligible polaron concentration. The voltage difference, V, between the top Al and bottom ITO electrodes may be found by integrating the electric field within the device over the device thickness, z, which simplifies in the case of constant field within the i-th layer of thickness, t_i, as:

$$V = \int_{device} F dz = \sum_i F_i t_i \qquad \text{(C.1)}$$

Due to negligible charge density within the device, the dielectric displacement (D) is continuous and constant at all points within the layer stack [172], even while the field (F_i) in each layer will depend on dielectric constant (ϵ_i) as:

$$D = \epsilon_i F_i \qquad \text{(C.2)}$$

For a known applied voltage, as in our bias-dependent testing, Equations C.1 and C.2 may be combined to find the dielectric displacement within the device as:

$$D = \frac{V}{\sum_i \frac{t_i}{\epsilon_i}} \qquad \text{(C.3)}$$

Spectroscopic ellipsometry in the near-infrared (800-1100 nm) reveals that the donor *m*-MTDATA and acceptor 3TPYMB possess a similar dielectric constant of $\epsilon_{D/A} = 2.9$, while the insulator LiF has $\epsilon_{Ins} = 1.8$. The similarity of dielectric constant across the donor-acceptor interface, allows definition of a single interfacial field $F_{D/A}$ as:

$$F_{D/A} = \frac{1}{\epsilon_{D/A}} \frac{V}{\sum_i \frac{t_i}{\epsilon_i}} \qquad \text{(C.4)}$$

In the devices for this study, four layers are present: bottom insulator, acceptor, donor, and top insulator. Both insulator thicknesses may be combined into one total insulator thickness t_{Ins}, while donor and acceptor layer thicknesses are t_D and t_A, respectively, yielding:

$$F_{D/A} = \frac{V}{\frac{\epsilon_{D/A}}{\epsilon_{Ins}} t_{Ins} + t_A + t_D} \qquad \text{(C.5)}$$

This form of the field-voltage relationship is reproduced in Eq. 5.1.

C.3 Absorption and emission characteristics of exciplex-forming materials:

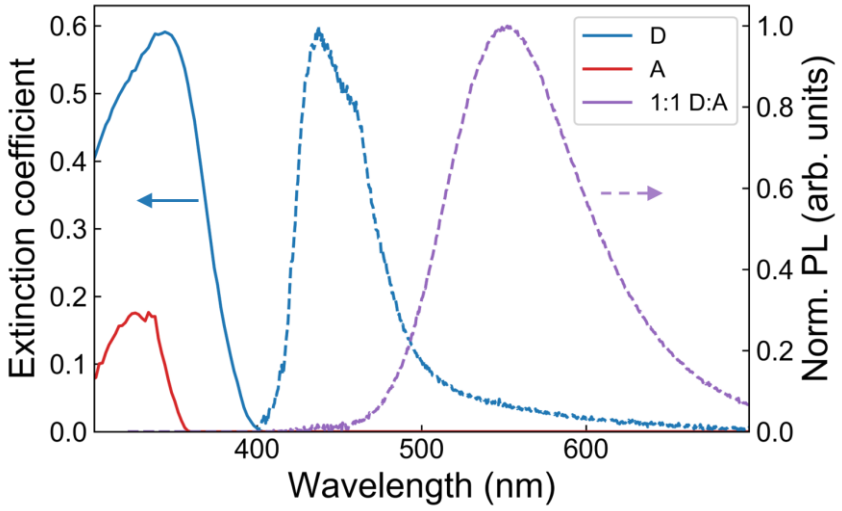

Figure C.1: Absorption and emission characteristics of exciplex-forming materials. Extinction coefficient spectra, derived from spectroscopic ellipsometry, of donor (D) m-MTDATA and acceptor (A), solid lines, left axis. Normalized photoluminescence spectra of neat m-MTDATA and 1:1 mixture of m-MTDATA:3TPYMB (1:1 D:A), dashed lines, right axis.

C.4 Energy extraction via fitting photoluminescence spectrum:

Normalized PL spectra recorded as a function of emission energy are fit with three Gaussian line-shapes in the form:

$$PL(E) = A_1 e^{-\frac{1}{2}\left(\frac{E-E_1}{\sigma_1}\right)^2} + A_2 e^{-\frac{1}{2}\left(\frac{E-E_2}{\sigma_2}\right)^2} + A_3 e^{-\frac{1}{2}\left(\frac{E-E_3}{\sigma_3}\right)^2} \qquad \text{(C.6)}$$

Each emission band is described with an amplitude (A_i), standard deviation (σ_i) and center energy (E_i). Non-linear least squares fitting (using the optimize.curve_fit method from the

Python scipy package) is employed to extract model parameters. Higher energy features ($E_i > 2.5$ eV) are assigned as local m-MTDATA emission, while the lowest energy feature ($E_i < 2.5$ eV) is assigned as exciplex emission. An example of fitting results is shown in Fig. C.1 with a comparison between measured and modeled data [Fig. C.2(a)] along with a residual spectrum of the difference between the measured and modeled data [Fig. C.2(b)]. The spectrum presented in Fig. C.2 is for a device with the architecture: ITO/40 nm LiF/20 nm 3TPYMB/5 nm m-MTDATA/90 nm LiF/Al under zero-bias (0 V), which is also included in Fig. 3(c).

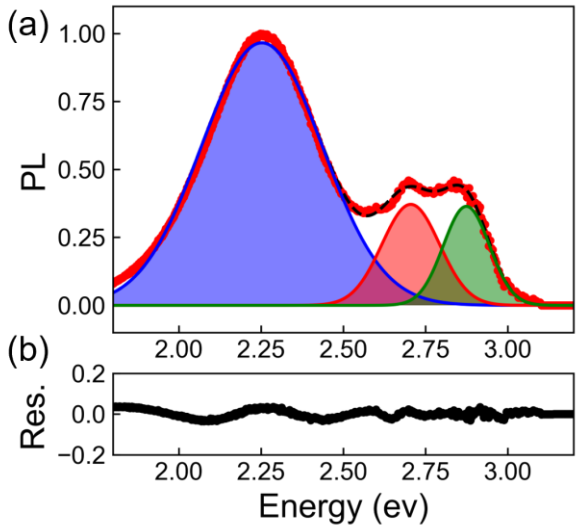

Figure C.2 (a) Gaussian fit results of PL spectrum with measured PL (red dots), individual modeled gaussians features (blue, red, and green filled areas) and total fit spectrum (black dashed line). **(b)** Residual difference between measured and total fit PL spectra.

Three Gaussian line-shapes adequately describe the recorded spectra with low residuals. Additionally, the high-energy features possess negligible tail intensity near the peak of the low energy feature, suggesting the exciplex energy assignment should be weakly sensitive to errors in modeling local emission fitting.

C.5 Exciton density calculation:

Illumination power density was measured using a Newport 818-UV silicon photodetector and was measured to be 5 W/m^2 with filtering for 370 nm illumination and no further attenuation. We estimate the generation rate of exciplexes at the D-A interface in our structures to be ~$6 \cdot 10^{17}$ m^{-2}s^{-1} at full power, assuming 20% exciton generation efficiency and 48% exciplex formation efficiency at the D-A interface. The generation efficiency is estimated by considering two-pass Beer's Law absorption, allowing for reflection off the cathode, in the donor of thickness (d) of 10 nm and an absorption coefficient (α) of 0.011 nm^{-1}, derived from the extinction coefficient of 0.32 at 370 nm from **Fig. C.1**, as $\eta_{abs} = e^{-\frac{2\alpha}{d}} = 0.20$. The formation efficiency is estimated from the m-MTDATA diffusion length

(L_D) of 5 nm yielding $\eta_{form} = \frac{L_D}{d}\tanh\frac{d}{L_D} = 0.48$, considering uniform exciton generation within the layer and quenching at only the D-A interface [168] This leads to a steady-state exciplex density of ~$6 \cdot 10^{11}$ m^{-2}, applying a 1 µs exciton lifetime [168].

We can estimate the interfacial site density from the molecular radius. The molecular radius (r) of m-MTDATA can be estimated from its bulk density (ρ) as $r = \sqrt[3]{\frac{3Mf}{4\pi\rho N_A}}$. The molecular weight of m-MTDATA (M) is 790 g/mol, a packing fraction (f) of 0.52 assumes a cubic arrangement of molecules, and N_A is Avogadro's number. Thus, the m-MTDATA density of 1.1 g/cm^3 predicts a molecular radius of 0.53 nm. We can then predict a 2-D packing density $n = \frac{1}{(2r)^2}$, in a square arrangement, of ~$9 \cdot 10^{17}$ m^{-2}. This site density is substantially larger than the estimated exciplex density above, such that a small fraction (< 1 in 10^6 sites) of sites is occupied during measurement. At this low level of excitation, it is expected that exciplex-exciplex interactions are negligible and observed behaviors may be attributed to the impact of field on individual exciplexes.

C.6 Time-dependent biased-PL spectra:

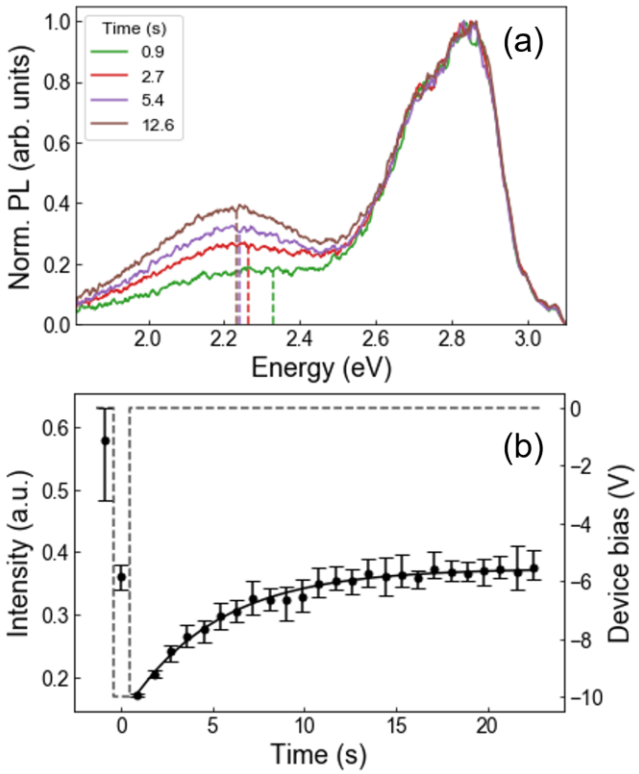

Figure C.3: (a) Normalized biased PL spectra at zero-bias measured over time. **(b)** Exciplex emission intensity, relative to local emission, as a function of time after a -10 V bias pulse at t=0.

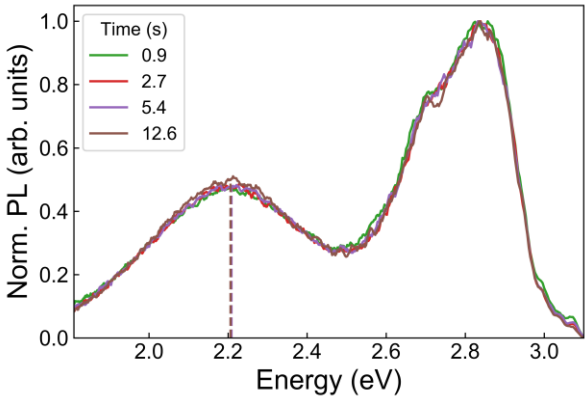

Figure C.4 Extracted exciplex emission energy as a function of time after a 10 V pulse at t=0.

C.7 Exciplex energy shifts under applied field for dilute donor-acceptor bilayers:

Photoluminescence spectra were collected as previously described for devices with architecture: ITO/80 nm LiF/20 nm 3TPYMB:TAPC/10 nm *m*-MTDATA:TAPC/40 nm LiF/Al under biases between 0 and 10V, in 2 V steps as shown in Figure 5.8. Extracted exciplex energy shifts for dilute are shown in Fig. C.5. The volume fraction of donor and acceptor (with remainder comprised by dilutant TAPC) are listed by volume percent. Shifts and field are calculated as earlier described for devices with neat donor and acceptor layers. Fit lines for extracted dipole moments, as presented in Table 5.1 are also shown.

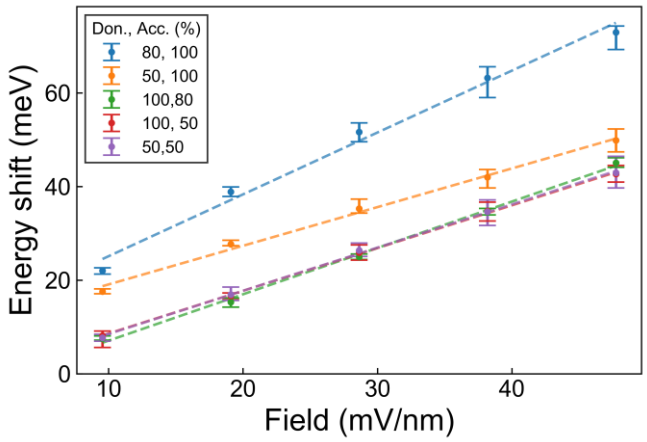

Figure C.5: Exciplex energy shifts for dilute donor-acceptor bilayer devices are shown as points with applied electric field for various dilutions of one or both layers, with donor and acceptor content listed by volume percent. Linear fits lines for each dilution are depicted by solid lines of the same color. Note: Dilutions of (D,A): (100,80), (100, 50), and (50,50) are nearly coincident.

D. Simulation codes

D.1 Iterative fit function for TDPQ fitting

```
clear all
close all

lambda = 370; %Wavelength of pump light (nm)
layersc = {'Air';'LiF'; 'mmtdata-bphen-1:3'; 'LiF'; 'SiO2abs'; 'Air'}; %
Names of layers of materials starting from side of light incidence ending with
air
layersq = {'Air'; 'HATCN'; 'mmtdata-bphen-1:3'; 'LiF'; 'SiO2abs'; 'Air'}; %
Names of layers of materials starting from side of light incidence ending with
air

PLlayerc=3; %layer that photoemission is measured for, air IS counted
PLlayerq=3; %layer that photoemission is measured for, air IS counted
%First layer must be air, working on optical inversion now
s=9.5; %Buffer layer thickness
c=s; %capping layer thickness
q=12.8; %quenching layer thickness
dc=[0; c; NaN; s; 1e6; 0];  % thickness of each corresponding layer in nm
(thickness of the first and last layers are irrelivant -->semi-infinite)
dq=[0; q; NaN; s; 1e6; 0];
air_angle=70; %incident angle through air, in degrees
polarization='s'; %light polarization state, can handle only s and p for now
steps=1e2; %if sumTot does not add to 1, increase number of steps, Atf is
numerically integrated, so errors may be present

dAL=[5.4, 7.5, 8.5, 10.6, 15.8, 17.9]; %Active layer thicknesses (nm)
dALerr=0*ones(1,length(dAL));%Active layer thickness errrors (nm)
Ld0=10; %Initial guess on Ld for active layer (nm)

PLRatioMeasured=[0.16545
0.33669
0.30875
0.43221
0.45188
0.5502]; %dual bg subtraction and hatcn only agree
PLRatioMeasurederr=0.1*PLRatioMeasured;% Experimental error

plotdata={}; %for origin plotting if desired
plotdata{end+1}=[dAL; dALerr ;PLRatioMeasured';PLRatioMeasurederr']';

libname='Index_of_Refraction_WorkingLibraryNC.xls';
nc=getNandK(layersc,lambda,libname); %complex numbers, rows layers, columns
wavelengths
nq=getNandK(layersq,lambda,libname); %complex numbers, rows layers, columns
wavelengths
%Estimated variables below;
%Active Layer (AL)
theta=1; % theta -exciton generation quantum efficiency in active layer
tau=1e-6; % tau - exciton lifetime in active layer (s)
BCsc={'hn','hn'}; %active layer boundary conditions
BCsq={'hd','hn'}; %active layer boundary conditions
```

```
fun=@(Ld)
norm(PLRatioSim(lambda,PLlayerc,PLlayerq,dc,dq,air_angle,polarization,s
teps,dAL,Ld,nc,nq,theta,tau,BCsc,BCsq)-PLRatioMeasured);
[Ld,fval,exitflag]=fmincon(fun,[Ld0],[],[],[],[],[0],[],[]);
PLRcalc=PLRatioSim(lambda,PLlayerc,PLlayerq,dc,dq,air_angle,polarizatio
n,steps,dAL,Ld,nc,nq,theta,tau,BCsc,BCsq);

%Fit quality evaluation (plot 1)
epsilon=0.7; %0<epsilon<1, smaller uses broader fit, larger uses narrower fit
Ldtest=linspace(epsilon,1/epsilon)*Ld;
for i=1:length(Ldtest)
    err(i)=fun(Ldtest(i));
end
f = fit(Ldtest.',1./err.','gauss2')
figure()
plot(f,Ldtest,1./err)
set(gca, 'XScale', 'log');
a1=0.1944;
b1= 5.525;
c1=0.8447;
pLd=a1.*exp(-((Ldtest-b1)./c1).^2); %Ld prob density function
Ldmean=sum(pLd.*Ldtest)/sum(pLd);
Lderr=1.96*std(Ldtest,pLd); %for 95% CI
name=['Ld is: ',num2str(Ld,2),char(177),num2str(Lderr,2)];
disp(name)
disp('Please update a1 ,b1, and c1')

ds=linspace(0.1,max(dAL)*1.1);
OpticalPLR=PLRatioSim(lambda,PLlayerc,PLlayerq,dc,dq,air_angle,polariza
tion,steps,ds,Ld,nc,nq,theta,tau,BCsc,BCsc);

PLRmodeled=[]; %simulate PLR for several Ld's
Lds=[Ld-Lderr,Ld,Ld+Lderr];
hold on
name=[];
for i=1:length(Lds)

PLRmodeled(i,:)=PLRatioSim(lambda,PLlayerc,PLlayerq,dc,dq,air_angle,pol
arization,steps,ds,Lds(i),nc,nq,theta,tau,BCsc,BCsq);
end

%Figure with data, OPLR, and shaded error region on fitted model
figure()
hold on
errorbar(dAL,PLRatioMeasured,PLRatioMeasurederr,PLRatioMeasurederr,'ok')
%
errorbar(dAL,PLRatioMeasured,PLRatioMeasurederr,PLRatioMeasurederr,dALerr,dALer
r,'ok')
plot(ds,OpticalPLR,'--k')
plot(ds,PLRmodeled(2,:),'k') %plot this to trick the legend into labeling
model with error bars as a thin line
plotdata{end+1}=[ds; PLRmodeled(2,:); PLRmodeled(1,:)-PLRmodeled(2,:);
PLRmodeled(2,:)-PLRmodeled(3,:); OpticalPLR]';

shadedErrorBar(ds,PLRmodeled(2,:),[PLRmodeled(1,:)-PLRmodeled(2,:);
PLRmodeled(2,:)-PLRmodeled(3,:)])
box on
xlim([min(ds),max(ds)])
```

```
xlabel('Blend Thickness (nm)','fontsize',18)
ylim([0,max(max(OpticalPLR),1.1)])
ylabel('PL Ratio','fontsize',18)
qname=['Model: Ld=',num2str(Ld,2),char(177),num2str(Lderr,2),'nm'];
legend({'Measurement','Optical
Limit',qname},'fontsize',14,'location','southeast')
set(gca,'fontsize',18)
function
PLRs=PLRatioSim(lambda,PLlayerc,PLlayerq,dc,dq,air_angle,polarization,s
teps,dAL,Ld,nc,nq,theta,tau,BCsc,BCsq)
    for i=1:length(dAL)
        dtemp=dc;
        dtemp(PLlayerc)=dAL(i);

PLc(i)=PLsim(lambda,PLlayerc,dtemp,air_angle,polarization,steps,nc,Ld,t
heta,tau,BCsc);
    end
    for i=1:length(dAL)
        dtemp=dq;
        dtemp(PLlayerq)=dAL(i);

PLq(i)=PLsim(lambda,PLlayerq,dtemp,air_angle,polarization,steps,nq,Ld,t
heta,tau,BCsq);
    end
    PLRs=PLq./PLc;
end

function
PL=PLsim(lambda,PLlayer,d,air_angle,polarization,steps,n,Ld,theta,tau,B
Cs)

out=SimpInvertedOpticalModel(lambda,d,air_angle,polarization,n,steps);
    x=cell2mat(out(1));
    Q=cell2mat(out(2));
    RATAs=cell2mat(out(4));
    if abs(1-sum(RATAs))>0.01
        1-sum(RATAs)
        disp('RATAs not summing to 1')
    end
    begin=(PLlayer-2)*steps+1;
    finish=(PLlayer-2+1)*steps;
    xact=x(begin:finish);
    Qact=Q(begin:finish);
    C=CenterFDsolver(Ld,theta,tau,lambda,d(PLlayer),Qact,BCs);
%calculate exciton denisty profile (a.u.)
    PL=trapz(xact,C);
end
function n=getNandK(layers,lambda,libname)
    n=zeros(length(layers),length(lambda)); %rows layers, columns
wavelengths
    [data,dataNames]=xlsread(libname);
    fileLambda=data(:,1); %Wavelengths from first column
    for i=1:length(layers)
        nindex=find(strcmp(strcat(layers(i),'_n'),dataNames));
        ndata=data(:,nindex);
        kindex=find(strcmp(strcat(layers(i),'_k'),dataNames));
        kdata=data(:,kindex);
        n_interp=interp1(fileLambda,ndata,lambda);
```

```
        k_interp=interp1(fileLambda,kdata,lambda);
        n(i,:)=n_interp'+1i*k_interp';
    end
end
```

D.2 Optical Model Simulation code

```
function out=SimpInvertedOpticalModel(lambda,d,air_angle,polarization,n,steps)
    %Calculate substrate reflectivity
    ns=n(end-1);
    na=n(end);
    qs=sqrt(ns^2-na^2*sin(air_angle)^2);
    qa=sqrt(na^2-na^2*sind(air_angle)^2);
    if polarization=='s'
        rs=(qs-qa)./(qs+qa);
        ts=2*qs/(qs+qa);
    elseif polarization=='p'
        rs=(ns.^2.*qa-na.^2.*qs)./(na.^2.*qs+ns.^2.*qa);
        ts=2*ns*na.*qs./((na.^2.*qs+ns^2.*qa));
    end
    Rs=abs(rs)^2;
          Ts=abs(ts)^2*real(qa/qs);


    %Treat absorbing substrate
    alphas=4*pi*imag(ns)/lambda;
    beta=exp(-alphas*d(end-1)); %fraction of light transmitted from one side of substrate
to the other (1-Abs for 1 pass)
    %substrate absorption NOT complete for inverted cell


    % From air side
    dl=d(1:end-1);
```

```
nl=n(1:end-1);
angle_in=air_angle;
TMMl=solveTMM(lambda,dl,nl,angle_in,polarization,steps);
Rtfl=cell2mat(TMMl(1));
Ttfl=cell2mat(TMMl(2));
xl=cell2mat(TMMl(3));


% Intensity and wave transmission coefficient correction factors from
% air incident to stack incident (here also air, so all factors are
% unity)
Tadjl=1; %Tadj=1 for light incident on thin films from air
tadjl=Tadjl^.5*real(qa/qs);  %Fresnel transmission coefficient from air propogating to right to substrate propogating to left
Esql=tadjl*cell2mat(TMMl(4));
Ql=Tadjl*cell2mat(TMMl(5));
%Calculate power dissipation per area at each wavelength for each layer
for j=1:length(nl)-2
    begin=(j-1)*steps+1; %Indices for range of E-fields values. 1, 101, 201, etc.
    finish=j*steps; %100, 200, 300, etc.
    xj=xl(begin:finish); %Only use x and E range for single film at a time
    Ajl(j,1)=trapz(xj,Ql(begin:finish))/Tadjl; %Absorbtion coefficient for individual absorbing layers (fraction of incident light absorbed)
end
Atfl=sum(Ajl); %absorption coefficient for thin film stack from air incident light


% From glass side
dr=flipud(d(1:end-1));
nr=flipud(n(1:end-1));
```

```
    angle_in=asind(1/real(nr(1))*sind(air_angle)); %snell's law from air ambient to
substrate

    TMMr=solveTMM(lambda,dr,nr,angle_in,polarization,steps);

    Rtfr=cell2mat(TMMr(1));

    Ttfr=cell2mat(TMMr(2));

    xr=cell2mat(TMMr(3));


    % Intensity and wave transmission coefficient correction factors from

    % air incident to stack incident (here substrate, so all factors are

    % NOT unity). This makes comparisons between Ql and Qr along with Esql

    % and Esqr meaningful. This may not be correct for Esq or tadjr, but is

    % for Q.

    Tadjr=(beta^2*Ttfl*Rs)/(1-beta^2*Rs*Rtfr); %for substrate-thin film stack interface

    tadjr=Tadjr^.5*real(qa/qs); %Fresnel transmission coefficient from air propogating to
right to substrate propogating to left

    Esqr=tadjr*cell2mat(TMMr(4));

    Qr=Tadjr*cell2mat(TMMr(5));

    %Calculate power dissipation per area at each wavelength for each layer

    for j=1:length(nr)-2

        begin=(j-1)*steps+1; %Indices for range of E-fields values. 1, 101, 201, etc.

        finish=j*steps; %100, 200, 300, etc.

        xj=xr(begin:finish); %Only use x and E range for single film at a time

        Ajr(j,1)=trapz(xj,Qr(begin:finish))/Tadjr; %Absorbtion coefficient for individual
absorbing layers (fraction of incident light absorbed)

    end

    Atfr=sum(Ajr); %absorption coefficient for thin film stack from air incident light

%     fprintf('Rtfl \t\t Atfl \t\t Ttfl \t\t Rtfr \t\t Atfr \t\t Ttfr \t\t Rs \t\t Ts \n')

%     fprintf('%4.4f \t %4.4f \t %4.4f \t %4.4f \t %4.4f \t %4.4f \t %4.4f \t %4.4f \n',Rtfl,
Atfl,Ttfl,Rtfr,Atfr,Ttfr,Rs,Ts)
```

```
%     IParmNames=["Rtfl","Atfl","Ttfl","Rtfr","Atfr","Ttfr","Rs","Ts"};
     InterfaceParameters=[Rtfl,Atfl,Ttfl,Rtfr,Atfr,Ttfr,Rs,Ts];


    Reflected=Rtfl; %+Tadjr*Ttfr;
    Absorbedl=Atfl;
    %Absorbedr=Atfr*Tadjr;
    Transmitted=beta*Ttfl;%*Ts/(1-beta^2*Rs*Rtfr);
    AbsorbedSub=(1-beta)*Ttfl;
    sumTot=Reflected+Absorbedl+Transmitted+AbsorbedSub;
    RATAs=[Reflected,Absorbedl,Transmitted,AbsorbedSub];
%     SParmNames=["R","Al","Al","T","Total"];
%
StackParameters=[Reflected,Absorbedl,Absorbedr,Transmitted,AbsorbedSub,sumTot];
%     fprintf('R \t\t Al \t\t Ar \t\t T \t\t Total \n')
%     fprintf('%4.4f \t %4.4f \t %4.4f \t %4.4f \t %4.4f \n',Reflected, Absorbedl,
Absorbedr,Transmitted,sumTot)
%
%     figure()
%     plot(xl,Esql,sum(d)-xr,Esqr)
%     legend('Left','Right')
%     xlabel('Position (nm)')
%     ylabel('|E|^{2}')
%     title('|E|^{2} distribution in films')
%
%     figure()
%     plot(xl,Ql,sum(d)-xr,Qr)
%     legend('Left','Right')
%     xlabel('Position (nm)')
%     ylabel('Norm. Abs. Q/I0 (nm^{-1})')
```

```
%     title('Absorption distribution in films')
    x=xl;
    Q=Ql;%+fliplr(Qr);
    Esq=Esql;%+fliplr(Esqr);
    Absorbedj=Ajl;%+fliplr(Tadjr*Ajr);
    Atot=Atfl;%+Atfr*Tadjr;
    %AbsFracFromRight=Atfr*Tadjr/Atot;
%Package outputs:
% x-position map for Q and Esq
% Q-Normalized (to I_0) power disipation distribution throughout stack,
% Esq-|E|^2 electric field distribution in stack
% RATAs-Reflection, Absorption, Transmission coefficients, and Substrate
% Absorption coeff
% Absorbedj-Absorption contribution of each layer (fraction of I_0)
% InterfaceParameters- reflection, absorption, and transmission coeffs for
% substrate/air and thinfilm/air or sub interfaces
% beta- fraction of light absorbed by substrate on one pass
% StackParameters-
out={x,Q,Esq,RATAs,Absorbedj,InterfaceParameters,beta};
end

function out=solveTMM(lambda,d,n,angle_in,polarization,steps)
m=length(d)-2; %number of thin film layers (2 less than listed in layers)
phiJ=acosd(sqrt(1-(real(n(1))./n(:)).^2*sind(angle_in)^2));
q=n.*cosd(phiJ);
qj=q(1:end-1);
qk=q(2:end);
nj=n(1:end-1);
```

```
nk=n(2:end);
if polarization=='s'
   rjk=(qj-qk)./(qj+qk);
   tjk=2*qj./(qj+qk);
elseif polarization=='p'
   rjk=(nj.^2.*qk-nk.^2.*qj)./(nk.^2.*qj+nj.^2.*qk);
   tjk=2*nj.*nk.*qj./((nk.^2.*qj+nj.^2.*qk));
end

I=zeros(2,2,m+1); %m+1 2x2 interface matrices
for j=1:m+1
    I(:,:,j)=1/tjk(j)*[1 rjk(j); rjk(j) 1];
end

zj=2*pi/lambda*q(2:end-1);
dj=d(2:end-1);
L=zeros(2,2,m); %m 2x2 layer matrices
for j=1:m
   L(:,:,j)=[exp(-1i*zj(j)*dj(j)) 0; 0 exp(1i*zj(j)*dj(j))];
end

Sj_p=zeros(2,2,m);
Sj_p(:,:,1)=I(:,:,1);
for j=2:m
   Sj_p(:,:,j)=Sj_p(:,:,j-1)*L(:,:,j-1)*I(:,:,j);
end

Sj_pp=zeros(2,2,m);
```

```
Sj_pp(:,:,m)=I(:,:,m+1);
for j=2:m
   Sj_pp(:,:,m+1-j)=I(:,:,m+2-j)*L(:,:,m+2-j)*Sj_pp(:,:,m+2-j);
end

rj_p(:,1)=Sj_p(2,1,:)./Sj_p(1,1,:);
tj_p(:,1)=1/Sj_p(1,1,:);
rj_pp(:,1)=Sj_pp(2,1,:)./Sj_pp(1,1,:);
tj_pp(:,1)=1/Sj_pp(1,1,:);

rj_minus(:,1)=-Sj_p(1,2,:)./Sj_p(1,1,:);
tj_plus(:,1)=tj_p./(1-rj_minus.*rj_pp.*exp(1i*2*zj.*dj));

S=I(:,:,1);
for j=1:m
    S=S*L(:,:,j)*I(:,:,j+1);
end
rtf=S(2,1)/S(1,1);
Rtf=abs(rtf).^2; %thin film stack reflectivity (electrodes and organics)
ttf=1/S(1,1);

ncostheta=real(q);
Ttf=real(q(end)/q(1))*abs(ttf)^2;
%Calculate energy dissipation rate per volume and E^2 at each point within films
alphaj=4*pi*imag(n(2:end-1))/lambda;
Tj=real(q(2:end-1)./q(1)).*abs(tj_plus).^2;
rhoj=abs(rj_pp);
delj=angle(rj_pp);
```

```
sumD=cumsum(d);

x=[];

Q=[];

Esq=[];

for j=1:length(n)-2

   begin=(j-1)*steps+1; %Indices for range of E-fields values. 1, 101, 201, etc. if steps=100

   finish=j*steps; %100, 200, 300, etc.

   xj=linspace(0,dj(j),steps); %discretize layer into 100 nodes is steps=100

   x(begin:finish)=xj+sumD(j);

   Esq(begin:finish)=abs(calcE(xj,tj_plus(j),rj_pp(j),dj(j),zj(j))).^2; %squared electric field, arb units

   theta=real(phiJ(j+1));

% theta=acosd(ncostheta(j+1)/real(n(j+1)))

   Q(begin:finish)=calcQ(xj,alphaj(j),Tj(j),rhoj(j),dj(j),real(n(j+1)),lambda,delj(j),theta); % nm-1

end

out={Rtf,Ttf,x,Esq,Q};

end

function E=calcE(x,tj_plus,rj_pp,dj,zj)

   % x may be a vector, others are scalar inputs

   % E is unitless (technically E/E0+ with incident medium reference E field as in Petterson)

   E=tj_plus*(exp(1i*zj*x)+rj_pp*exp(1i*zj*(2*dj-x)));

end

function Q=calcQ(x,alphaj,Tj,rhoj,dj,nj,lambda,delj,theta)

   %Implements equation 24 in Pettersson, but reduced by I0

   %Q therefore has units of nm-1

   %This gives derivative of absorption coefficient with position at a

   %point, based on some incident power density in left most media
```

```
   Q=alphaj*Tj/cosd(theta)*(exp(-alphaj*x)+rhoj^2*exp(-alphaj*(2*dj-x))+2*rhoj*exp(-alphaj*dj)*cos(4*pi*nj/lambda*(dj-x)+delj));

%    Q./alphaj.*Tj./cosd(theta).*exp(-alphaj.*x)%;rhoj^2*exp(-alphaj*(2*dj-x));2*rhoj*exp(-alphaj*dj)*cos(4*pi*nj/lambda*(dj-x)+delj)]/Q(1)

end

function n=getNandK(layers,lambda,libname)

   n=zeros(length(layers),length(lambda)); %rows layers, columns wavelengths

   [data,dataNames]=xlsread(libname);

   fileLambda=data(:,1); %Wavelengths from first column

   for i=1:length(layers)

      nindex=find(strcmp(strcat(layers(i),'_n'),dataNames));

      ndata=data(:,nindex);

      kindex=find(strcmp(strcat(layers(i),'_k'),dataNames));

      kdata=data(:,kindex);

      n_interp=interp1(fileLambda,ndata,lambda);

      k_interp=interp1(fileLambda,kdata,lambda);

      n(i,:)=n_interp'+1i*k_interp';

   end

end
```

D.3 Center finite difference method solver

```
function C=CenterFDsolver(Ld,theta,tau,lambda,d,Q,BCs)
% Solves for exciton density in a layer using a diffusion, generation,
% recombination governing equation and prescribed boundary conditions
%
% Ld-exciton diffusion length (nm)
% theta-exciton generation quantum efficiency
% tau - exciton lifetime (s)
% lambda- wavelength of light (nm)
% d- layer thickness (nm)
% Q- power dissipated at various points (W/m2 nm)
% BCs- pairs of conditions for left and right boundary in ordered pair
% [BCleft, BCright] (can currently handle homog. dirchlet BCs)
%
%  BC CODES:
% 'hd'-homogeneous dirchlet (C=0)
% 'hn'-homogeneous neumann(dC/dx=0)
```

```
%all arbitrary variables below
beta=1/Ld;% beta-1/L inverse diffusion length of excitons (nm-1)
h=6.626e-34; %planck constant (Js)
D=Ld^2/tau; %exciton diffusivity (nm^2/s)
nu=3e17/lambda; %light frequency (Hz), using speed of light in nm/s
Q=Q*1e-18; %Convert to W/nm3
BCleft=BCs(1);
BCright=BCs(2);

n=length(Q);
dx=(d-0)/(n-1);

A=zeros(n);
b=zeros(n,1);

% Deal with left BC
if strcmp('hd',BCleft)
    A(1,1)=1;
    b(1)=0;
elseif strcmp('hn',BCleft)
    A(1,1)=-2/dx^2-beta^2;
    A(1,2)=2/dx^2;
    b(1)=-theta/(D*h*nu)*Q(1);
else
    disp('Error with left boundary condition')
end

% Deal with interior nodes
for i=2:n-1
    A(i,i-1)=1/dx^2;
    A(i,i)=-2/dx^2-beta^2;
    A(i,i+1)=1/dx^2;
    b(i)=-theta/(D*h*nu)*Q(i);
end
% Deal with right BC
if strcmp('hd',BCright)
    A(n,n)=1;
    b(n)=0;
elseif strcmp('hn',BCright)
    A(n,n)=-2/dx^2-beta^2;
    A(n,n-1)=2/dx^2;
    b(n)=-theta/(D*h*nu)*Q(n);
else
    disp('Error with right boundary condition')
end
C=A\b; %calculates exciton density profile (#/nm3)
C=C*1e21; %converts to (#/cm3)
```